INTERNATIONAL ATOMIC ENERGY AGENCY
UNITED NATIONS EDUCATIONAL, SCIENTIFIC AND CULTURAL ORGANIZATION
INTERNATIONAL CENTRE FOR THEORETICAL PHYSICS
I.C.T.P., P.O. BOX 586, 34100 TRIESTE, ITALY. CABLE CENTRATOM TRIESTE

H4.SMR/453-3

TRAINING COLLEGE ON PHYSICS AND CHARACTERIZATION OF LASERS AND OPTICAL FIBRES

(5 February - 2 March 1990)

Oceanic and Terrestrial Lidar Measurements

F. Hoge

NASA Goddard Space Flight Center
Wallops Flight Facility
Wallops Island, Virginia
U.S.A.

CHAPTER

6

OCEANIC AND TERRESTRIAL LIDAR MEASUREMENTS

FRANK E. HOGE

NASA Goddard Space Flight Center
Wallops Flight Facility
Wallops Island, Virginia

The principal emphasis of this chapter will be on oceanic lidar measurements since most of the technical work described to date has been performed over marine targets. Terrestrial applications are, however, also included for the fol-

lowing reasons. First, some of the initial lidar Earth observations were performed as airborne metric profilometry measurements over land and sea ice. Second, recent airborne laser-induced fluorescence (LIF) experiments over living terrestrial plants indicate the strong potential of lidar techniques for the measurement of plant stress, senescence, pigment content ratios, and so on. When coupled with recently demonstrated metric plant height (including crown thickness and profile), this potential is further enhanced. Third, during the normal course of performing oceanic lidar investigations, an instrument can easily be configured for, and applied to, terrestrial targets such as trees, bushes, grasses, and/or foodcrops. Fourth, an oceanic fluorescence lidar contains all of the necessary subsystems needed to perform terrestrial metric and spectral measurements. Accordingly, terrestrial lidar measurements serve to complete the total lidar Earth observation picture.

While an ultimate goal of oceanic lidar instrument scientists is to obtain global measurements while operating from a space-borne platform, present technology will not allow this to occur in the very near term. Airborne lidars, however, can contribute to passive (or nonlidar) satellite ocean color sensor and algorithm development, validation, and calibration. An excellent example of the cooperative nature of passive and active (lidar) ocean color sensors is presented in the curvature algorithm efforts by Campbell and Esaias (1983). They used laser-induced fluorescence data acquired with the NASA Airborne Oceanographic Lidar (AOL) to help establish the physical basis for a spectral curvature algorithm for the quantification of chlorophyll from an airborne passive ocean color sensor. Also, Grew and Mayo (1983) used the same lidar data to show that the algorithm was valid in open ocean areas and that his passive ocean color instrument had continued to remain stable over a long period. These are the first reported uses of lidar and passive data taken simultaneously by separate active and passive sensors on the same airborne platform.

At present most remote sensing and analysis of marine phytoplankton is performed using passive sensors such as multispectral scanners. A noticeable example is the Coastal Zone Color Scanner (CZCS) operating from the NIMBUS-7 satellite. This is in fact the only sensor ever placed in orbit specifically to study living marine resources. However, airborne lidar sensors are presently under development to assist (a) in improved understanding of existing ocean color remote sensing methodology; (b) in the development of new, passive ocean color sensors; (c) in the validation and/or verification of satellite-derived phytoplankton concentration measurements; (d) in the development of new computational algorithms; and (e) in long-range space-borne lidar ocean color sensor development.

In their own right lidar color sensors can, as will be shown, obtain biooptical measurements that cannot be made by satellite and furthermore obtain these measurements with higher spatial and temporal resolution than is possible with satellite sensors. Additionally, lidar fluorosensors can operate in total darkness, allowing studies of diurnal effects. Moreover, the lidar induced emissions are highly specific, unlike the broad, almost featureless solar-induced ocean color spectra. Finally, lidars offer the prospect of performing high speed (5–100-ns) time domain measurements indicative of molecular relaxation or transition rate processes in the target material.

Although the lidar sensor possesses very high potential, existing passive sensors still have the advantages of lower weight, volume, and power together with reduced complexity with its attendant high reliability. Supplying an additional observational degree of freedom, the passive sensor can provide complementary data for validating the lidar measurements. This active and passive sensor complementarity should ultimately be possible on all platforms including spacecraft.

While lidars are at present being used primarily to validate and improve passive sensors, they are also used to assist in the development of state-of-the-art microwave altimeters and scatterometers. The excellent range resolution provided by narrow pulse widths, the lidar can, for example, yield excellent ocean surface elevation and backscatter power measurement for truthing or comparison purposes. Further, the relatively small laser beam divergence (< 1 mrad) and resulting receiver field of view afforded by a lidar allow the assessment of spatial averaging due to the much larger microwave sensor footprint.

Some of the first published accounts of airborne lidar geophysical measurements were given in the late 1960s time frame. Hickman and Hogg (1969) demonstrated that underwater topography measurements could be made by concurrently observing the water surface return and the pulse energy backscatter from the bottom. Still earlier, Ross et al. (1968) began making sea surface elevation measurements with a modulated CW helium–neon lidar system developed and sold by a commercial laser manufacturer. Even in the mid-1960s this latter lidar system was demonstrating the high potential of laser profiling in terrestrial applications (Jensen and Ruddock, 1965). A sustained but generally small level of research in oceanic and terrestrial lidar development and application has continued subsequent to these early experiments. While the total amount of marine and terrestrial lidar geophysical applications reported to date is rather sparse, fluorosensing experiments are even fewer in number. Furthermore, in some of these latter cases the only field work executed has been performed with the NASA AOL. Accordingly, in many areas of this chapter examples of field experiments utilizing the AOL will be presented. Whenever possible, the remote lidar measurement efforts by other research groups will be discussed herein. It is the sincere hope of this author that no important marine and terrestrial lidar research and applications have been overlooked. Any such omissions are purely inadvertent.

6.1 LIDAR INSTRUMENTATION FOR OCEANIC AND TERRESTRIAL APPLICATIONS

An oceanic lidar is herein defined as a laser transceiver operating from a remote platform situated in the atmosphere or in space at some finite distance from the water's surface. Thus, we will not consider lidars operating from submerged towed fish or submarine vessels but will limit our attention to those located on ground (near water's edge), pier, ship, and satellite platforms. Of these, airborne platforms will be emphasized since (1) the most advanced experiments performed to date have been conducted from them and (2) they are the natural forerunner to satellite lidar systems.

The lidar laser transmitter is assumed to be a pulsed type so that adequate excitation energy is available in a pulse width satisfactory for timing synchronism (ocean surface location and ranging). Furthermore, the laser wavelength is assumed to be within the so-called blue-green window of the ocean. Thus, the surface of the sea can be detected using the reflected Fresnel component while the remainder of the pulse probes the ocean volume. The lidar receiver is generally equipped with a telescope having sufficient aperture to provide enough gain for signal-to-noise ratio enhancement. The detector itself is usually a sensitive, wide-bandwidth, gain-multiplying device such as a photomultiplier or avalanche photodiode. Specific lidar instrumentation configurations fulfilling these general criteria will be referenced in later sections.

The atmosphere is primarily considered to be an intervening medium whose absorption and scattering properties interfere with the lidar oceanic and terrestrial measurements. Thus, unlike other lidars discussed in this book, oceanic and terrestrial lidar design and data analysis techniques are usually configured to avoid or reduce atmospheric effects. For airborne platforms the atmospheric effects for the frequently used 150-m altitude offers few problems. Precipitation and fog are the principal problems encountered. For specific lidar atmospheric measurement techniques, the reader is referred to other chapters in this book.

6.1.1 Oceanic and Terrestrial Lidar Measurements Concepts

Figure 6.1 conceptually illustrates the fundamental observational coordinates for a multichannel lidar. The time coordinate is considered to be the one that uniquely distinguishes an active sensor from a passive one. In a truly literal sense it provides the active or lidar sensor with a three-dimensional measurement capability. A passive sensor essentially possesses only two of these observational coordinates: the signal intensity and the emission wavelength. (In Section 6.1.2 the establishment of the temporal and spectral measurement coordinates within a lidar hardware configuration will be discussed in more detail.) The time coordinate in Figure 6.1 shows a transmitted laser pulse that, in most lidars, is used to initiate temporal measurements and electronically arm the lidar receiver subsystem for impending signal reception, detection, and recording. The strength of this pulse is generally recorded to allow the return signals to be corrected for laser transmit power variations. (No atmospheric volume backscatter is depicted in the trailing edge of the exciting laser even though it may actually be present. Anyway, lidar system operating parameters cannot easily be optimized for simultaneous atmospheric and oceanic measurements.)

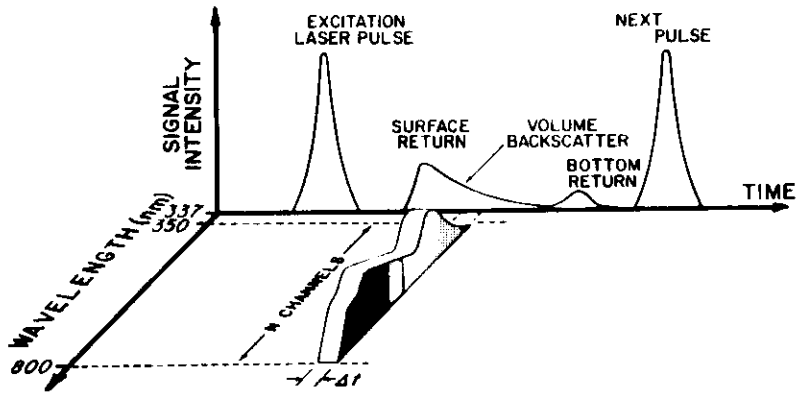

Figure 6.1. Fundamental observational coordinates of multichannel oceanographic lidar. For terrestrial applications the surface return comes from vegetation canopy while volume backscatter and bottom returns are obtained from intervening branches and forest floor, respectively. For both oceanic and terrestrial applications fluorescence spectrum sample gate time Δt can in principle be set to any temporal position from surface to bottom return or sufficiently widened to include entire surface-to-bottom time frame.

For an oceanic lidar the target is the water surface, volume, and, in the case of shallow water, the bottom. At the water's surface the transmitted pulse is partially reflected, but the major portion continues into the water volume to be scattered and absorbed by the water molecules as well as dissolved and entrained materials. The surface return pulse provides several important functions and/or measurements. First, when temporally compared or used with the transmitted pulse, metric measurement capability is realized since multiplication of one-half the elapsed time by the velocity of light yields the slant range to the target. When the vertical component of airborne platform motion is removed (by simple onboard accelerometer, ground-based radar, and/or ranging systems), the slant range measurement can yield sea surface wave, land topogra-

phy, and vegetation canopy profiles. For a conically scanning oceanic lidar, the roll-and-pitch attitude of the remote platform can even be recovered from the slant range data.

Second, the strength of the initial portion of the surface return is indicative of the scattering properties (e.g., capillary waves) of the water surface. The subsequent portion of the return pulse yields volume backscatter data and, in the case of sufficiently clear and shallow water, a bottom return. (For deep-water bodies one may consider the illustrated bottom return as, e.g., backscatter from entrained particulates captured at the thermocline.) In Figure 6.1 a 337-nm (nitrogen) laser with a pulse width of ~8 ns is assumed to provide the exciting laser pulse. This wavelength was assumed for the purposes of this discussion so that the laser-induced spectrum would essentially be shown in its entirety. This wavelength is not the most appropriate one for all applications. In fact, while a bottom return is shown in Figure 6.1 for conceptual purposes, one would not utilize 337 nm for water depth measurements because the attenuation at this wavelength is larger than at blue-green wavelengths.

A third use of the surface return is to initiate the high-speed digitization of the entire surface return, volume backscatter, and bottom return. A high-speed waveform recorder can be activated to accomplish digitization of the backscattered laser signal representing the water's surface and water column to a depth of ~10–30 m. The reader will notice that the backscatter distances or attenuation lengths in the water column are short compared to the kilometer lengths observed in the atmosphere. High-speed electronic timing is therefore crucial. Of course, to accomplish the recording of itself, a facsimile of the surface return must first be sent through a delay line. The surface return is also used to initiate the temporal gating of the spectral fluorescence detection and recording system. In general, all N channels of a fluorosensor can be simultaneously activated so that they can be effectively positioned above, at, or below the water's surface. This is accomplished by varying the time delay portion of the fluorosensor detection system. The integration aperture time Δt (Figure 6.1) may also be adjusted so that the thickness of the horizontal ocean layer can be varied as well. Thus, as seen in Figure 6.1, both the spatial position and width of the water layer being observed can in principle be selected by a combination of delay lines and integration time selection. If the fluorosensor aperture gate is temporally adjusted to correspond to the bottom, the fluorescence from submerged vegetation can conceivably be acquired.

Should one desire temporal (or depth) resolution of the water Raman (or the constituent fluorescence), the on-wavelength waveform digitizer subsystem discussed above can be quickly and easily connected to any chosen spectral channel. Alternatively, the temporal waveform digitization of a chosen wavelength from the laser-induced fluorescence spectrum of, for example, an optically thick

oil film would necessarily be interpreted as fluorescence time decay data, not depth-resolved information.

In terrain and vegetation mapping applications the ranging and temporal waveform-recording capabilities of the lidar can be used to make metric measurements of the surface elevation and tree/bush height. For example, in Figure 6.1, if the water's surface is, instead, a tree top, the lidar system can be used to obtain vertical terrestrial measurements in much the same manner as was done over water bodies. This is particularly true if the tree crown and/or leaf density is sufficiently sparse to allow downward penetration of portions of the laser beam. Of course, if some portion of the beam reaches the ground (as is frequently the case), the bathymetry or depth-resolved portion of the lidar system can be used to record the tree height and scatter from intervening leaves as well. Conceptually, one could at the same time record the fluorescence of a segment of the tree crown and understory at some chosen "depth" from the tree top.

6.1.2 Oceanic and Terrestrial Lidar Instrumentation

Depicted in Figure 6.2 is a generic form of a lidar system that can fulfill many, if not all, the measurement concepts outlined in Figure 6.1 and discussed in Section 6.1.1. The lidar in Figure 6.2 contains all the elements needed to spatially scan the surface, transmit and receive optical radiation, and record the resulting temporal and spectral data pretaining to an oceanic or terrestrial target.

At the heart of this oceanic and terrestrial lidar system is the computer and timing electronics that initiates measurements by commanding the laser to fire and completes the final recording of the data upon receipt of the backscattered radiation. Once the laser is fired, a small portion of the beam is diverted to detector 1 to (a) start the slant range measurement to the target and (b) measure the laser pulse energy. The lidar system is sometimes constructed in such a flexible manner that any one of several types of lasers may be interfaced depending on the experiment being performed. These lasers may have different (1) beam shapes (rectangular and/or oval, e.g., for gas discharge lasers) and (2) beam divergences. Thus, the lidar transmitter is provided with a beam shape and beam divergence control. To facilitate alignment, the transmit beam is made coaxial with the telescope. The scanner subsystem is common to both the transmitter and receiver and may consist of either reflective or refractive optical components depending on weight, volume, and spatial pattern required.

The receiver section is composed of a telescope having sufficient aperture to provide enough gain for signal-to-noise ratio enhancement. A Cassegrain-type telescope is a frequent choice for size, volume, and desirable co-linear axis configurations. The focal plane, adjustable field of view (FOV) allows the re-

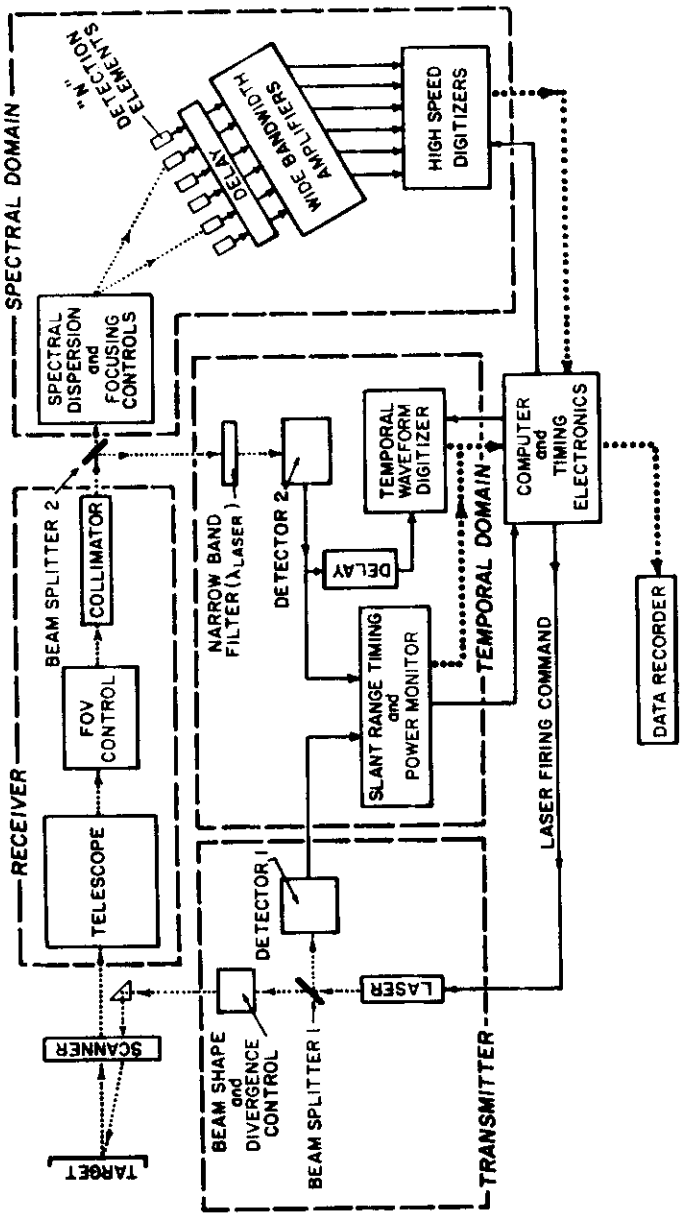

Figure 6.2. Block diagram of generic lidar system capable of making measurements described in Figure 6.1 and discussed in Section 6.1.1. See text for references to specific lidar hardware.

ceiver to view only the laser-irradiated spot on the target surface. Thus, the FOV can be made to closely match the transmit beam divergence. To accommodate symmetrical (e.g., rectangular) beam shapes, the FOV should be adjustable in both the horizontal and vertical dimensions. The receiver FOV control is perhaps one of the most important components of the entire system. It provides background or solar noise rejection by allowing the receiver to view only the spot that is to be illuminated by the laser. The background rejection is sufficient to allow operation of the lidar system during daylight hours. Depending on the application, FOV settings of 2–6 mrad are typically used during daylight hours even when high-gain photomultiplier tube detectors are employed in the system. FOV adjustments to 20 mrad are sometimes used during nighttime experiments. Subsequent to FOV control, collimation allows improved utilization of the received beam for (1) narrow-band interference filtering of extraneous, background noise prior to detection for temporal domain measurements and (2) spectral dispersion for fluorescence applications. Beam splitter 2 is the point at which the temporal and spectral measurement coordinates are established within the lidar hardware. (Refer also to Section 6.1.1 and Figure 6.1.)

The temporal domain measurements naturally divide into two separate segments.

1. The slant range timing, which represents the distance from the aircraft to the target, is obtained by ordinary time-of-flight measurement of the excitation laser pulse and its resulting echo or backscattered surface return (see Figure 6.1 also). For an aircraft platform operating at 150 m altitude the two-way elapsed time is ~ 1 μs. Electronic counters are readily available that allow measurements of range with a precision of ~ 0.02 m.
2. The surface return, volume backscatter, and bottom reflection (if any) are typically obtained with a wide-bandwidth waveform recorder. For oceanic and terrestrial lidar applications these waveform recorders typically span a total extent of only ~ 100–200 ns with contiguous, individual time bins having widths of ~ 5 ns. The time delay shown in Figure 6.2 is used to allow the range timing module to initiate the waveform recording at the proper moment.

The spectral measurement portion of the lidar system receives collimated background, on-wavelength, as well as laser-induced water Raman and fluorescence backscatter signals. This multicolor radiation is dispersed by diffraction grating (or by prism) and focused on N detectors. The number of detectors is primarily dictated by the resolution and the sensitivity required by the experiments. As before, a time delay is used in series with the detectors to allow the

high-speed digitizers to be activated in synchronism with the received fluorescence pulses. The N detection elements can be individual high-gain photomultiplier tubes, a silicon diode array, or an image dissector. These detectors may also be used in conjunction with image intensifiers for added sensitivity. The final choice depends on the sensitivity, spectral resolution, and spectral time decay measurement requirements. Lidar systems having many of the characteristics and features generally described here have been reported in detail in the literature (Bristow, 1978; Bristow et al., 1981; Hoge et al., 1980; Hoge and Swift, 1981b; O'Neil et al., 1980; Capelle et al., 1983; Franks et al., 1983). The status of airborne laser fluorosensing was recently discussed by O'Neil et al. (1981).

6.2 LIDAR MEASUREMENTS OF OCEAN SURFACE, VOLUME, AND BOTTOM

The airborne pulsed neon laser experiments by Hickman and Hogg (1969) amply demonstrated that the ocean surface, intervening volume, and the bottom could be probed remotely with airborne laser systems. Accordingly, the physical, chemical, and biological states of the surface, volume, and bottom regions were thus irreversibly declared fair game for the scientist interested in obtaining such knowledge in ways that only lidar remote sensing could uniquely provide.

While the ocean volume contains by far the majority of the important chemical and biological constituents, we will nevertheless begin the discussion of oceanic applications with the ocean surface. This is done for several reasons. First, historically some of the initial airborne lidar experiments were conducted to measure the sea surface wave profile or determine the on-wavelength backscattering cross section. Second, the airborne lidar measurement of fluorescence was first conducted on oil slicks residing on the sea surface. Third, the concept of using the volumetrically derived seawater Raman backscatter as the reference signal for lidar measurements can be introduced early in a formal, closed-form theoretical, and quantitative way for demonstrating airborne lidar metric measurements of oil films on the sea surface. In turn, this will (a) demonstrate the need for (and the importance of) the water Raman signal in most, if not all, oceanic lidar measurements; (b) lead naturally to its later use as a reference signal for measurement and/or correction of water column attenuation during the volumetric measurement of ocean constituents; and (c) encourage the reader to suggest and/or develop oceanic lidar measurement applications (and their attendant theories) based on this inherent oceanic lidar return signal. Thus, at the risk of excessive detail, the theory of oil fluorescence measurements will be fully discussed in Sections 6.2.1.4 and 6.2.1.5 in order to directly illustrate the quantitative potential that lidar measurements possess.

6.2.1 Measurements of Natural and Contaminated Ocean Surfaces

6.2.1.1 Lidar Backscatter

Outside of the initial bathymetric measurements discussed above, some of the first published accounts of lidar measurement of the uncontaminated ocean surface dealt with backscatter cross-sectional or signal return experiments. Indeed, it became necessary to first understand how the narrow coherent transmitted laser beam interacted with the ocean surface, and furthermore how the resulting small FOV telescopic receivers intercept and process such optical returns. One of the first published reports of airborne laser backscatter measurements from the sea surface was given by Jelalian (1968). While he (as well as Hickman and Hogg) made quantitative measurements, probably the most important finding of these original lidar investigators was that narrow-beam optical radar techniques from airborne platforms were feasible and presented no overriding physical complexity. Jelalian (1968) used a nadir-pointed 1.06-μm pulsed Nd-YAG laser at various aircraft altitudes to show that the surface return is range-square dependent and that the target cross section per unit area was larger for calm water than for seas with a measurable sea state. Petri (1977) made more extensive off-nadir measurements from a platform suspended from the southernmost Chesapeake Bay bridge span. He was also able to show that the return signal backscattered at normal incidence is larger for low sea states (corresponding to low wind speeds) and smaller for higher sea states. This is illustrated in Figure 6.3. Likewise, his data vividly showed that lidar systems that must operate off nadir should do so only if sufficient winds exist to disturb the sea surface and thereby produce sufficient surface facets to yield an adequate return signal to effect or at least initiate a lidar measurement. Anyone who attempts to operate a lidar system over calm water will readily observe that strong mirrorlike specular reflections occur near nadir and that significantly lower signals are received at 5°–10° from the nadir. Theoretical calculations by Swennen (1968) had predicted the decrease in signal with increasing wind speed for a normally incident beam. One can infer from his calculations that the wind-disturbed surface deflects the energy into the off-nadir wings (see Petri's data, Figure 6.3). Phillips (1979) formulated the general backscatter problem in terms of the wavenumber spectrum of the sea surface and showed that the amplitude (as well as the temporal) fluctuations depend on the wavenumber spectrum within the laser footprint. Unfortunately, his wavenumber development lacked sufficient data for the parameters to further verify the full applicability of the technique. While numerous airborne lidar experiments have been performed to date, a paucity of data has been published except as cited above. Bufton et al. (1983) has recently provided airborne scanning laser data at wavelengths of 337 nm, 532 nm, and 9.5 μm. He showed that the mean backscatter had a Gaussian-like shape with

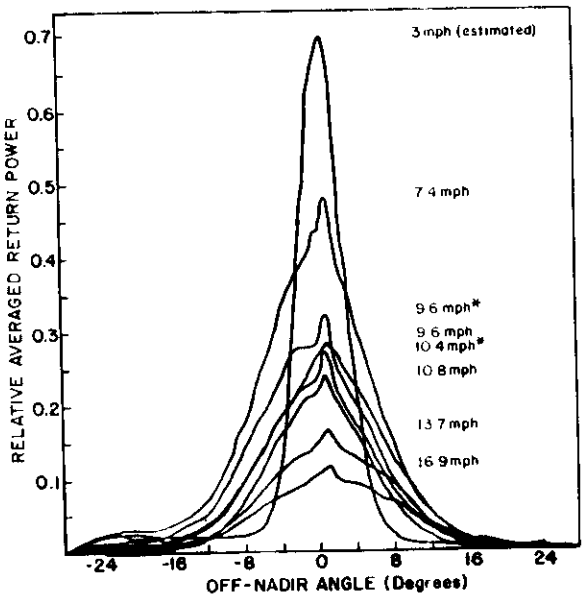

Figure 6.3. Average return signal as function of off-nadir lidar observational angle. Each transmit-power-normalized curve represents average of 18 azimuth positions (except single azimuth position averages labeled by asterisk). Data collected at 16 scans per second with receiver field of view of 24 mrad (Petri, 1977).

a FWHM ranging from 11° to 24° for wind speeds of 1.8–6.5 m/s. At or near nadir the normalized standard deviation ranged from 0.1 to 0.6. Furthermore, by airborne calibration against beach sand, an effective Lambertian reflectance of about 20% was found. This is of course about an order of magnitude higher than the theoretical Fresnel reflectance of an air–sea interface.

From a practical standpoint the laser backscatter measurements and theoretical developments performed to date allow one to only approximately ascertain the field conditions and lidar operating parameters under which satisfactory data can be obtained. As a specific example, consider the backscatter data adopted from Petri (1977) and given in Figure 6.3. From this data it is rather clear that a lidar with a scan angle of ±20° off nadir would have adequate surface return to initiate a measurement only within ±6° of nadir on days when the wind speed was ~3 mph. The data also indicate that operation beyond ±25°, even on the windiest days, would in all probability be marginal. Increasing the laser footprint size will probably increase the return signal. Likewise, opening the receiver FOV will no doubt improve the detection of the surface return pulse

but will in turn lead to a compromise in SNR during daylight hours. As may be seen later, it is possible to have sufficient wind to produce a ruffled sea surface for adequate backscattered surface return and still have detection problems. These detection difficulties can be caused by the wave-damping effects of, for example, a target oil slick or monomolecular film or strong near surface wave-current interaction and/or strong air–sea surface temperature gradient (McClain et al., 1982b). These wave-damping mechanisms modify both the height and slope probability density of the surface waves within the footprint so that the surface return is reduced.

It should be noted in passing that a conically scanning lidar system (Hoge et al., 1980) can be used to ascertain the airborne platform attitude should such orientational information be required. Byrnes and Fagin (1978) applied optimal filtering analyses to scanning data from the NASA AOL. They showed that the roll and pitch of the aircraft can be obtained with an accuracy comparable to that obtained from the gyros of an onboard inertial navigation system. The effects of large scan angles, sea state and currents, laser pulse width and repetition rate, and so on, were not studied to indicate the range of practicality.

6.2.1.2 Airborne Laser Profilometry

Laser profilometry (Ross et al., 1968) of ocean surface waves was apparently the first application of a lidar to oceanic surface wave studies. The potential of high spatial (and metric elevational) resolution of laser profilometry was quickly recognized, and a short time later (Ross et al., 1970) it was applied to the scientific study of sea surface wave development under fetch-limited wind conditions. In fact, these studies also served to show the rapid acceptability of laser instrumentation by the scientific community since these airborne experiments were made in conjunction with microwave profilometry measurements. In spite of its continuing simplicity of airborne instrument application, laser sea surface wave profilometry data interpretation advances have probably been the important ingredient to its recent increased acceptability. Long (1979) and Kats and Spevak (1980) detailed the procedures for analyzing surface gravity wave spectra observed in a moving reference frame. Additonally, due to (1) the recognition that the frequency spectrum of a homogeneous wave field can be distorted by flight direction relative to the wave field (McClain et al., 1980) and (2) the utilization of recently developed analytical and theoretical techniques (McClain et al., 1982b), laser profilometry has been shown to be useful in the measurement of sea state variations across oceanic fronts. In fact, a profilometer can be used to determine the directional properties of a wave field with an accuracy of better than ±10%, and the wavelength of each dominant component can also be determined to within 10%. For the verification of wave–wave and wave–current interactions, airborne laser profilometry may well be the only way to

obtain the high-resolution, synoptic data required. Recently, laser profilometry has been used to simultaneously measure ocean wave elevation and return power to identify those portions of the ocean wave yielding the highest backscatter cross section (Hoge et al., 1984). Laser profilometry has similarly been used to assist in the study of the electromagnetic bias of microwave altimeter systems when applied to satellite ocean topography measurements (Walsh et al., 1984; Choy et al., 1984).

6.2.1.3 Oceanic Geoid Measurements by Laser Altimetry

Lidar altimeters operating from space platforms promise improved elevation measurement precision since laser pulse widths in the 70-fs domain have recently been demonstrated (Fork et al., 1982). No doubt, even shorter pulse width lasers will become available in this decade. The space-borne altimetric measurement of the oceanic geoid by lidar has of course not yet been attempted. The theoretical background for such measurements have been given by Gardner (1982) and by Tsai and Gardner (1982). Their developments have beginnings in satellite microwave radar altimetry, which has proven highly successful during the past decade (McGoogan and Walsh, 1979). High-precision laser altimetry would allow higher spatial resolution mapping of the geoid and potentially the inference of ocean surface currents through high-resolution ocean surface elevational measurement of geostrophic effects. These ocean currents are in part responsible for the transport of biological and chemical constituents in the ocean. The ocean current transport is rather easily seen in satellite ocean color and temperature images of the ocean surface (Gordon et al., 1983). There are several reasons for discussing laser altimetry of the ocean surface within the confines of a book that focuses on laser remote chemical analysis. As we shall see in Section 6.2.1.5, the transmitted and backscattered pulse time-of-flight measurement by such lidar systems yields sea surface elevation measurements but simultaneously can give surface roughness information via pulse energy amplitude (Hoge et al., 1984). The surface roughness in turn determines the coupling of wind energy into the upper surface layers of the ocean. In turn, these wind-generated waves and currents are in part responsible for the transport of the chemical and biological constituents within the water column. Given sufficient laser power and receiver aperture, the same lidar altimeter performing altimetry and/or surface wave elevational measurements could be used simultaneously to measure the laser-induced fluorescence of phytoplankton photopigments (chlorophyll *a* and phycoerythrin), dissolved organic material (DOM), surface slicks, and so on. Present-day airborne lidar fluorosensors are capable of simultaneous measurements of the sea surface elevation and spectral fluorescence (Hoge and Swift, 1983a), but it will probably be several decades before such multiuse space-borne lidars are operational. One would expect to first see

existing passive ocean color scanners mated with microwave altimeters, wherein the altimeter is used to determine sea state and ocean currents for respective correction of ocean color images for glint and the determination (and ultimate understanding of) possible transport current mechanisms. Gradually, then, the microwave altimeter could be supplanted with the laser altimeter. Ultimately, given sufficient and expected technological progress, the laser altimeter could advance to simultaneous measurements of laser-induced fluorescence as well as geoid and surface wave determinations. Coupled with space-borne passive ocean color scanners similar to those in existence today, such lidar systems could yield data of significant use to the oceanographic community. The future challenge is to concurrently obtain sufficient laser energy and receiver aperture size to make oceanic and terrestrial application of such space-borne lidar color (fluorescence) sensors practical.

In the meantime, the study of the electromagnetic bias problem, which limits the ultimate accuracy of space-borne altimeters, must also be continued (Walsh et al., 1984; Hoge et al., 1984; Choy et al., 1984). Furthermore, the detailed satellite laser altimetry studies of Tsai and Gardner (1982) and the joint height-slope probability density function developments of Huang et al. (1983, 1984) should be combined with the space-borne laser studies to perhaps provide additional insight into the problems of space-borne laser altimetry.

6.2.1.4 Sea Surface Oil Slick Detection, Measurement, and Identification

Petroleum hydrocarbon inputs to the world's oceans are estimated to be about six million metric tons each year (Myers and Gunnerson, 1976). International interest in the study of spilled oil continues, as evidenced by the technical papers originating during the past decade from the United States (Kung and Itzkan, 1976; Hoge and Swift, 1980; Hoge and Swift, 1983a; Hoge, 1983), Canada (O'Neil et al., 1980; Rayner et al., 1978; Rayner and Szabo, 1978), The Netherlands (Visser, 1979), Italy (Burlamacchi et al., 1983), Japan (Sato et al., 1978), and the USSR (Abramov et al., 1977; Bogorodskiy et al., 1977).

Unlawful spillage cannot easily be deterred unless the oil can be classified according to some criteria. While numerous passive sensors can detect the oil slick and thus measure its areal extent, none has the capability to classify the oil. However, Fantasia et al. (1971) and also Measures and Bristow (1971) separately concluded that the laser-induced fluorescence spectrum (including fluorescence lifetime) showed significant promise. A helicopter-borne fluorosensor later demonstrated for the first time that the fluorescence spectrum could be detected (Fantasia and Ingrao, 1974) remotely. It has been shown that the shape of the fluorescence color spectrum alone is adequate to separate the oil into three classifications: (1) light-refined products such as diesel fuel, (2) crude oils, and (3) heavy oils such as Bunker C fuel oil (O'Neil et al., 1980). Given

the large number of oils that produce different spectra (Fantasia and Ingrao, 1974), a classification into only three types would not be sufficient to allow deterrent policing for surreptitious spillage. However, Measures et al. (1974) have demonstrated that fluorescence decay time spectroscopy could be used to discriminate between similar hydrocarbons. Furthermore, since the fluorescence conversion efficiency is highly variable among the oils (Fantasia and Ingrao, 1974), the avenue of development seems clear: a classification scheme based on oil fluorescence decay time spectroscopy and conversion efficiency should be undertaken.

However, a thin portion of an oil slick will produce less fluorescence than a thick portion so that a different conversion efficiency would apparently be found throughout a slick, thus rendering the fluorescence conversion efficiency method questionable if not useless. What was needed, then, was a method of remotely sensing the fluorescence conversion efficiency of oil slicks independent of their thickness. The theory for such a remote oil fluorescence classification technique was published by Kung and Itzkan (1976), and airborne validation experiments were begun in 1978 (Hoge and Swift, 1980, 1983a; Hoge, 1982). The Kung and Itzkan method of calculating the characteristic infinite-thickness absolute spectral fluorescence conversion efficiency from oil films of finite thicknesses used the seawater Raman backscatter as the reference signal for calibration. The theory also accounted for the background fluorescence caused by dissolved organic material, or *Gelbstoff*. They showed that under most conditions the absolute oil fluorescence spectral conversion efficiency (AOFSCE) could be determined within a factor of 2 accuracy if the oil film is $\geqslant 0.5$ μm thick, the oil fluorescence is greater than the *Gelbstoff* fluorescence, and the water column beam attenuation at the laser wavelength and at the Raman backscatter wavelength is less than 1.2 m^{-1} somewhere along the flight path. (This latter requirement is to allow at least one measurement of the depth-resolved water Raman decay constant in reasonably clear water. Assuming long-term drift is not a problem, the integrated Raman and its corresponding depth-resolved decay constant are both constant multiples of each other at all other positions of the flight where a Raman signal can be obtained.) These criteria being satisfied, the theory allows a general classification of oils without a priori knowledge of the oil film thickness. Furthermore, once the oil is positively identified, we shall see later that the oil film thickness can in turn be measured. Of course, this latter measurement aids in the determination of the volume of oil spilled.

The AOFSCE theory has been field tested using the NASA AOL (Hoge and Swift, 1980, 1983a). The absolute oil fluorescence spectral conversion efficiency η_f is given by (Kung and Itzkan, 1976)

$$\eta_f = \frac{\sigma N_w T_e T_r}{\gamma_e + \gamma_r} \frac{\theta_f}{1 - \Delta_r^{1+\epsilon}} \left(1 - \frac{\Delta_r^{1+\epsilon}}{\Xi_f}\right) \tag{6.1}$$

where σ = Raman cross section of water

N_w = number density of water

T_e, T_r = transmissivities of air–sea interface at laser emission and Raman wavelengths, respectively

γ_e, γ_r = effective or beam attenuation coefficient of seawater at laser emission and Raman wavelengths, respectively

θ_f = oil fluorescence signal at wavelength λ_f as normalized by water Raman signal measured outside slick, K_f/R (see Figure 6.4*a*,*b*)

Δ_r = Raman signal amplitude measured while over oil slick (with fluorescence contributions from oil and *Gelbstoff* at λ_r removed by interpolation and subtraction) normalized by water Raman from clean sea region, R'/R (Figure 6.4*a*)

Ξ_f = oil fluorescence measured over oil slick and normalized by fluorescence signal at λ_f observed outside slick, K_f/J_f

Finally,

$$\epsilon = \frac{\kappa_f - \kappa_r}{\kappa_e + \kappa_r} \tag{6.2}$$

where κ_f, κ_r, and κ_e are the extinction coefficients of the oil at wavelengths λ_f, λ_r, and λ_e, respectively. Figure 6.4*a* contains the essential definitions of many of the above parameters defined for LIF of oil and water column constituents.

The first multiplicative term of Equation (6.1) is known as the seawater Raman conversion efficiency:

$$\psi = \frac{\sigma N_w T_e T_r}{\gamma_e + \gamma_r}. \tag{6.3}$$

Thus, a straightforward or simplified interpretation of Equation (6.1) is that the absolute oil fluorescence spectral conversion efficiency is the water column Raman conversion efficiency modified by two additional multiplicative terms whose values depend on the extinction and spectral fluorescence properties of the oil. Ideally, the oil fluorosensing lidar can be equipped to remotely measure the sum of the effective attenuation coefficients of water, $\gamma_e + \gamma_r$, by utilizing the temporal variation or depth-resolved Raman signal backscattered from the water column. Then

$$\gamma_e + \gamma_r = \frac{c\tau}{2n} \tag{6.4}$$

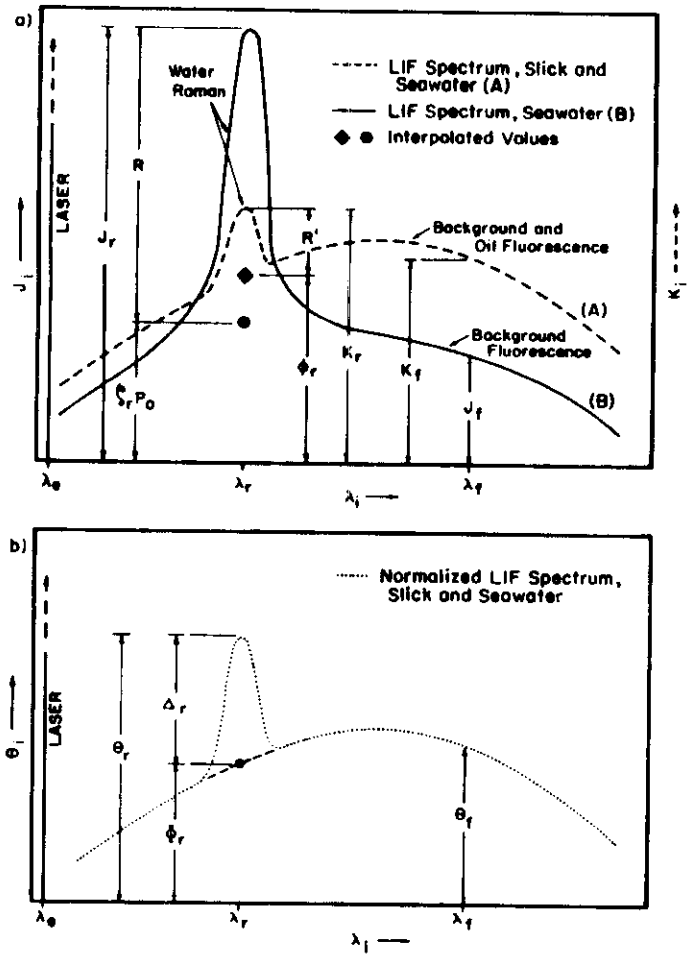

Figure 6.4. (*a*) Theoretical or expected laser-induced fluorescence spectral waveforms over (A) ocean water covered by optically thin oil film and (B) ocean water. (*b*) Spectral waveform of ocean water normalized by water Raman backscatter R (Hoge and Swift, 1980).

where c is the velocity of light, n is the index of refraction, and τ is the Raman signal decay time constant computed from total elasped, or two-way, time decay data. During our oil spill experiments, the NASA AOL could not be rapidly reconfigured from the spectral mode to the temporal or depth-resolved mode in order to measure τ. Instead, an estimate of ψ from the water optical transmission

data taken by truth ships in the immediate vicinity of the spill was used. It is recognized that the ultimate utility of AOFSCE for the general typing of oil spills with an airborne laser fluorosensing system requires a measurement of ψ independent of any supporting surface vessels and during the same time frame as the airborne oil fluorescence data is acquired. Therefore, the latter sections of this chapter will describe progress to date in the measurement of depth-resolved water Raman during separate field experiments. The reader will no doubt recognize the general oceanographic usefulness of the remote measurement of ψ and its interpretation via Equation (6.3) of the effective extinction coefficient of the water column.

Field experiments to investigate the Kung–Itzkan theory have been performed with the NASA AOL. The AOL instrument was configured with a 337-nm nitrogen laser transmitter having an energy of 1 mJ in a 10-ns pulse. The fluorosensing mode was used for the airborne spectral measurements described herein. The range of AOL transmitter and receiver parameters used in the oil spectral measurements are essentially described in some of the previous publications referenced above. For convenience, the important parameters are summarized in the fluorosensor portion of Table 6.1.

During November 1978 the AOL participated (together with the Canada

Table 6.1. AOL Operating Parameters

	Oil Fluorosensing Mode, Nitrogen Laser
Transmitter	
Wavelength	337.1 nm
Bandwidth	0.1 nm
Pulse width	10 ns
Pulse rate	$\leq$ 100 Hz
Peak output power (max)	100 kW
Beam divergence	4 mrad
Receiver	
Bandwidth	3500–8000 Å
Spectral resolution (min)	11.25 nm
Field of view	1–20 mrad, variable, vertical, and horizontal
Temporal resolution	8–150 ns, variable
Experiment	
Aircraft altitude	150 m
Aircraft velocity	75 m/s
Measurement background	Day

Center for Remote Sensing; O'Neil et al., 1980) in a series of missions designed to measure the effects of a dispersant on the spreading rates of crude oils spilled on the ocean surface. Information regarding the spills is provided in Table 6.2. Additional physical characteristics of the two crude oils are given in Table 6.3. The data analyzed were from missions flown over the LaRosa slick on November 3, 1978, and the Murban slick on November 9, 1978.

Figure 6.5 shows the calculated AOFSCE at 500 nm for the Murban crude oil as a function of oil film thickness. The thickness could be obtained since (a) the oil type was known a priori and (2) the extinction coefficients had been measured in the laboratory (Hoge and Kincaid, 1980; Hoge, 1982). Although the theoretical model should recover the same conversion efficiency for all thicknesses, the fluorescence yield is apparently too low for films $< 2\ \mu m$ thick. This is especially evident for the more fluorescent Murban crude. A minimum limit for the AOFSCE application was not totally unexpected since the calculations of Kung and Itzkan (1976) showed that the film should be $> 0.5\ \mu m$ to attain a conversion efficiency within a factor of 2 accuracy using a lidar having instrument parameters similar to the AOL.

A single self-contained lidar for AOFSCE measurements must be capable of depth-resolved water Raman backscatter measurement at some position along the flight line in order to complete the calibration. Few fluorosensors are yet configured to perform this portion of the AOFSCE measurement during the same mission. However, such instrument configuration problems are tenable (and have actually been accomplished on the AOL). This was not the case during the oil spills discussed herein, so experiments to ascertain the feasibility of performing the requisite AOFSCE depth-resolved seawater Raman backscatter was performed separately (Hoge and Swift, 1983a,b). A mission was flown off the coast of Virginia in the Atlantic Ocean. It consisted of a single flight line originating about 30 km offshore and intersecting the beach. This gave a continually varying water column attenuation. As with the oil spill experiments, a 337-nm pulsed laser was used. With the AOL configured into the

Table 6.2. Experiment and Data Summary

Date	Crude Oil Type	Dispersant Applied	AOL Data Passes Before Dispersant		Total AOL Data Passes
			Nonscan	Scanning	
November 2, 1978	Murban	After 2 h	0	0	18
November 3, 1978	LaRosa	After 2 h	3	5	33
November 9, 1978	LaRosa	Immediately	0	0	37
	Murban	Immediately	0	1	17

Table 6.3. Spilled Oil Types and Selected Physical Characteristics

Oil	Source	Type Crude	Fluorescence		Extinction Coefficient (nm^{-1})			
			Emission	Peak Wavelength (nm)	337.1 nm	381 nm	500 nm	API°
LaRosa	Venezuela	Heavy	Low	490	896	434	189	23.3
Murban	Middle East	Light	High	505	265	95	26	38.1

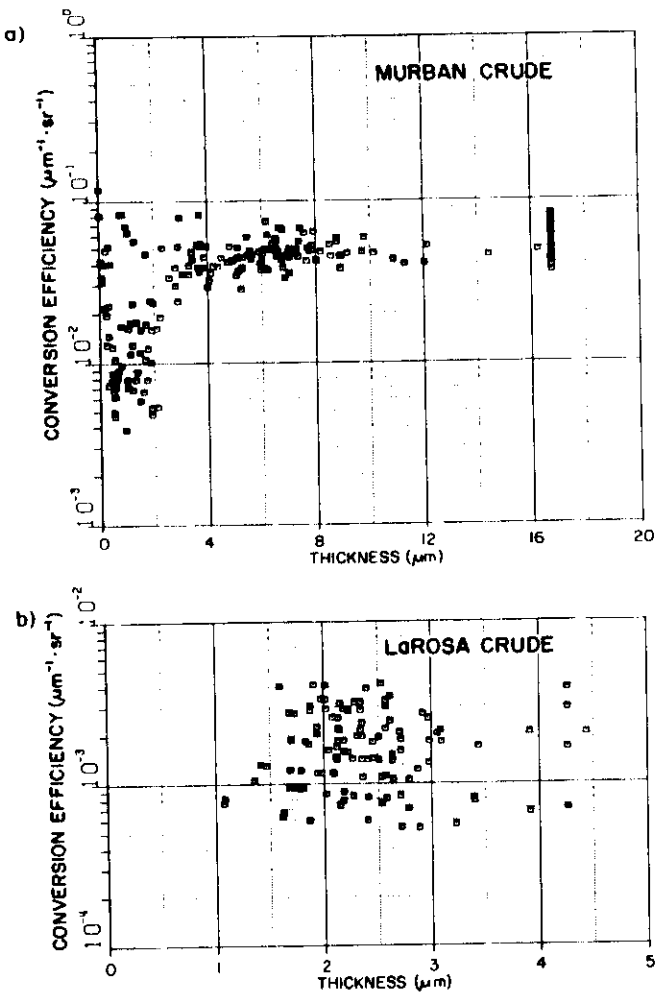

Figure 6.5. (*a*) Oil fluorescence conversion efficiency of Murban crude oil as function of film thickness. (*b*) Oil fluorescence conversion efficiency of LaRosa crude oil as function of film thickness (Hoge and Swift, 1980).

bathymetric mode (Hoge et al., 1980), the depth-resolved waveforms in Figure 6.6 were obtained.

Figures 6.6*a*–*c* show typical depth-resolved waveforms of the laser-induced water Raman backscatter. Note that the offshore waveforms (Figure 6.6*a*) have a larger amplitude and extend to greater depths. As one proceeds shoreward

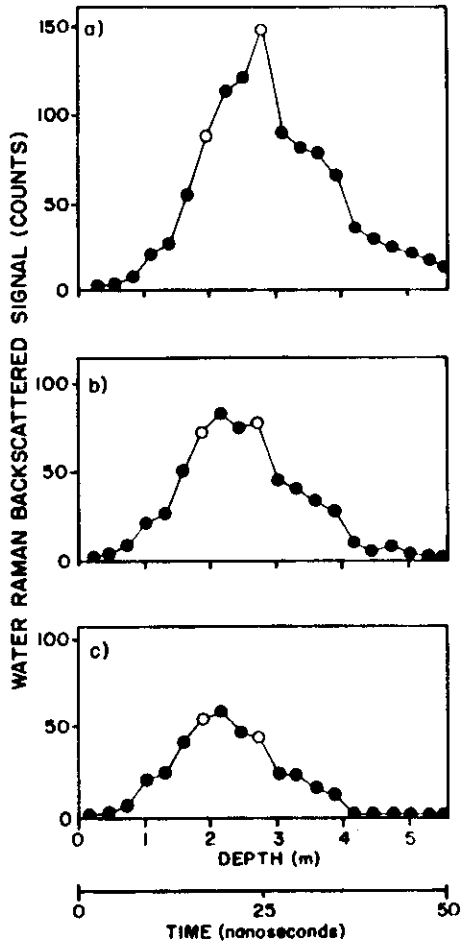

Figure 6.6. Depth-resolved, 337.1-nm laser-induced water Raman backscatter waveforms. Open circles at channels 7 and 10 are labels for subsequent discussion of turbidity cell structures in Section 6.2.2.4 (Hoge and Swift, 1983c).

(Figures 6.6*b*,*c*) into more turbid water, the backscatter from the deeper regions of the water column is progressively lost, as would be expected. At the same time, the peak amplitude of the backscattered Raman signal also declines. As a consequence, the instantaneous peak amplitude of the Raman waveform progressively shifts toward shallower depths as increasingly more turbid water is encountered. Later in this chapter we shall discuss from theoretical considerations the general shape of the backscattered Raman pulse and its relationship to the system response, sea surface, and water volume attenuation characteristics. The channel-to-channel sensitivity variations within each waveform were not correctable because of an inadvertent and unfortunate loss of calibration data in the time frame the experiment was conducted. The relative and qualitative features of the data together with the resulting conclusions are, however, unaffected. Recently developed calibration techniques together with new waveform digitizing equipment now permit significantly better quality data from the AOL.

A straightforward convolutional model accounts quite well for the observed pulse shape is increasingly turbid water. It can be shown (Hoge and Swift, 1983c) that the Raman pulse shape can be represented rather well by the multiple convolution of a Gaussian lidar system response, Gaussian sea surface height and slope probability density, and an exponential water column response,

$$R(t) = A \exp\left(\frac{-t}{\tau}\right) \exp\frac{\sigma^2}{2\tau^2}\left[1 + \operatorname{erf}\left(\frac{t}{\sigma} - \frac{\sigma}{\tau}\right)\right] \tag{6.5}$$

where

$$\sigma^2 = \sigma_g^2 + \sigma_t^2 \tag{6.6}$$

and σ_g denotes the rms width of the lidar system and σ_t is related to the width of the sea surface density $\sigma_\zeta = c\sigma_t/2$, where c is the velocity of light. From Equation (6.4) the parameter τ is related to γ_e and γ_r, the effective attenuation coefficients of the seawater at the laser and Raman wavelengths, by

$$\tau = n/2c(\gamma_e + \gamma_r) \tag{6.7}$$

where n is the index of refraction of seawater, and the factor of 2 accounts for the fact that the digitized waveform is recorded for the entire two-way propagation path. The constant A is

$$A = 1/c\pi S^2 \tag{6.8}$$

where S^2 is the mean square value of the total slope. For this simple convolution model, it is seen that the amplitude of the backscattered pulse is principally

influenced by the mean square value of the total slope S^2. The remaining shape is, of course, contributed by the incident pulse width, sea state in the footprint, and the water attenuation function. For rapid computational purposes (1) a series expansion or (2) a rational approximation of the error function for argument z, erf(z), may be used (Abramowitz and Stegun, 1964; Hayne, 1980).

For initial estimates assume $\gamma_e = 2\gamma_r$ (Hoge and Swift, 1981a). To estimate the rms width of the laser system response, we note that our 337.1-nm nitrogen laser has an inherent pulse width of ~8 ns. We have measured a FWHM pulse width η of ~12 ns with the entire system including the waveform digitizer. But the FWHM pulse width is related to the rms width by $\eta = 2\sigma_g\sqrt{2 \ln 2}$. Thus, $\sigma_g = 5$ ns.

The mean square total slope S^2 may be obtained from the Cox and Munk (1954) relation

$$S^2 = 0.003 + 0.005W \tag{6.9}$$

For a wind speed W of 5 m s^{-1}, the rms wave height σ_ζ would for this wind speed be on the order of 0.7 m (Hoge et al., 1984). Then, $\sigma_t^2 = 4\sigma_\zeta^2 c^2$ yields a value of ~5 ns. However, the AOL radiated (and viewed) spot on the ocean surface is ~0.6-m diameter from our operating altitude of 150 m. Therefore, the instantaneous rms wave height within this spot for any single pulse is probably no greater than ~3 cm. This would yield a negligible contribution of the Raman pulse shape compared to an incident pulse width of ~8 ns.

Using the values of the above parameters, the Raman pulse given by Equation (6.5) is plotted in Figure 6.7 together with the Gaussian lidar system response and water column exponential decay function. Note that (1) the incremental entry of the laser pulse into the water and (2) the attenuation within the water column causes the Raman pulse to have a longer leading edge risetime. This results in a maximum or peak amplitude that is shifted several nanoseconds late with respect to the lidar (flat-surface) system response.

Furthermore, the tail of the Raman pulse is, of course, lengthened by the depth or range extent reached by the exciting laser pulse. Accordingly, as the water column attenuation increases, one would expect this trailing portion of the pulse to be quite sensitive to this attenuation because of the exponential behavior of the effect. This is indeed what happens in this computational model as well as the experimental field data (cf. Figure 6.6). In Figure 6.7 the uppermost water attenuation curve and resulting Raman pulse correspond to the most transmissive water we have observed in the coastal region near Wallops Island (Hoge et al., 1980). In this case we assumed $\gamma_e = 2\gamma_r = 0.1$ m^{-1}. The other two lowermost curves in Figure 6.7 correspond to succeedingly less transmissive water, having $\gamma_e = 0.6$ and 1.0, respectively. Note that progressively more water column attenuation yields a lower peak amplitude and a shift of this peak

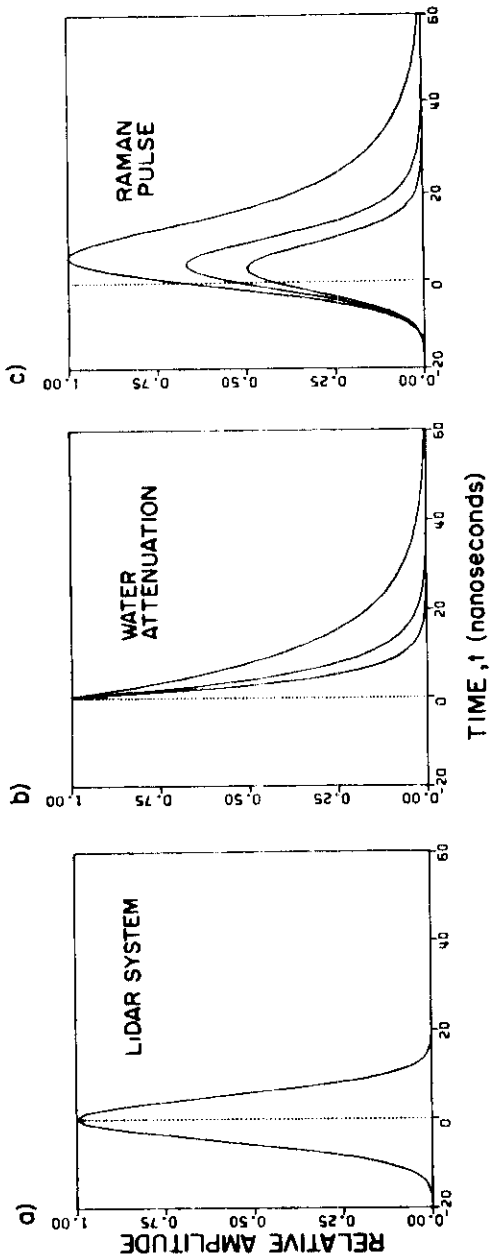

Figure 6.7. (*a*) Assumed Gaussian lidar system response function and (*b*) exponential water attenuation function. (*c*) Backscattered Raman pulse $R(t)$ calculated from convolution of Gaussian lidar system response, Gaussian sea surface height and slope probability density, and exponential water column response (Hoge and Swift, 1983c).

to shorter time and thus shallower water depths. This shift of the peak of the Raman pulse (as well as other attendant changes in pulse shape) would continue only until the Raman pulse becomes essentially equivalent to the lidar system response. At this point, of course, the amplitude of the Raman pulse (but not the on-wavelength Fresnel backscatter) tends to zero since no water molecules can be accessed due to the higher turbidity. One can easily see that the quantitative measurement of the effective attenuation coefficient is ultimately limited by the lidar system response. In our lidar system the principal contribution to the response is the transmitted pulse width. Therefore, if one wishes to conduct measurements in highly turbid water bodies, much shorter laser pulselengths than used in our initial equipment will be required. However, as Kung and Itzkan (1976) point out, the water column decay τ need only be measured at one position along the flight line where the water is sufficiently clear to yield a measurement for AOFSCE purposes. Then, if the system does not drift during the completion of the line, the τ at a more turbid region of the test site can be obtained by simple ratio with the total integrated Raman signal. Thus, it appears that oil spills can be classified according to their spectral conversion efficiency by using the water Raman signal for absolute calibration.

As was noted earlier, Equation (6.7) is obtained from Equation (6.4). The γ's are generally called the *effective attenuation coefficients* since it is not always known whether (a) the beam attenuation coefficient (frequently denoted by α or c, the latter not to be confused with the velocity of light) or (b) the diffuse attenuation coefficient is required. Confusion prevailed for several years until Gordon (1982) gave an interpretation for lidar elastic or on-wavelength backscattered signals. He used Monte Carlo techniques to solve the radiative transfer equation and found that the backscattered power is a decaying exponential function of time over the time interval required for the photons to travel four attenuation lengths through the water. Perhaps more importantly, it was also found that the effective attenuation coefficient of this exponential decay is strongly dependent on the parameters of the lidar system as well as on the optical properties of the water. The ratio of the radius of the spot on the sea surface viewed by the lidar receiver optics to the mean free path of photons in the water is the significant parameter. For values of this parameter near zero, the decay is determined by the beam attenuation coefficient, while for values greater than ~5–6, the decay is given by the diffuse attenuation coefficient. Between these two extremes Gordon (1982) determined that the interpretation of the effective attenuation coefficient requires, essentially, complete knowledge of the inherent optical properties of the water: the beam attenuation coefficient and the volume scattering function.

As shall be seen later in the discussion of LIF of chlorophyll and its normalization by the water Raman signal, results essentially similar to Gordon's

were found by Poole and Esaias (1982). Thus, it would seem that an oil classification theory is available and that no fundamental obstacles exist that would block its airborne field application. Of course, much more field work needs to be performed on a variety of oil types and under a variety of sea surface and water column conditions.

Once an oil type has been identified (or already known a priori), it is possible to measure the thickness of an oil film. From the results of Kung and Itzkan (1976) the thickness is given by

$$d = -\frac{1}{\kappa_e + \kappa_r} \ln\left(\frac{R'}{R}\right) \tag{6.10}$$

where K_e and K_r are the extinction coefficients of the oil at the laser and Raman backscatter wavelengths, respectively. Consistent with Figure 6.4, R' is the Raman signal obtained while over the oil whereas R is the Raman signal from an uncontaminated segment of the water column outside the slick region.

Figure 6.8 shows several channels of a typical laser fluorosensor output during overflight of an oil slick. These data were taken over a Murban-type oil by the NASA AOL in the scan mode (Hoge and Swift, 1980). Similar data were obtained during the same field experiments by the CCRS fluorosensor in a nonscanning mode (O'Neil et al., 1980). Notice that the Raman backscatter signal in channel 2 (and to a lesser degree, channel 1) depresses when the water column is increasingly obscured by the oil slick. Concurrently, the fluorescence emission in other channels (e.g., channels 3, 4, 5, and 12) increases. The 337-nm laser pulse is attenuated by the oil film immediately before entering the water column. Likewise, the isotropically emitted water Raman at 381 nm is attenuated upon its return passage through the slick. This attenuation is respectively accounted for in the model by the extinction coefficients κ_e and κ_r [Eq. (6.10)]. Upon complete transversal of the slick, the Raman signal that exceeds the *Gelbstoff* background returns to its prior value R. The modulation appearing on the fluorescence and the Raman signals in Figure 6.8 is caused by the AOL conical scanner sweeping the laser beam into and out of the oil slick. Knowing the off-nadir pointing angle of the scanner and the azimuth encoder angle, one can readily calculate the relative position of each LIF spectrum and resulting thickness. Thus, a three-dimensional map can be produced as the result of a single pass over the slick. A typical oil film thickness map is given in Figure 6.9. During this passage across the slick the scanning system mapped the rightmost edge of the slick. The thickness gradient as well as the volume is readily calculated from this data. The percentage of the thickness is given in the included table. Much more field work needs to be done to further validate the theoretical and field experimental techniques discussed here.

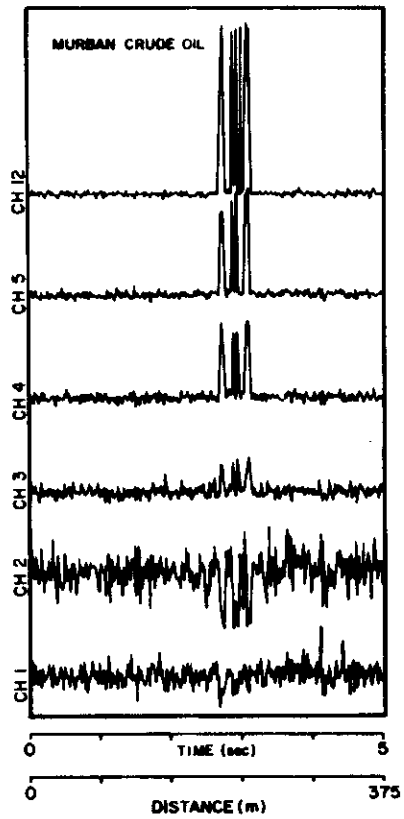

Figure 6.8. Return signal amplitudes recorded in fluorosensor spectral channels 1, 2, 3, 4, 5, and 12 during overflight along right edge of Murban crude oil slick. Conical scanner operation gives rise to 5-Hz amplitude modulation in all Raman and fluorescence (channels 3, 4, 5, 12) channels (Hoge and Swift, 1980).

In coastal and/or harbor regions, the water bodies are likely to be rather turbid. Then, the laser may not penetrate the water column to sufficient depth to produce a usable water Raman signal. Under these conditions one can resort to the oil fluorescence backscatter method of film thickness measurements. Hoge (1983) used the theoretical model developed by Horvath et al. (1971) and later modifed by Kung and Itzkan (1976) to calculate the thickness from the oil fluorescence backscatter. In Figure 6.4*a*, curve *A* shows the background and oil fluorescence, the seawater Raman, and some of the quantities to be discussed for the situation where the airborne lidar is positioned over the oil slick. Curve *B* of Figure 6.4*a* is an analogous situation for a lidar over seawater only. The notation used herein is primarily as found in Kung and Itzkan (1976) and Hoge

THICKNESS RANGE (um)	No. of PIXELS	THICKNESS PORTION (%)
0.25 to 1.00	2901	50.27
1.00 to 2.00	2460	42.63
2.00 to 3.00	148	2.56
3.00 to 4.00	99	1.72
4.00 to 5.00	80	1.39
5.00 to 6.00	15	.26
6.00 to 7.00	11	.19
7.00 to 8.00	11	.19
8.00 to 9.00	6	.10
9.00 to 10.00	7	.12
> 10.00	33	.57

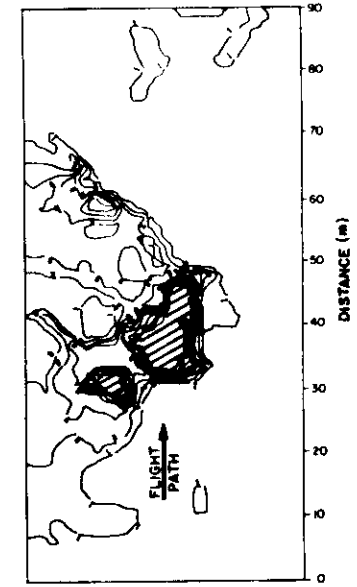

Figure 6.9. Oil film thickness contour plot produced from water Raman backscatter data. Conical scanner azimuth angle, slant range, off-nadir angle, and aircraft velocity allowed determination of spatial position of thickness values (Hoge and Swift, 1980).

(1983). While the aircraft is over the slick, the return signal S_i in the ith channel of the fluorosensor can be expressed as

$$K_i = \eta_i P_0\{1 - \exp[-(\kappa_e + \kappa_i)d]\} + \zeta_i P_0 \exp[-(\kappa_e + \kappa_i)d] + \delta_{ir}\psi P_0 \exp[-(\kappa_e + \kappa_i)d] \tag{6.11}$$

where η_i = fluorescence conversion efficiency in ith wavelength channel for optically thick oil film

P_0 = incident laser power

κ_e, κ_i = extinction coefficient of oil at laser excitation wavelength and at any ith wavelength channel, respectively

d = thickness of oil

ζ_i = fluorescent conversion efficiency of an optically thick seawater column exclusive of water Raman

ψ = Raman conversion efficiency of seawater

δ_{ir} = delta function to select Raman channel r

When the aircraft is outside or beyond the slick, $d = 0$, and the return signals are defined as J_i:

$$J_i = \zeta_i P_0 + \delta_{ir}\psi P_0 \tag{6.12}$$

Assume now that the water mass outside the slick is the same as present beneath the oil film. Evaluate Equations (6.11) and (6.12) at the same fluorescent wavelength $\lambda_i = \lambda_f \neq \lambda_r$ so that $i = f \neq r$. Combining the two resulting equations and solving for the thickness d yields

$$d = -\frac{1}{\kappa_e + \kappa_f} \ln\left(\frac{\kappa_{f,\infty} - \kappa_f}{\kappa_{f,\infty} - J_f}\right) \tag{6.13}$$

where

$$K_{f,\infty} = \eta_f P_0 \tag{6.14}$$

Here $S_{f,\infty}$ is interpreted as the fluorescence signal intensity for an optically thick film at wavelength λ_f. The reason for this definition can be more clearly understood by evaluating Equation (6.11) at λ_f as d approaches large values. Thus, from Equation (6.13), to obtain the oil film thickness, one must have (a) the extinction coefficients of the oil at the laser excitation and fluorescence wavelengths, (b) the fluorescence level from an optically thick portion of the oil, (c) the fluorescence level of the film portion whose thickness is to be measured, and finally (d) the background fluorescence of naturally occurring materials J_f. The quantities described in (b), (c), and (d) can be obtained from the airborne lidar signals, as we shall see. The extinction coefficients κ_e and κ_f must be known a priori or obtained from a sample of oil immediately upon completion of the experiment. Equation (6.13) tells us that the background fluorescence J_f must only be subtracted from the infinite thickness fluorescence level before normalizing the residual fluorescence $K_{f,\infty} - K_f$. The $J_f = 0$ is a physical condition that occurs in deep-ocean areas where little organic material fluorescence is found (Hoge and Swift, 1981a; Leonard et al., 1979). In these types of water the fluorescence depth technique may offer little advantage over the water Raman suppression method. The reason for this is that the water Raman backscatter is rather easily obtained since the attenuation of open ocean water is

minimum. Ocean regions would, however, offer an excellent location to compare the Raman suppression and fluorescence depth thickness measurement techniques.

The $K_{f,\infty}$, K_f, and J_f components are illustrated in Figure 6.10 for a hypothetical nonscanning flight line passage over a wind-driven oil slick having an optically thick nontransparent head and a thinner tail. Using the definitions in Figure 6.10, Equation (6.14) may be written as

$$d = -\frac{1}{\kappa_e + \kappa_f} \ln \frac{F'}{F} \tag{6.15}$$

This illustrates more clearly that the thickness is related to the residual fluorescent component while over the slick F', normalized by the peak or background corrected, saturated fluorescence component obtained from the optically thick portions of the slick, F. Equation (6.15) may be used to calculate the oil film thickness of the spills by using the ratio of the fluorescence from the thinner regions F' to that in the optically thick area F. The extinction coefficients κ_e and κ_f for each oil may be separately measured in the laboratory using fresh oil samples (Visser, 1979; Hoge and Kincaid, 1980; Hoge, 1982).Most probably, the main practical problem with this fluorescence depth technique is finding and/or defining the peak, "saturated" fluorescence level, F, in an optically thick region of slick, as shown in Figure 6.10.

Future oil spill experiment design should be concerned with utilizing an oil that (a) has minimum coagulation properties, (b) is sufficiently lightweight to

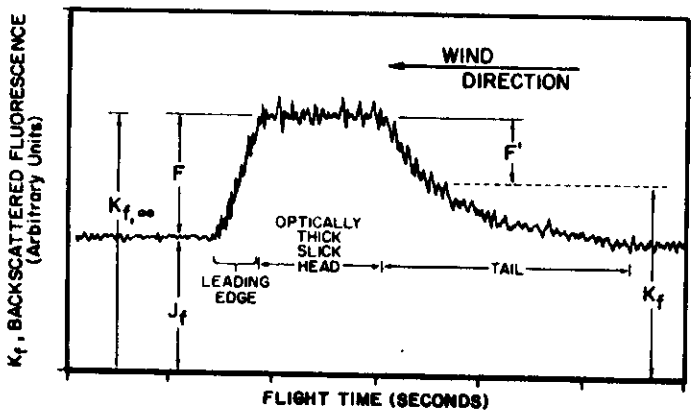

Figure 6.10. Hypothetical backscattered fluorescence signature expected during lidar overflight of wind-driven, optically thick oil slick (Hoge, 1983).

spread rapidly and be deployed in light wind conditions, and (c) contains a sufficiently large amount of oil to form a large optically thick target for airborne sensor investigation.

6.2.1.5 Natural and Man-Made Monomolecular Films

It should be pointed out that there are no doubt some physical and/or physicochemical properties of oil spills on seawater that are not adequately modeled by the Kung and Itzkan theoretical development. For example, all the seawater Raman backscatter suppression modeled by R' in Figure 6.4 and experimentally demonstrated in Figure 6.8 is apparently not due to the κ_e and κ_f optical extinction of the oil film. There are experimental indications that nearly transparent, monomolecular films deployed on the sea surface can similarly suppress the Raman backscatter and the *Gelbstoff* fluorescence (Huhnerfuss et al., 1985). Thus, to some extent the wave-damping properties of oils can be expected to suppress the Raman and *Gelbstoff* fluorescence in addition to the $\kappa_e + \kappa_f$ optical attenuation normally observed during oil film overflights.

A typical oleyl monomolecular film (Huhnerfuss et al., 1978, 1981, 1983a,b) on the ocean will suppress the airborne laser-induced Raman (and dissolved organic fluorescence) signals, as shown in Figure 6.11 (Huhnerfuss et al., 1985). The oleyl alcohol film thickness is on the order of 3–30 nm, and for all practical purposes the laser-induced fluorescence and the optical absorption or extinction for such films is extraordinarily small and undetectable from aircraft altitude. Thus, the gravity waves and capillary wave structure are modified by the film. Such physical changes provide vivid contrast with respect to the surrounding unaltered sea surface and are therefore readily seen by the naked eye (Huhnerfuss and Garrett, 1981; Brockmann et al., 1982). Likewise, these physical surface changes give rise to a change in the wave height and slope probability densities, which determine the laser beam entry and ultimate exit of the Raman scatter and constituents fluorescence from the water column. Note that the oleyl films are only detectable in a differential or relative sense with respect to the surrounding water. If the entire ocean surface were covered with such a slick, it could only be detected in an absolute sense, a task not easily accomplished with the absolute calibration difficulty of today's lidar systems.

The modification of oceanic lidar signals by man-made monomolecular slicks serves as a warning that naturally occurring slicks (Garrett, 1983) can give a similar modification of lidar signals from the ocean surface and water column. Few locations in the world's oceans are devoid of these perturbing natural slicks. Accordingly, more effective means must be found to quantitatively study monomolecular slicks as well as deal with their effects on lidar measurements. The absolute calibration of oceanic lidars will probably help. The concurrent operation of other sensors measuring surface backscatter and emission (micro-

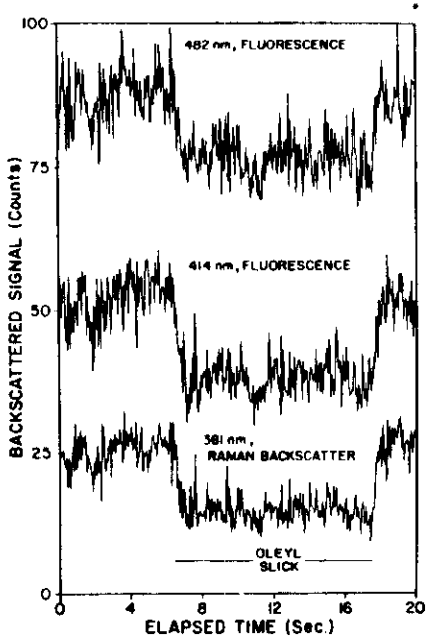

Figure 6.11. Profiles of 337.1-nm laser-induced fluorescence of dissolved organic material and water Raman backscatter obtained during lidar overflight of oleyl alcohol monomolecular film. For ease of comparison 30 and 60 count biases have been added to 414- and 482-nm profiles, respectively, in order to separate plots physically within single figure (Huhnerfuss et al., 1985).

wave scatterometers and radiometers) is recommended. Additionally, more man-made oleyl alcohol slick field experiments need to be executed both in the presence and absence of natural slicks.

The modification of lidar signals by monomolecular slicks prompts one to propose their use in the possible calibration or improvement of petroleum oil slick measurements. Under the singular assumption that a nonattenuating and nonfluorescent monomolecular film dampens ocean waves in the same way as the oil film, lidar data obtained over a monofilm could be used as the "neighboring sea" baseline against which the oil slick measurements are made. That is, instead of calibrating the Raman depression (and oil fluorescence) against the uncontaminated sea [such as done by the Kung and Itzkan (1976) technique], the comparison is performed against a monomolecular film deployed near the oil slick. Then, the Raman depression over the oil film will be attributed to the optical extinction $\kappa_e + \kappa_r$, as prescribed by the Kung–Itzkan model. Figure 6.12*a* shows a hypothetical or expected airborne lidar water Raman

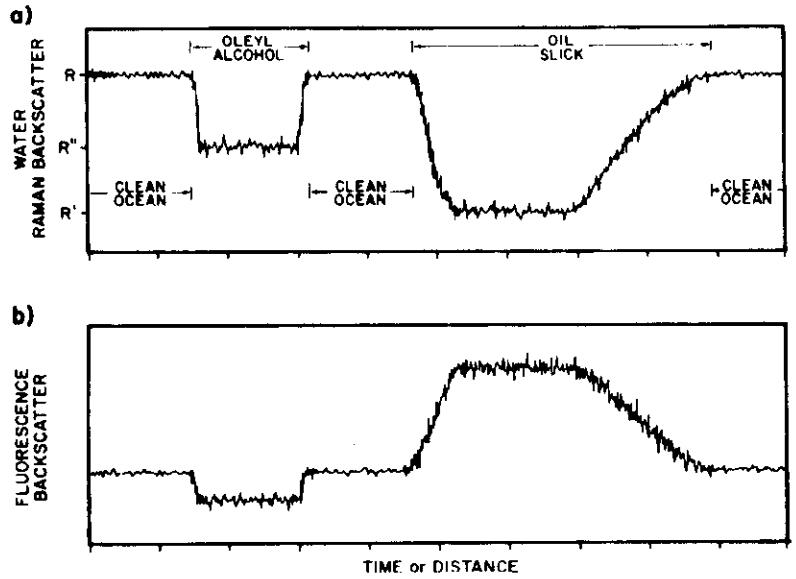

Figure 6.12. (*a*) Anticipated airborne laser-induced water Raman backscatter profile expected during sequential overflight of oleyl alcohol monomolecular film and oil slick both deployed on clean sea surface. (*b*) Airborne laser-induced fluorescence backscatter profile expected during overflight of oleyl alcohol film and oil slick.

backscatter profile that would be obtained over an oleyl alcohol monomolecular film deployed upon a "clean" sea surface near a target oil slick. This expected composite signature is assembled on the basis of separate airborne lidar observations of an oil slick (Hoge and Swift, 1980) and a monomolecular film (Huhnerfuss et al., 1985), examples of which were separately given in Figures 6.8 and 6.11. In the area covered by the monomolecular film, the seawater Raman backscatter decreases as a result of modifications of the laser beam and fluorescence backscatter spatial distribution caused by capillary and small gravity wave damping (further discussion is Section 6.2.3). After again crossing the clean sea, the oil slick is encountered, and the water Raman decreases because of both (a) the capillary and small gravity wave damping and (b) the attenuation of the laser and sea Raman backscatter by the slick material. Assuming the wave damping by the oil slick is the same as that caused by the monomolecular film, the effect described in (a) can be removed by using the monomolecular film measurements as the baseline against which the oil slick measurements are taken. Then, the optical attenuation in (b) as modeled by Kung and Itzkan remains.

Thus, rather than comparing the oil slick water Raman measurements to the surrounding clean, flat sea, as in the original Kung–Itzkan model, they are instead compared to the water Raman values obtained while over the monomolecular film. As a result of this experimental technique and data analysis procedure, the oil film thickness measurement, for example, would have less error contribution by wave-damping effects due to the oil.

Figure 6.12*b* shows a fluorescence backscatter profile that would be expected as the result of these same experimental conditions. Here, the *Gelbstoff* fluorescence is suppressed by the oleyl alcohol film, but this type of suppression is far exceeded by the oil fluorescence, as shown is the rightmost portion of Figure 6.12*b*.

The composite monomolecular film, oil slick, and seawater Raman signatures illustrated in Figure 6.12*a* are based on separately available airborne lidar data obtained to date (Figures 6.8 and 6.11). With this supporting experimental evidence, the Kung–Itzkan flat-sea model can be modified or redeveloped to incorporate the physical effects observed. Figure 6.13 (curve *C*) shows the expected suppression of the clean, open-sea lidar spectrum while over a monolayer. Also shown in Figure 6.13 is the expected spectrum (*B*) to be found over the clean sea. (Curve *B* is also given in Figure 6.4*a* for ease of compari-

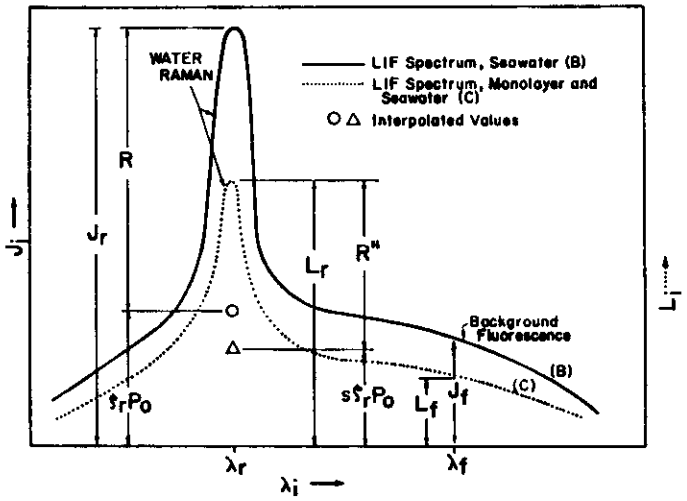

Figure 6.13. Theoretical airborne laser-induced emission spectrum expected while over a monomolecular film deployed on clean sea surface (curve *C*). Wave-damping effects coupled with lidar off-nadir observational angle can both lead to observed reduction of spectral backscatter emission relative to that found over clean sea (curve *B*).

son.) A suppression factor, $s = R''/R$, can be calculated from the data, such as given in Figure 6.11. This suppression factor is valid only for (a) sea surface conditions existing on a particular day and (b) lidar off-nadir viewing angle used (see Section 6.2.3 for further discussion). The channel-to-channel gains for the AOL were not well known during the time period of the monomolecular film experiment. For this reason also, the suppression factor shown herein may not be representative of values measured in figure experiments.

As before from the experimental data of Figure 6.11 (and as conceptually depicted in Figures 6.4*a*, 6.12, and 6.13), the integrated water column Raman found over the monomolecular film, R'', is related to the clean-sea Raman signal R by $R'' = sR$. Or, the airborne laser-induced water Raman signal obtained over the monomolecular film is some measurable fraction s of the water Raman signal obtained over the clean sea. Using procedures similar to those of Kung and Itzkan (1976), the flat-sea model can be renormalized against a monomolecular film (instead of the clean sea) to obtain

$$d = -\frac{1}{\kappa_e + \kappa_r} \ln \frac{R'}{sR} \tag{6.16}$$

which shows that the thickness is related to the Raman component while over the oil slick R' normalized by the suppressed Raman component over the monofilm, sR. The result in (6.16) is not totally unexpected. Furthermore, in the absence of a monomolecular film $s = 1$ and the expression reduces to the original Kung–Itzkan thickness Equation (6.10). Equation (6.16) may be used to calculate the film thickness of oil spills using the ratio of the water Raman over the oil to the water Raman signal observed over the monomolecular film.

Figure 6.14 illustrates the impact upon the lidar measurement and data system of including the wave-damping effects within the oil film thickness calculation [Eq. (6.16)]. For $s = 1$ no suppression has occurred, and the oil film thickness is as shown in the lowermost curve for a Murban-type oil. From Table 6.3, the extinction coefficients for Murban at the laser, Raman, and fluorescence wavelengths of 337.1 and 381 nm are 265 and 95 mm^{-1}, respectively (Hoge and Swift, 1980). Note that wave-damping effects immediately consume 40% of the dynamic range of the instrument for a suppression factor $s = 0.6$ (uppermost curve in Figure 6.14). Comparing Figure 6.11, also, one can see that the oil film optical extinction effects can now only start at ~600 counts for an assumed 10-bit (1024 digital count) lidar data system. Note further that the largest thickness error occurs at the thickest portion of the oil film and that this error can easily approach one order of magnitude. The smallest thickness errors due to wave-damping effects occur in the thinner portions of the slick. It thus appears that oil film thickness estimates could be significantly improved if

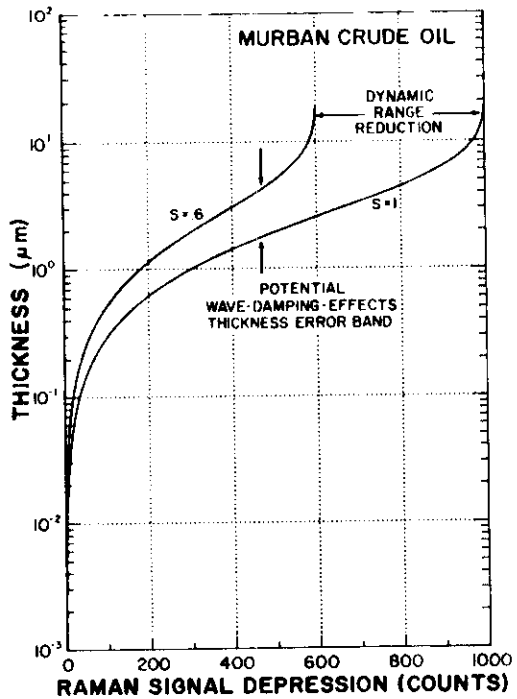

Figure 6.14. Dynamic range suppression of oceanic lidar data acquisition system caused by wave-damped signal reduction effects. Resulting potential errors in measurement of oil film thickness are nonlinear functions of water Raman signal depression.

monofilms are used for the baseline measurement to reduce wave-damping effects errors.

In Sections 6.2.1.4 and 6.2.1.5 we have devoted what would seem to be an inordinate amount of space to a subject that might by some be considered less important than the upcoming section on ocean volume measurements. However, an attempt has been made in these latter two sections to use the measurement of sea surface phenomena to illustrate the quantitative lengths to which lidar measurements may ultimately be extended. Lidar remote sensing is in its infancy. No doubt more quantitative models and field experiments can rightfully be expected in future years.

6.2.2 Measurements in Ocean Volume

This section will focus on the measurements in the volume below the ocean surface. While these volume measurements are affected by the state of the surface above it, we will forego the details of the effect of the sea surface waves on the volume measurements until Section 6.2.3.

6.2.2.1 Biological Measurements in Ocean Volume

The world's oceans comprise about three-quarters of Earth's surface and are responsible for approximately one-third of all primary production (Struum and Morgan, 1981). Primary production in marine waters is very closely correlated with chlorophyll *a* concentration (El-Sayed, 1970; Sorenzen, 1970). This is a key finding, not only because chlorophyll *a* is the principal ingredient in the photosynthetic process, but also because chlorophyll emits measurable fluorescence in virtually direct proportion to its concentration (Yentsch and Menzel, 1963). Thus, primary production can apparently be inferred by measurement of fluorescence. While this is a very simplified interpretation of a highly complex process, it forms the basis of remote sensing of chlorophyll and the ultimate goal of inferring primary productivity and total biomass in the ocean. However, the remote sensing of phytoplankton was assured only when it was found that the concentration could be evaluated from the in vivo chlorophyll fluorescence, that is, without extracting the pigment from the organism (Sorenzen, 1966).

The laboratory studies of Hickman and Moore (1970) and Friedman and Hickman (1971) strongly suggested the feasibility of chlorophyll measurements from remote platforms. Mumola and Kim (1972) sensed in vivo fluorescence of naturally occurring phytoplankton in the Chesapeake Bay from a pier-based platform. These experiments led to the airborne (helicopter) detection of chlorophyll (Kim, 1973). Mumola et al. (1973) suggested that more accurate chlorophyll measurements could be obtained if the four major color groups of algae (red, blue-green, green, and golden brown) were excited with a four-wavelength laser. The concept is discussed by Mumola et al. (1973) and by Browell (1977).

Without resorting to a maze of excitation and emission spectra, the reader can gain a general understanding of the laser-induced phytoplankton technique by referring to Figure 6.15. Adapted from Govindgee and Govindgee (1974), the lower portion of Figure 6.15 shows pigments important to the photosynthetic process. The arrows and annotation of the pigment blocks serves to label the dominant color of light absorbed as well as the energy transfer among (and spectral emission from) various major pigments. A specific and typical example of the fluorescence spectra observed during remote airborne excitation of phytoplankton with a high-power 532-nm blue-green pulsed laser (L) is shown in the upper portion of Figure 6.15. This spectrum was taken with the AOL during the Superflux experiments conducted in the Chesapeake Bay (Campbell and Thomas, 1981). The phycoerythrin and chlorophyll fluorescence emission band peaks are labeled as *P* and *C* and occur at ~580 and ~685, respectively. No carotenoid or phycocyanin fluorescence was observed. The water Raman back-

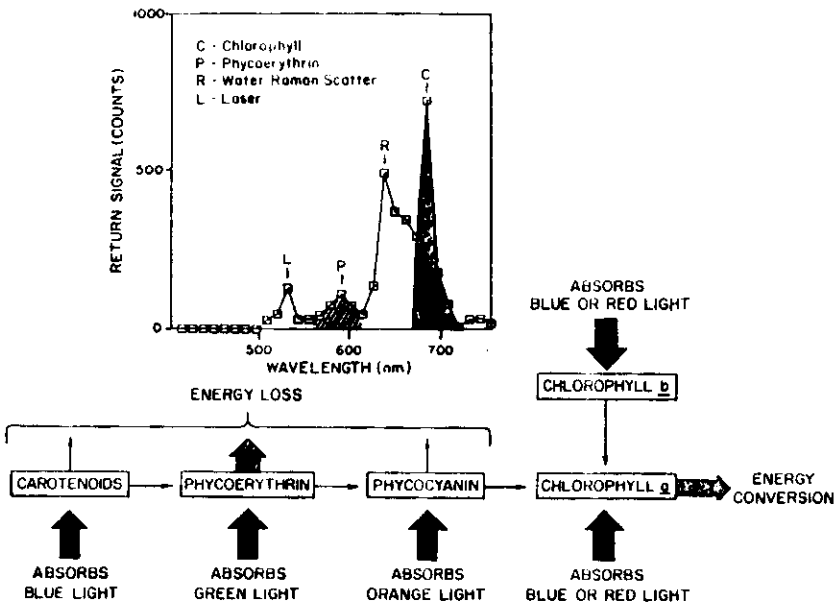

Figure 6.15. Model of energy absorption, transfer, and emission by and between principal pigments important to photosynthetic process (Govindgee and Govindgee, 1974; Browell, 1977). Inset: actual airborne 532-nm laser-induced spectrum of waterborne marine phytoplankton. This spectrum obtained in Atlantic Ocean near mouth of Chesapeake Bay (Hoge and Swift, 1981c).

scatter line is labeled *R*. The laser-induced Raman scatter is an inherent property of the water molecules in which the phytoplankton are growing and will always be produced even when no organisms are present. The water Raman can obscure (or cannot be distinguished from) phytoplankton fluorescence emissions that have narrow linewidths and occur at ~647 nm. The strongest water Raman emission is the OH^- stretch Stokes line and is situated at ~3350 cm^{-1} from the laser. Thus, the choice of laser wavelength is dictated not only by optimum excitation wavelengths of the target but also by the placement of the water Raman line to avoid obscuration of desired emission spectral bands from the waterborne target species. Selection of laser wavelength as well as the useful application of the water Raman emission for correction of spatial variability of water column attenuation properties is discussed subsequently in this section.

Concerning the excitation wavelength selection, the four previously mentioned wavelengths were chosen only for chlorophyll stimulation. It is now well known that the ~3350-cm^{-1} OH^- stretch water Raman backscatter can be easily detected remotely. Thus, an improper choice of the excitation wavelength could yield Raman interference in the 685-nm chlorophyll band. For example, one would not choose one of the excitation wavelengths to be ~557 nm since this would produce a Raman emission at 685 nm and would interfere simultaneously with the chlorophyll emission. As we shall discuss later, one would not choose an excitation wavelength at ~486 nm since this would similarly produce a Raman backscatter line at ~580 nm, the wavelength position of the phytoplankton phycoerythrin pigment fluorescence. Browell (1977) performed an analysis of lidar systems for phytoplankton studies and concluded among other things that the remote measurement of chlorophyll requires (a) optimum excitation wavelengths and (b) careful measurement of the water column attenuation coefficients. Regarding wavelength selection, a prototype laser was developed to stimulate chlorophyll at 454.4, 539.0, 598.7, and 617.8 nm and observe the resulting 685 nm fluorescence. This system was last operated in 1980 during the Superflux experiments in the Chesapeake Bay (Jarrett et al., 1981). The method used to handle the water column spectral attenuation coefficients will now be discussed in more detail.

The analysis of Browell (1977) pointed to the need for accurate knowledge of the water attenuation coefficients. Airborne field experiments subsequently demonstrated that the laser-induced water Raman backscatter could be used to effectively remove chlorophyll fluorescence signal variability due to horizontal spatial variations in water column attenuation. Bristow et al. (1981) reported the highly successful use of water Raman normalization of chlorophyll signals during flights over the fresh water of Lake Mead. Likewise, Hoge and Swift (1981b) reported similar successes during experiments in the marine waters of the North Sea, the Atlantic Ocean, and Chesapeake Bay estuary (Hoge and Swift, 1981c) and the northwestern Atlantic Ocean (Hoge and Swift, 1983b; Hoge and Swift, 1985). Figure 6.16*a* shows profiles of chlorophyll *a* fluorescence and water Raman backscatter along flight line 8 of a June 23, 1980, mission in the Chesapeake Bay. The effect of normalizing the chlorophyll fluorescence with the water Raman signal is seen by noting Figure 6.16*b*. The declining Raman signal gives a corresponding increase in the chlorophyll fluorescence. During four separate missions flown in June 1980 over the lower Chesapeake Bay and outflow into the Atlantic Ocean, the water-Raman-normalized chlorophyll *a* fluorescence yielded correlation coefficients of $r = 0.97$, 0.92, 0.81, and 0.82 in separate linear regressions against ship truth data. Without Raman normalization this level of agreement could not be obtained. The importance of applying Raman corrections to the various laser-induced fluorescence responses to correct for spatial variation in water column optical transmission properties cannot be overstressed since it is necessary for the precise recovery of even relative concentrations of various parameters.

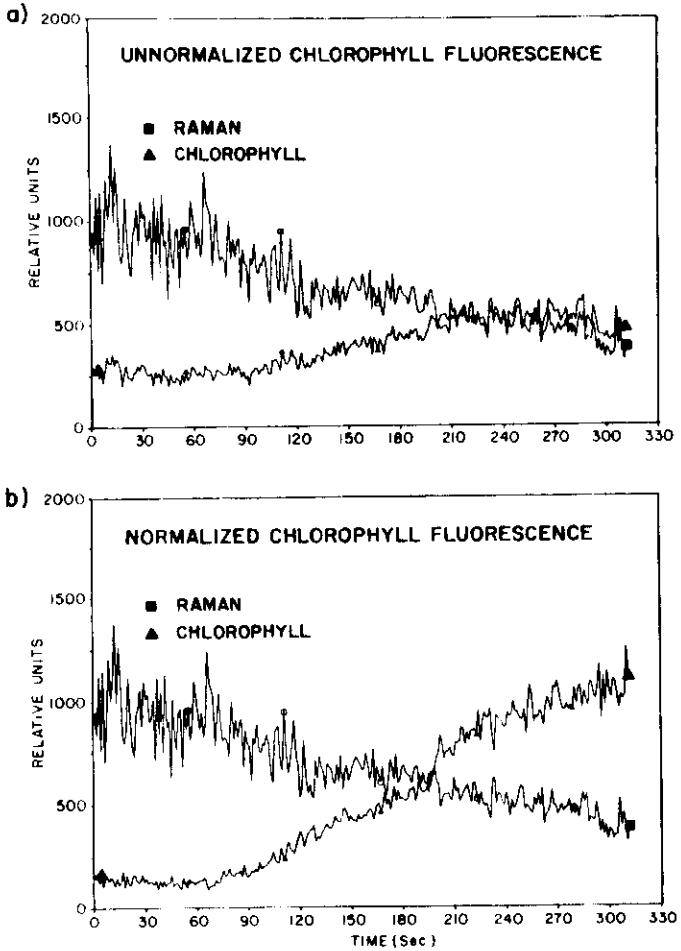

Figure 6.16. (*a*) Profiles of airborne laser-induced water Raman backscatter and unnormalized chlorophyll *a* fluorescence obtained during flight experiments in coastal waters of Atlantic Ocean. (*b*) Same profiles as in (*a*) except that chlorophyll *a* fluorescence corrected for spatial variability of water column attenuation by normalizing with water Raman backscatter signal strength (Hoge and Swift, 1981c).

The water Raman normalization technique has been successfully demonstrated in lake, estuary, and marine bodies and is well established. The Monte Carlo simulation studies of Poole and Esaias (1982) showed that Raman normalization produces effectively linear response to chlorophyll concentration, particularly for excitation at 480 and 532 nm. Poole and Esaias (1983) suggested, however, that the Raman signal should be used cautiously, if at all, in linear algorithms to measure beam attenuation or irradiance (diffuse) attenuation coefficient in a quantitative sense. These latter results are in accord with those of Gordon (1982) and Poole and Esaias (1982).

Zimmerman et al. (1976) were apparently the first to observe the laser-induced fluorescence emission of in vivo phycoerythrin using a shipboard lidar remote sensing system. They conducted five stations in the marine waters of the Atlantic Ocean/Chesapeake Bay mouth. They found the 580-nm fluorescence peak and further discovered that its strength (as well as that of chlorophyll fluorescence) increased upon approaching the bay mouth. Celander et al. (1978) obtained the 337.1-nm laser-induced fluorescence emission spectra of six freshwater algae species. Using cultures of unknown concentration, they found spectral bands at 380 (water Raman), 460, 585, 665, and 725 nm. They did not identify the 460- and 585-nm peaks; however, the latter is probably phycoerythrin. Some of the species revealed bands centered near 515 nm and were also not identified. In general, the freshwater species displayed stronger blue-green fluorescence than marine algae.

The airborne LIF of phycoerythrin was observed in 1979 during experiments conducted in the North Sea and in the Chesapeake Bay (Hoge and Swift, 1981b). (A typical airborne LIF spectrum obtained by the AOL was previously given in the inset of Figure 6.15.) Airborne laser-induced phycoerythrin fluorescence was also observed in 1981 in the Nantucket Island–New York Bight region of the north Altantic Ocean (Hoge and Swift, 1982a). Furthermore, airborne laser observations of phycoerythrin have been reported during dedicated studies of Gulf Stream Warm Core Rings (Hoge and Swift, 1983b). Figure 6.17 shows the geographic location of WCR 82-B that was intensively studied in the spring of 1982. Figure 6.18*a* provides profiles of normalized chlorophyll and phycoerythrin fluorescence over this warm core ring (WCR) (Hoge and Swift, 1983b) during a mission flown on April 20, 1982. The water Raman shown in Figure 6.18*b* indicates that the optical transmission is higher in the inner portions of the ring. Likewise, a separate infrared sensor yielded data (Figure 6.18*c*) that verifies the core has a higher temperature than the boundaries. As before, a 532-nm pulsed, frequency-doubled Nd–YAG laser was used as the primary excitation source. The aircraft crossed the ring boundaries approximately 200 s from each end of this flight line. Elevated chlorophyll *a* and phycoerythrin fluorescence levels are found in this high-velocity boundary region that surrounds

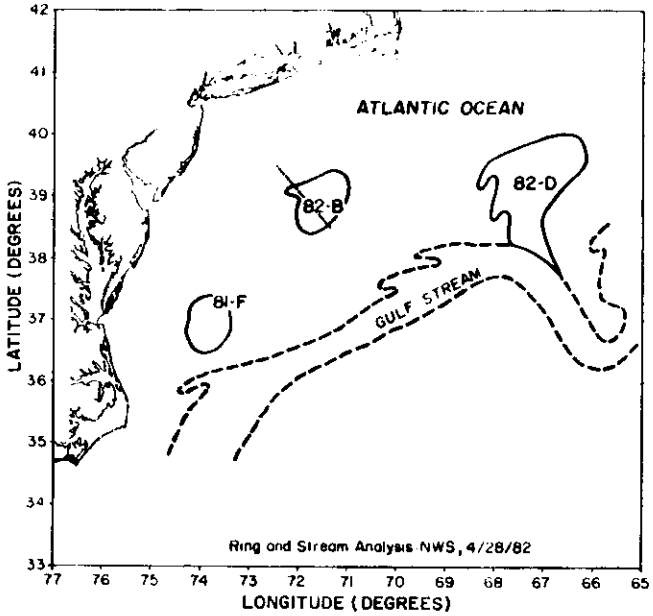

Figure 6.17. Location of Warm Core Ring 82-B at time of airborne experiment described in text. One of numerous airborne laser experiment flight lines shown across entire ring. Profiles of laser-induced chlorophyll *a* and phycoerythrin fluorescence as well as water Raman backscatter obtained in this particular flight line given in Figure 6.18 (Hoge and Swift, 1983b).

the ring. Figure 6.19 is a scatter plot of the chlorophyll and phycoerythrin segments labeled *A*, *B*, *C*, *D*, and *E* in Figure 6.18*a*. These scatter plots demonstrate the coherence of the chlorophyll and phycoerythrin fluorescence observed. The correlation coefficients between phycoerythrin and chlorophyll *a* fluorescence varied respectively from 0.85 to 0.653, as shown in the Figure 6.19. The proportion of phycoerythrin to chlorophyll *a* fluorescence is seen to be higher within the ring than in either of the boundary regions. The significance of these findings is at present not well understood. It has been suggested that these phycoerythrin–chlorophyll *a* ratio variations are caused by speciation changes. The ship data from these experiments has not yet allowed this to be proven conclusively. To illustrate the potential importance of airborne lidar fluorosensing to the study of mesoscale oceanographic features, Figure 6.20 shows a chlorophyll fluorescence contour map generated from data such as previously shown in Figure 6.18. Similar maps of phycoerythrin fluorescence and Raman scatter can also be generated. Such features can be mapped in 2–3 h depending

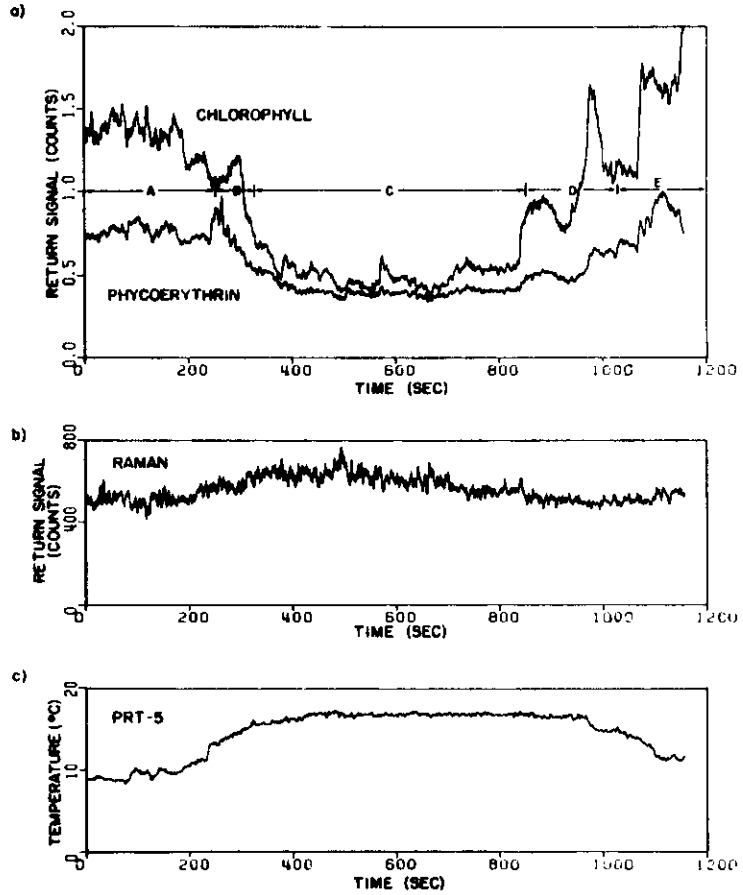

Figure 6.18. Profiles of airborne laser-induced (*a*) chlorophyll *a* and phycoerythrin fluorescence, (*b*) water Raman backscatter, and (*c*) infrared radiometer surface temperature obtained during flight across Warm Core Ring 82-B (Hoge and Swift, 1983b).

on the type of aircraft platform used and the flight pattern configuration. Such mapping can also be executed during overcast conditions or during other such times that a satellite coverage is not available (including darkness).

A shipboard laser system for in vivo stimulation of the water constituents is suggested to complement the usual chlorophyll extraction, flow-through fluorescence, and taxanomic observations. Such shipboard laser experiments should avoid water-pumping systems and use the forward end of the ship to reduce

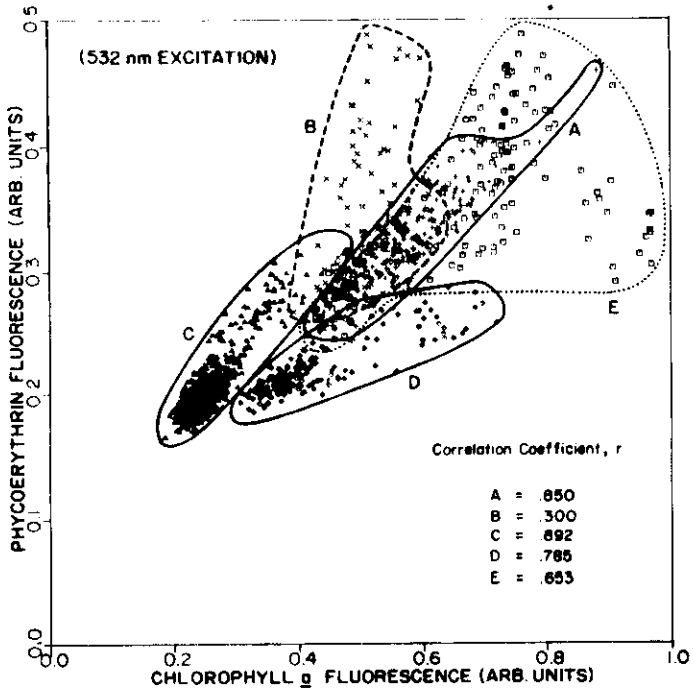

Figure 6.19. Scatter diagram of chlorophyll *a* and phycoerythrin fluorescence occurring within several discrete sections of flight line across Warm Core Ring 82-B. Portions *A*-*E* correspond to those regions of flight line in Figure 6.18 (Hoge and Swift, 1983b).

possible disturbances that may rupture fragile organisms. This is particularly true if the experiments are performed in estuarine regions such as the Chesapeake Bay. Exton et al. (1983) showed that Chesapeake Bay estuarine samples are dominated by cryptophytes whose phycoerythrin fluorescence was significantly modified by a pumping circulation system that apparently ruptured the cell walls of the organism. On the other hand, Exton found that coastal marine samples found near the bay mouth contained mostly cyanobacteria whose stronger cell walls are not easily disrupted. The phycoerythrin fluorescence from these plankton were not noticeably affected by pump agitation. Apparently, a shipboard laser system could assist scientists to some degree with speciation. Houghton et al. (1983) showed that a pier-based lidar system having 7.5 nm resolution was capable of detecting and distinguishing differences between the phycoerythrin spectral from cyanobacteria (peak at 576 nm) and cryptophytes

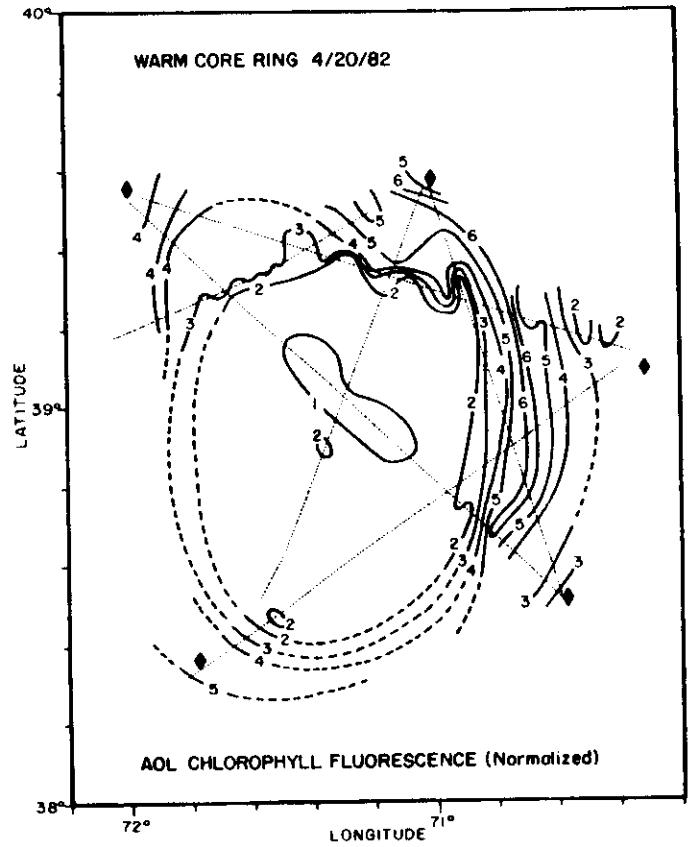

Figure 6.20. Contour plot of chlorophyll *a* fluorescence produced from data such as presented in Figure 6.18. Similar contour plots of phycoerythrin fluorescence can also be generated in similar fashion (Hoge and Swift, 1985).

(peak at 586 nm), both of which can be major components of nearshore/estuarine nanophytoplankton communities. Coupled with recent flow cytometers (Yentsch and Yentsch, 1984), advances such as these promise improved water surface truth for validating airborne laser results.

The reader should note that the phycoerythrin plots herein are not expressed in milligrams per cubic meter such as is normally done for chlorophyll. The reason is that phycoerythrin extraction and measurement techniques are not as well developed as for chlorophyll. A method for the extraction and quantifica-

tion of phycoerythrin from algae has been recently described (Stewart, 1982). The effectiveness of this reported technique is not known.

Because of the specificity of the lidar data, it is very useful for validating passive sensors operating alongside the lidar. However, a single, combined active-passive sensor would allow still more applications than two separated instruments on the aircraft. A combined active-passive ocean color instrument allows reasonably rapid calibration of both modes, studies of the fluorescence-to-pigment ratio and its possible link to phytoplankton fluorescence yield, validation of passive ocean color in-water algorithms and instrumentation as discussed above, and studies of the effect of sea state on passive ocean color measurements. Such studies will probably be reported in future years since the NASA AOL fluorosensor has recently been modified to operate concurrently as a multichannel passive ocean color sensor.

Future space-borne fluorosensors should carry a comparison passive color sensor to provide for comparative data in the same footprint. Then global validation and comparison techniques can be rapidly assessed.

6.2.2.2 Chemical Constituents in Ocean Volume

Probably the first airborne lidar detection of chemicals in the environment was reported by O'Neil et al. (1973). They used a CW helium-cadmium laser at 442 nm to excite fluorescence of the effluent from a paper mill having high concentrations of lignin sulfonates. Bristow (1978) also reported the airborne laser-induced fluorescence of the outflow of this paper mill by using a 337-nm pulsed nitrogen laser. The main features of the work by Bristow (1978) has also been summarized by Measures (1984). The lignin sulfonate laser-induced emission spectrum is quite similar to that of naturally occuring dissolved organic carbon (DOC), and this could easily preclude the direct, unambiguous measurement of pulp mill effluent. It is well known that the fluorescence spectrum of natural waters is quite broad and typically devoid of identifiable spectral characteristics. However, the total signal under the fluorescence emission curve is more informative and is apparently proportional to organic loads in the water bodies (Measures et al., 1975). But emission amplitudes are difficult to calibrate absolutely, and Bristow et al. (1973) suggested that the OH^- stretch water Raman be used as a reference to calibrate the return signal.

Numerous investigators have found that the water-Raman-normalized fluorescence of natural water is to some degree correlated to the total organic content of the water (Measures et al., 1975; Zimmerman and Bandy, 1975; Bristow and Nielsen, 1981). These findings are in general agreement with earlier worker's conclusions (Kalle, 1966; Christman and Ghasseni, 1966; Sylvia et al., 1974). After a very detailed laboratory feasibility study Bristow and Nielson

(1981) concluded that the Raman-normalized fluorescence emission induced in surface waters by UV radiation could be used to provide a unique airborne remote sensing capability for monitoring the concentration of DOC. At present we know of no airborne lidar field experiments that have been conducted expressly to measure surface water DOC. However, Hoge and Swift (1982b) used the organic material to map fronts in the German Bight. Water Raman normalization was recommended by Bristow and Nielsen (1981), but for the high-DOC levels found in coastal regions, the UV laser-induced Raman may be difficult to obtain reliably.

While the laser-induced fluorescence emission signal of naturally occurring organic materials (*Gelbstoff*) is highly correlated to the amount of DOC (Bristow and Nielsen, 1981), the use of this signal in remote measurements is complicated by the fact that a major DOC constituent (fulvic acid) has been shown to be affected by both pH and by trace metals (Saar and Weber, 1980). The fluorescence of DOC is quenched, or reduced in intensity, by complexation with metals (Ryan and Weber, 1982). Furthermore, the quenching is wavelength dependent (Vodacek and Philpot, 1985), with the long-wavelength components in general being quenched more than the shorter wavelengths as the metal concentration increases. If one has thorough knowledge of the pH of the body of water (e.g., a lake), the concentration of metal may possibly be inferred from the wavelength-dependent quenching. Since iron causes more quenching than aluminum and copper (Vodacek and Philpot, 1985), the dominant metal present in the lake may also be required information. Knowledge of the amount of metals complexed, or associated with organics, is important since they are highly toxic in the free state. However, if the acidity of the lake increases, through acid rain or other causes, the complexing can be disrupted, the metal freed, and accordingly the toxicity will rise. Although low pH is also toxic, elevated levels of, for example, aluminum appear to have serious effects (Cronan and Schofield, 1979).

Vertucci (1985) found that the differences in the laser-induced fluorescence spectra of natural lake waters were sufficient to be used in regression models to predict sample DOC, pH, and aluminum. The prediction accuracy of DOC and aluminum was improved when the data were analyzed in separate pH classes. The studies were performed to determine the potential of airborne laser fluorosensing for remotely detecting and measuring lake acidification.

Yentsch (1973) was perhaps the first to suggest in a laser remote sensing forum that salinity might be inferred from the detection of the organic material or yellow substances or *Gelbstoff*. He showed that a high degree of correlation exists between yellow substances and salinity where the Merrimack River mixes with Gulf of Maine waters. Figure 6.21 shows a plot of laboratory laser-induced fluorescence of Savannah River/Atlantic Ocean water samples as a function of

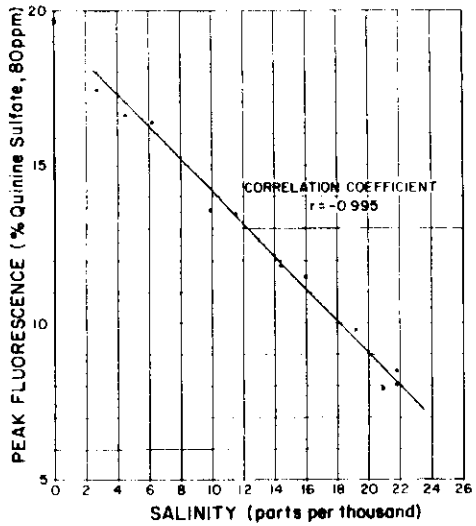

Figure 6.21. Variation of 337.1-nm laser-induced fluorescence of dissolved yellow substances and salinity. Samples gathered in vicinity of Savannah River mouth.

salinity. These latter data were provided by James Yungel of the AOL support laboratory. The reference signal for the organic fluorescence in the latter figure was an 80-ppm solution of quinine sulfate. To use this latter technique for remote measurement, the organic material must be conserved, that is, there must be no unknown sources or sinks. There are many conflicting opinions as to the source of the dissolved organic material and whether the sinks (if any) can be properly accounted for. Rather than discussing the merits in detail here, we suggest that the technique be tried in an airborne field environment selected to minimize the source/sink issues.

Airborne lidar observation of the sulfate ion Raman scatter may provide a salinity measurement method and a way to avoid the above problems. Houghton (1973) suggested that salinity might be measured remotely by detection of the Raman spectrum of the sulfate ion, SO_4^{2-}. The technique is based on the constancy of composition, which says that the ratio iof SO_4^{2-} to chlorine is a constant regardless of salinity. He recommended standardizing the SO_4^{2} by using the OH^- stretch water Raman signal. Relative to remote sensing, several serious problems immediately present themselves. First, the SO_4^{2-} Raman is weaker than the OH^- stretch water Raman and only has a peak strength that is approximately equal to the H_2O bending mode Raman line. Second, the spectral width

of the SO_4^{2} Raman is significantly less than the OH^- stretch water Raman depending on the laser linewidth. This suggests the need for a high-resolution spectrofluorometer to allow quantitative utilization of the spectra. Third, the sulfate ion Raman rides upon, and can easily be obscured by, the naturally occurring dissolved and particulate organic fluorescence background. Ironically, the organic fluorescence interference is strongest in coastal regions where salinity maps would be most useful. The degree to which these problems affect the airborne remote detection and utilization can only be assessed by actual field experimentation. As Houghton (1973) points out, it will probably be necessary to utilize a multichannel fluorometer. This of course would allow the use of interpolation techniques (Kung and Itzkan, 1976) to accommodate or correct for the organic fluorescence.

Perhaps the first controlled chemicals to be remotely sensed by lidar were organic dyes dumped into the Atlantic Ocean for tracing purposes. Hoge and Swift (1981a) reported the absolute measurement of tracer dye concentration in the ocean using airborne laser-induced water Raman backscatter as the calibration reference signal. O'Neil et al. (1980) overflew the same dye spill and used the dye fluorescence data to conclude that such Rhodamine WT fluorescence could easily be distinguished from oil spill fluorescence. Hoge and Swift (1981a) used the scanning AOL fluorosensor mode to map the concentration down to about 2 ppb.

Figure 6.22 shows a typical lidar fluorosensor response to a dye spill in the open ocean. About 18.9 l. of 20% solution of Rhodamine WT were used in these experiments. During this pass the AOL instrument was conically scanning with a full cone angle of 10°. The 5-Hz scan frequency can be seen in the fluorescent data. During this particular pass, the aircraft was principally flown over the leftmost edge of the irregularly shaped dye plume. Thus, the conical scanner during portions of the flight line caused the lidar system to view the plume only during approximately each half-cycle of the scan frequency of 5 Hz. Accordingly, the output response of each LIF channel is amplitude modulated by the successive views into (and away from) the dye plume. During this pass more than 20 incursions into and out of the dye were observed. Shown are channels 2, 11, 20, 22, and 24. Channel 11 is located between the Raman and dye emissions and is included to illustrate the typical fluorosensor response or behavior in spectral regions that have little or no physical participation. Channel 2 is rather closely centered upon the Raman band and contains the major portion of this spectral emission. Note that the Raman signal is approximately 10 times stronger than the dye emission. Also, no discernible Raman suppression is found in channel 2 as the dye is encountered and its fluorescence emission rises as shown in channels 20, 22, and 24. The absence of Raman suppression should be compared to the very noticeable Raman suppression over oil spills (Figure

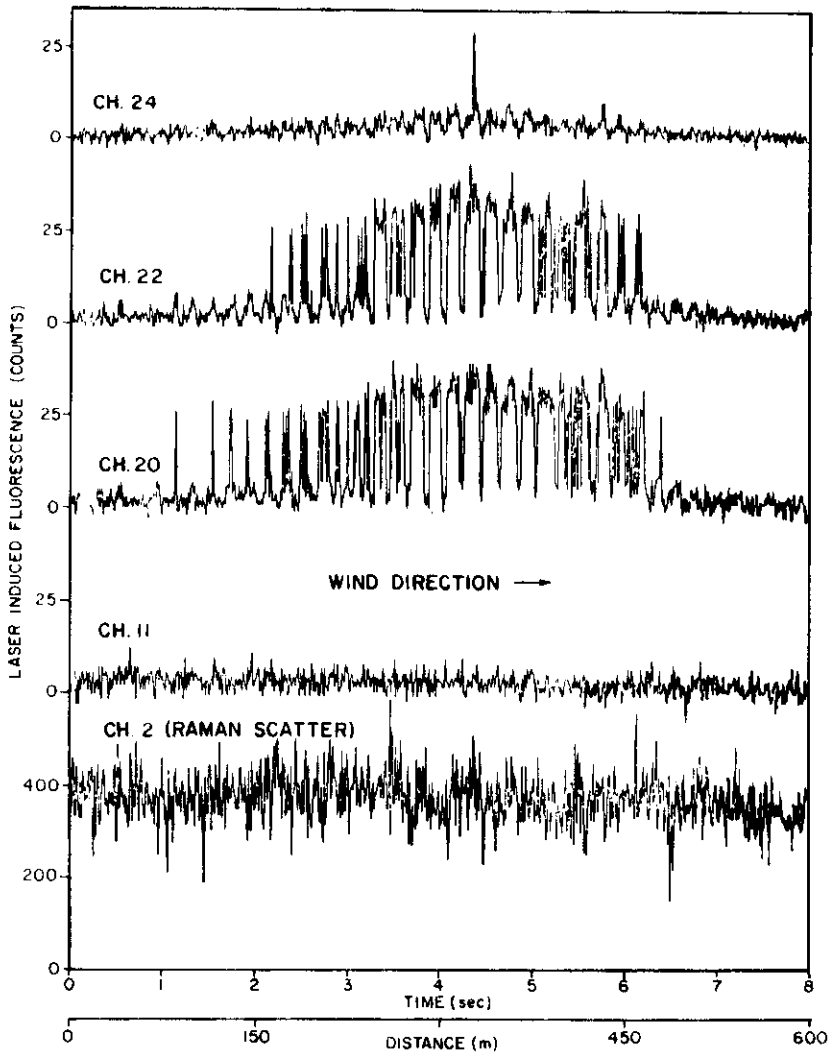

Figure 6.22. Airborne laser-induced spectral emissions from Rhodamine WT tracer dye dispersed in ocean. Channel 2 contained principal portion of water Raman backscatter centered at ~381 nm. Channel 11 included to show typical fluorosensor response in spectral regions not containing Raman and dye emissions. Absence of any Raman suppression in channel 2 shows that dye contributes little attenuation at 337.1 and 381.0 nm. The 5-Hz amplitude modulation of fluorescence is result of conical scanning of system during overflight. All channels contiguous and have bandwidths of 11.25 nm (Hoge and Swift, 1981a).

6.8). These experimentally observed, nondepressed Raman signal data completely agreed with the Canada Center for Remote Sensing laser fluorosensor results obtained over the same dye plume from another aircraft flying at 450 m altitude at the same time (O'Neil et al., 1980). Our interpretation of these channel 2 Raman data is that the dye produces no discernible change in the optical properties of the water column so that the extinction sum $\gamma_e + \gamma_r$ is essentially constant throughout the entire test region both inside and outside the plume. Or viewed another way, the absorption by the dye molecules contributes very little to the attenuation or extinction in the water column at the laser emission wavelength and the Raman wavelength (Hoge and Swift, 1981a). The nondepression of the water Raman signal over this chemical dye spill also suggests, but does not prove, that the Raman depressions found, for example, in deep-ocean phenomenon (such as the boundary of a warm core ring, Section 6.2.2.1) are due to scatter and not absorption.

Figure 6.23 is a dye concentration contour map produced from the corrected channel 20 data shown in Figure 6.22. Azimuthal scan angle data, slant range to the sea surface, as well as roll-and-pitch aircraft altitudes are recorded simultaneously with the spectral channel values to provide a mechanism for projecting the horizontal position of each laser pulse. The roll-and-pitch parameters are provided by a Litton LTN-51 inertial navigation system (INS). Note that the image is in three sections, which must be laid end to end to yield the entire dye plume edge. The conical scan pattern of small dots represents the actual spatial position of the radiated laser pulse intercepting the ocean surface. The contours were produced from the fluorescent intensity values observed at each dot position. Good agreement is found for spatial positions where the conical scan pattern intersects. The contours are labeled in arbitrary units of digital counts. The 10-digital-count contour actually corresponds to a concentration of 3.33 ppb, a 20-digital-count contour to 6.66 ppb, and so on.

A scanning airborne laser fluorosensor has the potential to provide relatively high density dye concentration maps without the need for extensive in situ sampling (Hoge and Swift, 1981a). The technique utilized here requires laboratory calibration with dilute dye concentrations that span the range of the ultimate field dye concentrations. The water Raman intensity must be obtained in both the laboratory and airborne data. The ratio of the fluorescence to Raman signals in the airborne data is compared to the same ratio found in the prepared laboratory dilutions to determine the field concentrations. One of the major errors in this technique involves the water column attenuation coefficient at the laser, Raman, and dye fluorescence emission wavelengths. It can be shown (Hoge and Swift, 1981a), however, that the errors produced by attenuation in the water column are quite manageable, particularly if the water mass can be accurately categorized by the Jerlov (1976) classifications.

Other dye-tracing experiments have been conducted (O'Neill et al., 1981)

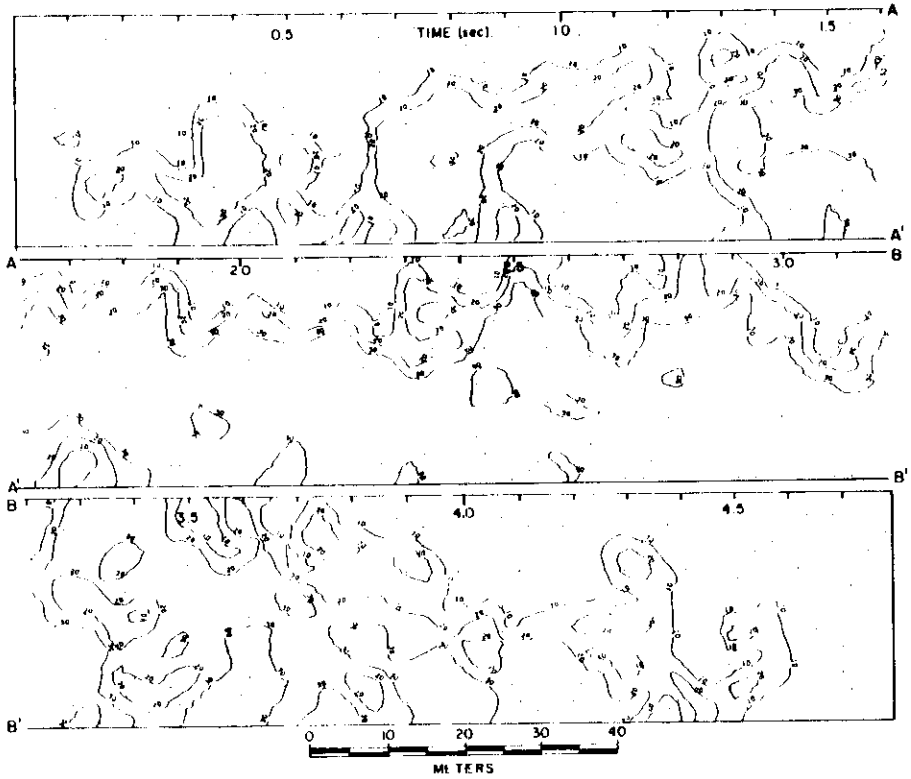

Figure 6.23. Dye concentration contour plot or image produced from channel 20 results in Figure 6.22 together with simultaneously recorded azimuthal scan angle data. Entire contiguous image may be seen in usual configuration by joining three segments of *AA'* and *BB'*, respectively. Roll and pitch of aircraft corrected using data from Litton LTN-51 inertial navigation system. Alternatively, roll and pitch may also be obtained directly from scanning lidar slant range data. Contours labeled as 10 digital counts correspond to 3.33 ppb dye concentration, 20 digital counts to 6.66 ppb, etc. (Hoge and Swift, 1981a).

with the AOL reconfigured to use a neon laser (λ_L = 540 nm). The fluorescence of Rhodamine 6G dye was still observable at a concentration of 4 ppb even though the pulse energy was about 3% of that available when N_2 was used in the same laser cavity. Using a wavelength in the green part of the spectrum, which is better able to penetrate the water than the UV wavelengths, allows the sensor to measure the dye concentration over a longer water column. With a

time-resolved laser fluorosensor and a target substance with a sufficiently short fluorescence lifetime, the concentration as a function of depth could be measured, greatly enhancing the interpretation of such dispersion experiments. The above tracer dye remote measurement technique is of course applicable to the measurement of near-shore and estuarine calculation.

Another application of the tracer dye technique suggested by Hickman (1973) was the remote measurement of temperature. In this method a calibrated mixture of two dyes whose fluorescence emission intensities are temperature sensitive (such as Rhodamine B and Eosin Y) would be deployed together in the water column. The plume would then be excited by a single laser to produce an emission peak at two different wavelengths characteristic of each dye. The ratio of the strength of the two peaks would yield the relative temperature. The absolute temperature calibration would be obtained by in situ sampling. To improve the accuracy of the results, the data should be corrected for salinity effects. Conversely, if the water temperature is already known, salinity variability could be inferred.

6.2.2.3 Ocean and Estuarine Front Detection

When two or more different water masses meet, zones having a high degree of spatial and temporal variability are frequently formed. For example, when lower salinity estuaries and rivers empty into oceanic waters, sites of locally intense mixing and small-scale interaction occur at the boundary of such water masses. The interactions of the water masses may be further enhanced by inherent bathymetric features (shoals, banks, etc.), differing regional wave and current velocities, and temperature–density gradients (Bowman and Esaias, 1977). Conventional techniques cannot easily and economically provide the spatial resolution and wide-area coverage needed to adequately sample within the appropriate length and time scales present in these regions. Airborne lidars have the ability to map large areas over reasonably synoptic scales and with high spatial resolution. Since fronts or zones of convergence tend to concentrate biological and chemical waterborne constituents (Sick et al., 1978), the laser-induced spectral fluorescence characteristics of lidars appear particularly appealing. Furthermore, the on-wavelength backscatter from the surface and water column potentially allows measurement of (a) local surface wave structure modification or gradients and (b) entrained/resuspended sediments and/or particulates, respectively. This section will address the modest and limited application efforts to date.

Hoge and Swift (1983c) have shown that the depth-resolved water Raman backscatter waveform can reveal turbidity cell structure in the ocean. This cell structure is obtained by selecting and plotting two separate depth-resolved chan-

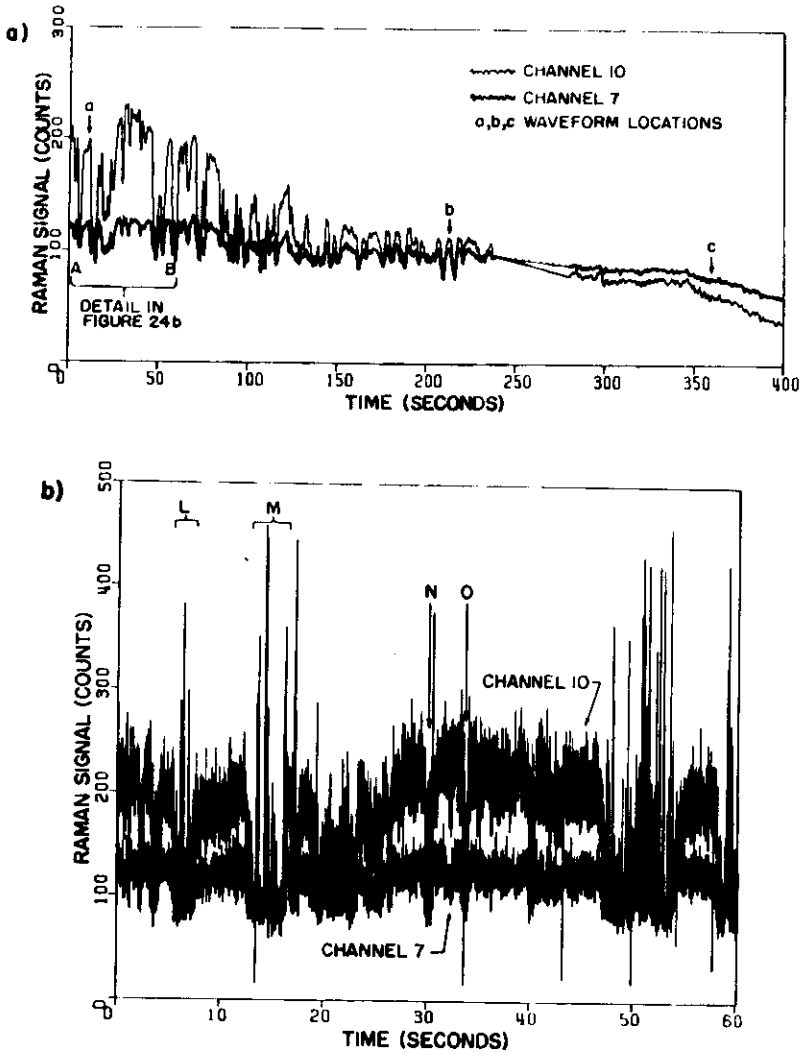

Figure 6.24. (*a*) Profile of channels 7 and 10 from airborne depth-resolved water Raman backscatter waveforms corresponding, respectively, to measurements made at depths of 1.8 and 2.5 m. Arrows show locations of depth-resolved waveforms of Figure 6.6. Data gap indicated by straight lines connecting profiles between 240 and 280 s (Hoge and Swift, 1983c). (*b*) Detailed plot of initial flight line portion labeled *A–B* in Figure 6.24. Presence of numerous clear water cells of various sizes readily apparent. Samples of sharp declines in water Raman backscatter can be found at positions *L*, *M*, *N*, and *O* (Hoge and Swift, 1983c).

nels from the 381-nm Raman backscatter waveform (channels 7 and 10 from Figure 6.6 of Section 6.2.1.4). Figure 6.24*a* vividly shows the gross cell structure in the coastal waters off the Virginia coast during a 40-km westward flight from clearer water to the more turbid surf water near the beach. Figure 6.24*b* shows the detailed cell structure observed in the clearer water portions of the flight line. The waveform shape is modeled rather well, as discussed in Section 6.2.1.4 and in Figure 6.7.

The water column or depth-integrated fluorescence and Raman signals may also be used in broader scale field experiments to map the location and relative strength of fronts (Hoge and Swift, 1982b). During the 1979 Maritime Remote Sensing Experiment (MARSEN) the AOL participated in seven flights in the North Sea. Several of these missions were used to map the German Bight where the Elbe River and Weser River deposit large quantities of fresh water laden with dissolved and particulate materials. The naturally occurring *Gelbstoff* or dissolved organic material was assumed to be a conservative tracer during the 3-h time period of the mapping exercise. The AOL instrumentation was configured as listed in Table 6.1. Figures 6.25*a*,*b* show the water Raman and unnormalized *Gelbstoff* fluorescence from a typical flight line. Notice, for the most part, that changes in the Raman profile are mirrored in the *Gelbstoff* profile. Although the sense of movement is generally the same in both profile traces, the degree of the corresponding movement is quite variable. This can be seen by comparing the segments designated 1, 2, 3, 4, and 5 in Figure 6.25. Normalization of the fluorescence signal with the Raman backscatter signal significantly reduces the effect of the changes in water optical transmission upon the final, corrected fluorescence signal. (Normalization is also discussed in Section 6.2.2.1.) Figure 6.25*c* shows the profile of the normalized *Gelbstoff* fluorescence. Notice that the amplitude remains relatively smooth over most of the flight line except at the points labeled 1–5. Both (a) the relative strength or localized slopes within the normalized *Gelbstoff* profile (in counts/km) and (b) the sign of slope were then used to delineate the fronts. Front location maps were generated from these slope/sign variations. It was determined that the spatial distribution of the fronts found by this airborne lidar technique was in very reasonable agreement with previously published oceanographic ship results.

Mesoscale eddy or warm core ring mapping by airborne lasers was discussed in Section 6.2.2.1. Essentially the same 532-nm laser and AOL configuration were used during the Superflux experiments (Campbell and Thomas, 1981) to map chlorophyll and phycoerythrin fluorescence as well as Raman backscatter (Hoge and Swift, 1981c). Sarabun (1981) used the AOL multichannel fluorosensing lidar data in a cluster analysis to define water mass boundaries and/or water types. He was able to show that the data allowed the generation of maps having physically plausible water mass delineations.

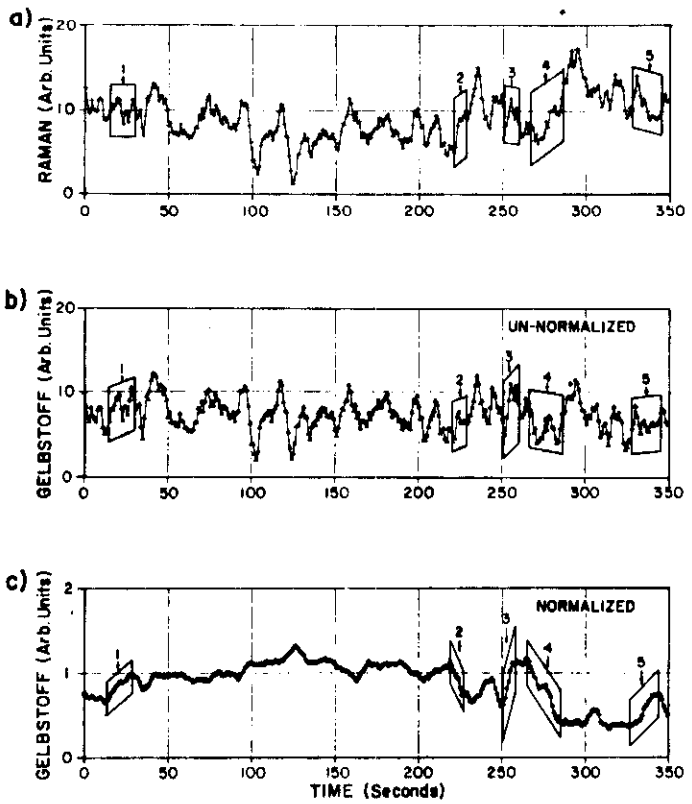

Figure 6.25. Profiles of (*a*) depth-integrated water Raman backscatter and (*b*) *Gelbstoff* fluorescence obtained in German Bight region of North Sea. (*c*) *Gelbstoff* fluorescence normalized by water Raman backscatter from (*a*). Normalization of *Gelbstoff* fluorescence with Raman backscatter significantly reduces effect of water optical transmission and allows easier identification of fronts whose locations can be found, e.g., at 1, 2, 3, etc. (Hoge and Swift, 1982b).

6.2.2.4 Optical Properties of Ocean Water Column

The world's oceans cover almost 75% of Earth's surface and are responsible for an estimated 30–45% of all primary production (Strumm and Morgan, 1981; Riley and Chester, 1971). It is a significant challenge to measure and monitor this vast and important surface area. Furthermore, it is an even bigger challenge to measure the upper layer and/or volume beneath this surface. Presently, measurements in the volume are being accomplished for the most part by airborne

and satellite passive remote sensing. However, better physical, chemical, and biological measurements in the volume strongly depend on the models used to invert the data. Accordingly, these models can probably be improved by inclusion of accurate measurements of the optical properties of the water column by airborne lidars. Furthermore, a potentially important and concurrently related application of airborne oceanic lidars is the validation and/or calibration of passive, optical satellite measurements in a region of the ocean chosen to be generally representative of vast areas of the globe. Then, the lidar-calibrated satellite sensor can be used outside and beyond the validation area to obtain improved data to allow, for example, better global productivity estimates. Of course, even in the absence of passive ocean sensor requirements for lidar optical properties and validation/calibration data, airborne lidar measurements of the upper ocean are important in their own right since large areas of the ocean can be surveyed rapidly, even under cover of darkness if necessary.

As we have seen, the accuracy of biological, chemical, and physical water column measurements by lidar is strongly driven by the optical properties of the water column. The volumetrically derived water Raman backscatter has of course been used to significant advantage to correct for the attenuation properties of the water column. Beyond this, however, the quantitative measurement of the inherent optical properties of the ocean by remote sensing is difficult and still requires some in situ measurements.

As pointed out earlier in this chapter, Gordon (1982) investigated the effects of multiple scattering on the interpretation of oceanic lidar data. Using Monte Carlo techniques to solve the radiative transfer equation, he found that, after removal of geometric loss factors, the on-wavelength or elastic backscattered power is a decaying exponential function of time over the time interval required for photons to travel four attenuation lengths through the water. The effective attenuation coefficient of the exponential decay was found to be dependent on the ratio of the radius of the spot on the sea surface viewed by the lidar to the mean free path of the photons in water. When this parameter is nearly zero, the exponential decay is determined by the beam attenuation coefficient, whereas for values greater than about 6, the exponential decay asymptotically approaches, or is given by, the attenuation coefficient for downwelling irradiance (diffuse attenuation coefficient). For intermediate values of the parameter the interpretation of the effective attenuation coefficient apparently requires complete knowledge of the inherent optical properties of the water: the beam attenuation coefficient and the volume scattering function. Gordon's results were essentially corroborated in the Monte Carlo modeling of water Raman normalization by Poole and Esaias (1982).

Independently, Koerber and Phillips (1982) used Monte Carlo techniques to determine that accurate estimates of the absorption coefficient a can be obtained from measurements of the decay rate of the lidar backscatter envelope provided

that an adequately large FOV is used. The technique uses an airborne lidar system to transmit a laser pulse vertically downward into the water column and subsequently records the temporal, on-wavelength or elastic backscattered signal. They also concluded that the backscatter signal can be used to estimate the scattering properties of seawater, for example, the volume scattering function at 180°, $\beta(\pi)$. However, this $\beta(\pi)$ must be converted to values of the scattering coefficient b by using a nonlinear empirical relationship that in turn depends on the in situ measured volume scattering functions of Petzold (1972). The obvious weakness of this method lies in the fact that the empirical relationship derived for a particular region may not be valid in all water masses. This, then, is roughly equivalent to the suggestion by Gordon (1982) that for intermediate values of the ratio of the lidar-viewed spot radius to the photon mean free path, a complete knowledge of the inherent optical properties is required.

Subsequently, Phillips et al. (1984) described an analytical technique for the independent measurement of two basic, intrinsic optical properties of seawater: the absorption and scattering coefficients. The technique relied on the previous Monte Carlo simulations that provided the necessary data to establish the feasibility of an airborne laser technique (Koerber and Phillips, 1982) and an earlier theoretical study (Phillips and Koerber, 1984) that utilized the Monte Carlo results to establish the limits of validity of the analytic model. Using a full Monte Carlo simulation (as opposed to semianalytic Monte Carlo techniques), Phillips et al. (1984) showed that in the asymptotic limit of large FOV (and corresponding sea surface spot diameter) the effective attenuation coefficient γ is the absorption coefficient a rather than the diffuse attenuation as found by Gordon (1982). They argue the finding that $\gamma \rightarrow a$ in the large-FOV limit becomes evident when the independent variable in the model is considered to be time rather than depth. Then, every photon received at a given time has obviously spent the same amount of time in the water and has also traveled the same total distance in the water, irrespective of how many times it has been scattered. Since the only process reducing the number of such photons is absorption, the effective attenuation coefficient equals the absorption coefficient. Phillips et al. (1984) further conclude that, apart from geometric factors, the amplitude of the backscatter signal at the water surface and its time decay in the water column allow both the absorption and scattering coefficients of water to be determined independently. In situ measurements were used to confirm the validity of the technique. Clearly, however, more modeling and field measurements were recommended to resolve the findings of Phillips et al. (1984) relative to those of Gordon (1982) and Poole and Esaias (1982).

In spite of efforts thus far it seems that (1) assumptions about the water mass being overflown must be invoked or, (2) as Gordon (1982) suggests, the complete knowledge of the inherent optical properties (beam attenuation coefficient and volume scattering function) of the water must be known if the ratio of the observed ocean spot to photon mean free path is from ~0.5 to 5 or 6.

6.2.3 Effect of Surface Waves on Measurements in Ocean Volume

To this point we have considered lidar measurements of the sea surface and materials deployed upon it (Section 6.2.1). Also, the measurement of constituents within the ocean volume has been discussed separately (Section 6.2.2). However, there is strong experimental evidence that variability in sea surface elevation modulates signals obtained from within the water column. The height and slope statistical distributions of the sea surface waves are known to significantly affect the in-water, spatial or volumetric distribution of an incident laser beam upon its initial, vertically downward passage through the surface (Bobb et al., 1978). Wave slope statistics have actually been obtained from optical radiance measurements made below the sea surface using the sun as the light source (Stotts and Karp, 1982). Furthermore, lasers immersed in the ocean have been used to measure wave slopes by directing the beam vertically upward into a four-quadrant detector (Schau, 1978; Tang, 1981; Tang and Shemdin, 1983). Thus, by induction, the uncollimated, spherically isotropic fluorescence and Raman backscatter from the water column must be spatially redistributed into the observational hemisphere above the sea surface. Clearly, then, there would be some manifestation of the distributed sea surface embedded within the volumetrically generated return signals. The sea surface perturbation of water-column-derived lidar backscatter signals was first reported by Hoge and Swift (1983a). This relationship is illustrated in Figure 6.26*a*, which shows profiles of the depth-integrated Raman signal and the sea surface elevation, both plotted as a function of time for an expanded segment of pass 2 over the LaRosa slick previously discussed in Section 6.2.1.4. The sea surface elevation was determined by subtracting the mean slant range measurement acquired by the lidar altimeter subsystem from individual slant range measurements and inverting the results such that the peaks represent wave crests and conversely the depressions represent wave troughs. [Low-frequency vertical aircraft motion (Krabill and Martin, 1983; Hoge et al., 1984) has not been removed from the data; however, this motion is of no consequence in the following discussion.] The correspondence (outside the oil slicks themselves) of higher Raman signal to wave crests and lower Raman signal to wave troughs persisted throughout the oil spill data sets. This correspondence or correlation also exists in depth-resolved water Raman backscatter signals, as seen in Figure 6.26*b*. Note particularly the apparent phase shift between the Raman signal peak and the wave crests. While there are a few exceptions, variations in Raman backscatter signal from the ocean volume appear to lag corresponding variations in the sea surface record. This

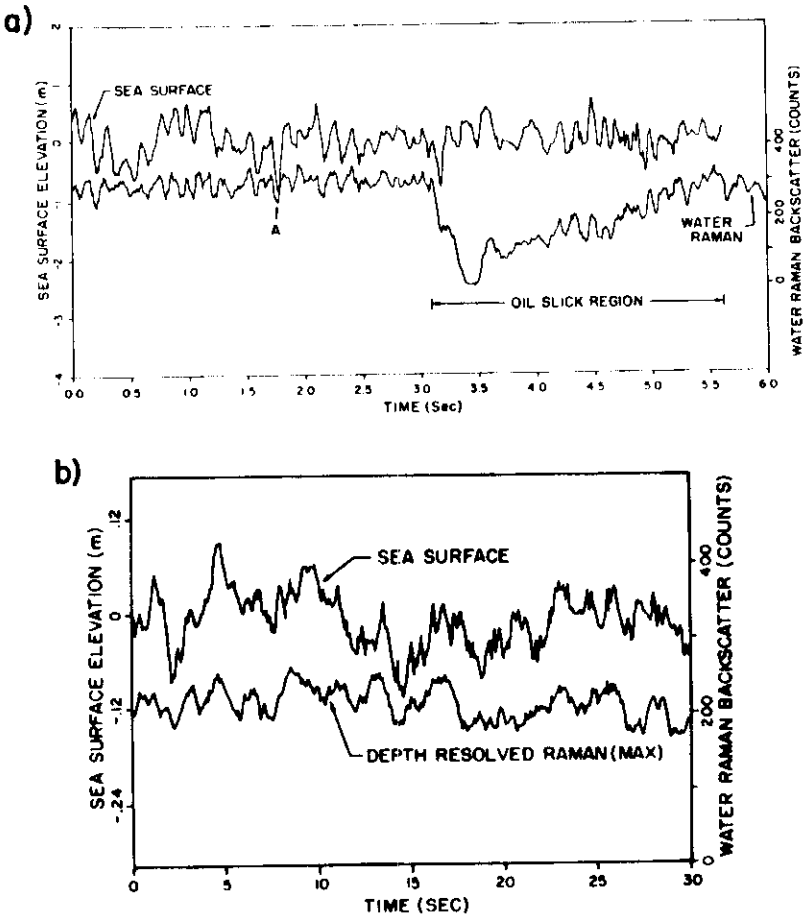

Figure 6.26. (*a*) High correlation of depth-integrated water Raman backscatter with sea surface elevation. Correlation persists over all but thickest portion of oil slick. Spatial phase lag between two measurements is particularly recognizable at position *A*. (*b*) Correlation of depth-resolved water Raman backscatter with sea surface elevation. Sea surface derived from range data obtained from leading edge of depth-resolved water Raman return pulse (Hoge and Swift, 1983a).

is quite evident in Figure 6.26*a* at the position labeled *A*, where the local Raman depression lags the wave trough. This apparent phase shift is caused by the off-nadir pointing angle of the lidar system relative to mean sea level (Hoge et al., 1984). It should also be noted that the detection of the ocean surface is dominated by Fresnel reflection with some Mie backscatter components from the ocean volume while the Raman backscattered signal is strictly volumetric.

The relationship between the sea surface wave structure and the resulting modulation of volumetrically derived fluorescence and Raman backscatter is not well understood and is not easily modeled in closed form. Gelhaar (1982) was the first to show by computer simulation and some limited closed-form analysis that lidar fluorescence signals from the volume are modulated by the sea surface. Gehlaar (1982) developed a three-dimensional computer simulation based on ray-tracing principles. He used this model to analyze the effect of sea surface structure, or elevation, on lidar fluorescence signals generated within the ocean volume. He found that the depth-resolved fluorescence return signals possessed a maximum that was positioned several meters below the surface. This signal maximum is attributed to allowable refractory exit channels leading to the detector. If one assumes that a monochromatic sine wave corrugation makes up the sea surface, the depth of the signal maximum can be calculated exactly and is found to be in good agreement with the computer model results. Gehlaar (1982) further validated the computer simulation model by calculations based on (1) the transformation of solid angles by the curved boundaries on the surface and (2) statistical methods. Generally, it was found throughout the calculations that the signal maxima found just below the surface is followed by a signal reduction or fall-off with depth that is steeper than would be attributed to the usual $\gamma_e + \gamma_f$ effective attenuation coefficient losses. His work is a good first-start effort and points to the need for adequate experimental verification and further modeling.

In Section 6.2.1.5 manmade monomolecular slicks on the ocean surface were discussed in the context of their use in the calibration of petroleum oil slick measurements. In truth, since these monomolecular slicks are, for all practical purposes, nonfluorescent and nonattenuating, they should be considered useful in the study of fluorescence/Raman signal modulation by surface waves. Huhnerfuss et al. (1985) have experimentally shown that airborne lidar fluorescence and Raman signals are significantly modified by monomolecular films. They suggest that one of the possible reasons for the observed lidar signal depressions is the alteration of the spatial distribution of the volumetrically derived backscatter signals by the monomolecular film. Figure 6.27*a* (upper) illustrates qualitatively that (because of wave damping) the monomolecular slick region has a wave slope distribution whose variance or width is smaller than found for the clean sea region. Thus, the volumetrically derived backscatter signals detected while overflying a monomolecular film will have a more sharply peaked spatial distribution in the upward or vertical direction normal to the mean sea surface (Figure 6.27*a*, lower). For the nonslick or clean sea, the wave slope distribution and corresponding lidar backscattered signal spatial distribution are given in Figures 6.27*b* (upper) and 6.27*b* (lower) respectively.

Then, if one is lidar-sensing the water column beneath the film, very near to the nadir direction, the backscattered signals would actually be enhanced relative to those found in the clean, non-film-covered sea nearby. However, if the

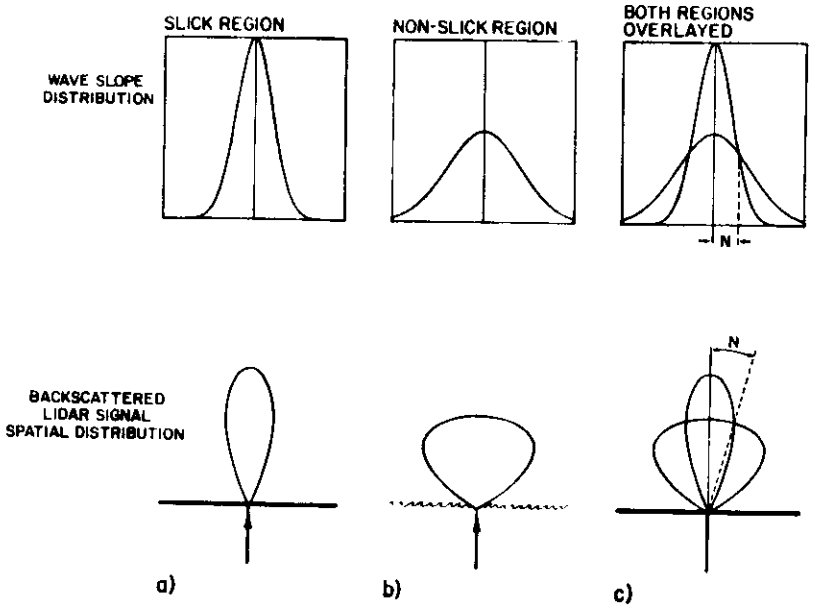

Figure 6.27. Wave slope distribution and backscatter lidar signal spatial distribution expected for (*a*) monomolecular slick and (*b*) nonslick region of ocean. (*c*) Overlay of respective distributions in (*a*) and (*b*) illustrating lidar observational angle at which slick could not be distinguished from open ocean.

airborne system is viewing the film-covered sea at a sufficiently large off-nadir angle relative to the vertical, the lidar signals while over the slick will be reduced (relative to the clean-sea region). This is illustrated in Figure 6.27*c*, where both the wave slope (and lidar backscatter spatial) distributions for slick and nonslick regions have been overlayed. A larger lidar backscatter signal is obtained while over the nonslick region if the observing angle is as depicted in distribution overlays of Figure 6.27*c*. The observations at large off-nadir angles ($>N$) are essentially being made in the higher power peripheral portion of the broadly peaked spatial distribution of the upwelling radiant flux in the nonslick region. Figure 6.27*c* further shows that the slick and nonslick regions cannot be easily discriminated on the basis of backscattered power if the lidar off-nadir observing angle is equal to N, as shown. The angle N would probably not be known a priori but could be measured with a scanning lidar by determining the angle at which the slick and nonslick backscattered signal strengths are equal. In Figure 6.11, discussed in Section 6.2.15, the AOL fluorescence and Raman

backscatter data were obtained at an off-nadir angle of ~7°, resulting in signal depressions while over the monofilm.

In this qualitative explanation we have avoided discussing the fact that the narrow transmitted laser beam spatial distribution incident on the sea surface is also altered at the air–sea interface. However, based on recent studies it appears that the in-water, volumetric spatial redistribution of the incident laser beam upon its downward passage through the surface (Bobb et al., 1978) [and subsequent multiple scattering within the ocean volume (Lerner and Summers, 1982)] is small (and potentially ignorable) compared to the spherically isotropic spatial distribution of the fluorescence and Raman scatter that this incident beam generates.

Karp (1976) theoretically studied the transmission of a laser beam from above (as well as from below) the sea surface for down-link (and up-link) satellite optical communications feasibility studies. His work (and included references) and that of Bobb et al. (1978) could serve, in addition to Gehlaar's (1982) work as the research base from which monostatic airborne lidar sea surface modulation modeling studies could be initiated. The theoretical work of Luchinin (1979) and Luchinin and Sergiyevskaya (1982) should also be evaluated to determine if redistribution of the surface incident laser beam by surface waves could be described as a special case of their solar ray formalism. While there is strong experimental evidence for sea surface perturbation of volumetrically derived lidar signals, the degree of influence on the signal spatial distribution by Mie scattering within the medium should also be evaluated, quantitatively if possible. In this regard, the theoretical descriptions of the propagation and interaction of narrow light beams in seawater (Yura, 1973; Arnush, 1972; Makarevich et al., 1969; Romanova, 1968; Bravo-Zhivotovskiy et al., 1969) should also be evaluated.

6.2.4 Bathymetry and Other Water Column and Ocean Bottom Measurements

As discussed previously, Hickman and Hogg (1969) first demonstrated that an airborne laser system could be used to measure water depth. They showed that a single pulse, when transmitted vertically downward to the water's surface, is in turn partially reflected from that surface as well as the water–bottom interface. Thus, there is generated a pair of pulses whose separation is proportional to the water depth. The low-power 60-μJ neon laser pulse that they used was adequate to map depths to nearly 8 m from an airborne platform flown 150 m above the water's surface. Kim et al. (1975) and Kim (1977) used a 2-kW, 6-ns pulsed neon laser at 540 nm and a 2-MW, 8-ns, frequency-doubled Nd-YAG laser at 532 nm to obtain bathymetric profiles in the Chesapeake Bay and

Key West, Florida, regions. Depths to almost 10 m were obtained in waters having an effective attenuation coefficient of 0.175 m^{-1}. His work has been adequately reviewed by Measures (1984).

By far, the principal hinderance to the useful, routine application of airborne coastal bathymetry is the two-way exponential water column attenuation of the transmitted pulse and the reflected pulse from the bottom. Accordingly, one must virtually scale the laser power upward by an order of magnitude in order to achieve operation to twice the depth. Thus, with the inefficiency of lasers, one must carefully choose the season in order to avoid attenuation by plankton growth and further avoid months when winds will stir and entrain bottom sediments into the water column (Hoge et al., 1980). Finally, one must choose sites whose bottom can actually be reached by laser sounding. Some of the practical considerations for using an airborne laser system for routine survey have been reported by Enabnit et al. (1981). Furthermore, to be truly cost-effective in a high-density mapping mode, the laser bathymetry system must be able to scan the beam over a substantial swath. This requires a high-repetition-rate laser transmitter, receiver, and recording components. The principal cost factors have been studied by Enabnit et al. (1978), who reported that airborne laser hydrography was cost-effective relative to standard launch or ship techniques.

Hoge et al. (1980) demonstrated that conical scan methods were feasible for airborne laser hydrography. They used a 400-Hz, 7-ns neon laser having a 3-kW output at 540.1 nm to map portions of the Chesapeake Bay and the adjoining Atlantic Ocean. Depths to 10 m in the ocean and 4.6 m in the bay were measured. Water truth measurements were taken to validate the depth and beam attenuation coefficient, which allowed evaluation of the system's performance. Lidar bathymetry in the United States is presently being pursued on an active basis by the U.S. Navy. A modest effort continues to show good progress on their Hydrographic Airborne Laser Sounder (HALS). This 400-Hz, frequency-doubled Nd–YAG conical scan system is electronically configured to process analog bathymetry waveforms in real time and record the resulting depth. The system contains a time-gated or variable-gain PMT to reduce the strong surface return and enhance weak bottom returns. This PMT is subsequently followed by a logarithmic amplifier to further accommodate the wide dynamic range between the surface and bottom return signal strengths.

Interest in laser hydrography is not limited to the United States. The Australian coastal waters are so extensive that a laser hydrography program was begun there as an outgrowth of their airborne laser land profiler effort (Clegg and Penny, 1977). Their first bathymetric profiling tests in 1975 yielded 30–40-m depths using a 532-nm-wavelength laser. Another system (called WRELADS II) has full scanning capability, horizontal position fixing, and data-recording capabilities and is undergoing flight trials (Penny, 1982).

In Canada four different airborne techniques were evaluated for their coastal hydrography needs. Only lidar bathymetry was demonstrated to achieve the depth accuracy required by the Canadian Hydrographic Service Charting Standard (O'Neil, 1983).

Scientists with the Swedish government recently reported laser bathymetry efforts in the Baltic Sea (Steinvall et al., 1981). They used the Canadian lidar bathymeter (MK-II) to show that depths of 30 m could be mapped. The MK-II lidar delivered 5-MW pulses with 5-ns lengths and was flown at an altitude of 150 m.

In bathymetrically related efforts, researchers in Sweden had previously reported underwater laser–radar laboratory experiments in the areas of bathymetry and fish school detection (Fredriksson et al., 1979). The experiments were performed in a 27-m horizontal tank that had been fitted with mirrors to control beam direction. In these experiments, a nitrogen-laser-pumped dye laser was used to produce a 5-ns pulse in the green spectral region. The backscatter was collected by a receiver consisting of a Newtonian telescope, a PMT, a fast transient digitizer, and an on-line computer. Useful laser–radar echoes could be detected from the dark backs of herrings, sprats, and mackerels at "depths" to 15 m. Subsequently, some live fish were gently held a few centimeters underwater in small collars while the 337.1- and 532-nm laser-induced fluorescence was measured. Fluorescence was observed from both the backs and undersides of the fish with the latter signals being strongest. Unfortunately, the fluorescence (a) was quite weak and (b) had the same shape as the spectrum of naturally occurring DOC. They concluded that the strength was insufficient to be of practical use. Much earlier, laboratory and theoretical studies of fish school detection by airborne laser systems had been conducted in the United States (Murphee et al., 1973). They concluded that fish detection (using the on-wavelength backscatter signal) was feasible from a low-flying (150 m) aircraft using equipment available at that time.

In closing this section it should be mentioned that the operation in shallow water of a depth-integrating fluorescence lidar has not yet been reported. However, upon encountering shallow water, the received fluorescence signals are expected to increase for several reasons. First, the isotropically emitted fluorescence (stimulated at every depth location during downward propagation of the on-wavelength beam) will be reflected from the bottom to provide some increase in the backscattered signal. Second, there will be additional stimulation of the water column (and its constituents) by the on-wavelength radiation after reflection from the bottom. Thus, the on-wavelength reflection from the bottom effectively increases the apparent depth of the water column being sensed. Since the original transmitted beam remains spatially more compact (Lerner and Summers, 1982) than the isotropically emitted fluorescence it produced during vertical, downward traversal, the bottom reflection of this induced fluorescence is

expected to be smaller than that produced by the vertically propagating on-wavelength reflection. Furthermore, the on-wavelength radiation is expected to dominate the bottom effects since it is reflected in a Lambertian manner from the bottom. This, in turn, improves its effectiveness in stimulation of the water column during its upward propagation. Note further that some of the fluorescence produced by the vertically propagating on-wavelength reflection also is ultimately reflected from the bottom. Finally, if the bottom contains fluorescent materials and/or vegetation, this fluorescence adds to that of the water column constituents. Of course, if one is observing the on-wavelength bottom return, the fluorosensor aperture gate can be manually or automatically adjusted in width and depth position to reject all bottom reflections.

6.3 TERRESTRIAL LIDAR MEASUREMENTS

6.3.1 Terrain and Vegetation Elevation Measurements

Fundamentally, terrain profiling is the simplest and perhaps the oldest application of an airborne laser (Jensen, 1967). Since the late 1960s and early 1970s, airborne lasers have been used for the metric measurement of terrain and ice surfaces. Noble et al. (1969) reported the airborne measurement of ice elevation with a commerically available modulated CW 632.8-nm helium–neon laser profiling system. This low-beam divergence lidar system was flown over ice in the Beaufort Sea to demonstrate the feasibility of using a laser system to accurately profile the sea ice surface and to measure the pressure ridge heights. The laser-derived sea ice surface profile clearly allowed the delineation of water, thin ice (first-year ice), and pack ice (multiyear ice). They found that for a small-spot-size nadir-pointed lidar such as this, the height variance (as well as the backscattered signal strength) of the elevation profile data is higher over water than thin ice, and in turn, the thin-ice elevation variance (and associated backscatter signal strength) was higher than that of pack ice. Using essentially the same lidar, Ketchem (1971) and Tooma et al. (1976) obtained profiles of first-year and multiyear ice.

For land terrain profiling Penny (1972) used a doubled Nd-YAG laser with a 20-ns pulse width, an energy of 750 μJ/pulse, and a beam divergence of 0.3 mrad as the transmitter. The 10-cm receiver telescope and PMT detector/amplifier allowed operation to 5000 m above ground level. The laser system determined a profile of terrain heights above a reference surface that was 6000 m below an isobaric surface at the nominal aircraft altitude. The barometric height above the isobaric surface was measured by a sensitive differential pressure gauge. The horizontal position of the aircraft was determined through interpretation of photographs obtained during the laser profiling. Their system was not fully evaluated for mapping through tree-covered terrain, and no field trials were conducted over dense jungle terrain.

Mamon et al. (1978) reported the test flight results of a compact transceiver that was built by a commercial manufacturer. The transmitter used a GaAs solid-state laser, 15-cm-diameter collimating objective yielding a 1.5-mrad FOV. The laser pulse width was 10 ns and yielded a peak power of 25 W per pulse. The receiver consisted of a 20-cm-diameter collimating lens and an avalanche photodiode detector. Their system was designed for terrain elevation profile measurements even in the presence of trees. Since branches may give multiple target return signals, one or more return pulses might be received in response to one transmitted pulse. Thus, since the range to the ground is required, the last pulse from a series of multiple returns must be discriminated. Their system incorporated this so-called last-pulse selection. Data were taken over a deciduous forest at two different seasons of the year, yielding measurements during full-foliage and no-foliage conditions. From this standpoint alone, the GaAs lidar represented a slight improvement over the Australian system. However, no method was provided for removing the aircraft vertical motion as had the Australian system. As with the Australian system, the horizontal position control was provided by photographic data.

Krabill et al. (1980, 1984) presented the results of a series of joint NASA–U.S. Army (Corps of Engineers) terrain mapping experiments. They used the NASA AOL in the bathymetric mode with a laser repetition rate of 200 pps to obtain both profile and scan data over open and tree-covered terrain. The experiments were conducted to collect data similar to that a ground survey team would normally obtain for input to hydraulic-hydrologic models for simulating flow lines of streams. Both existing ground survey and independently obtained photogrammetry were used for ground truth. Figure 6.28 shows a comparison of the airborne laser data and a photogrammetrically derived profile. Notice that a 12-cm rms difference was obtained over terrain with no trees or bushes while a 50-cm rms difference was obtained over wooded terrain. No attempt was made to verify the accuracy of either the lidar or photogrammetric results. Some of the difference may have been due to errors in the photogrammetric profile. In fact, in at least one instance, the laser found verifiable terrain features that were completely missing in the final photogrammetry truth products. Note further in Figure 6.28 that the heights of the trees may be obtained quite easily. [Such vegetation features can also be found in the data of Penny (1972) and Mamon et al. (1978).] In lieu of a last-pulse tracker, the bathymetric mode of the AOL (Hoge et al., 1980) was used to advantage to find the forest floor terrain segments. Here, the depth-resolved or temporal-waveform-recording subsystem is used to obtain a "surface" return from the top of the forest canopy and the bottom return from the forest floor. Then the sum of the range to the "surface" (canopy) and the "depth" (tree height) yields the slant range from the aircraft

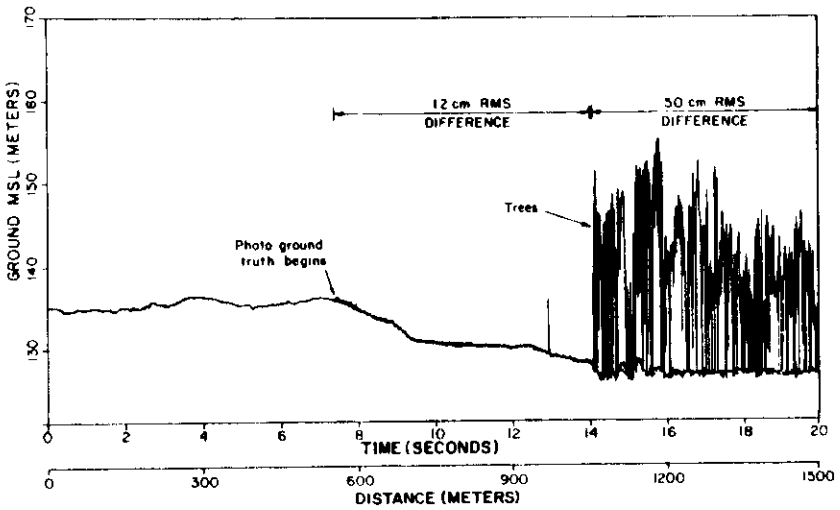

Figure 6.28. Comparison of airborne laser terrain survey and photogrammetrically derived profile. Bathymetric mode of AOL used to locate forest floor terrain segment (Krabill et al., 1980).

to the ground. Aircraft horizontal position for these tests was determined from a combination of inertial navigation system (INS) position, velocity, heading, track angle data, and photographic interpretation. The aircraft vertical position was determined from three (minimum) ground survey points, AOL range data, and a vertical accelerometer.

The lengths to which one must go to determine the aircraft position (and orientation) points to the fact that both navigation and positioning remain as problems for generalized application of an airborne lidar to terrain mapping and tree height measurement (Chapman, 1982). Vertical control can be satisfactorily accomplished over flight lines of several kilometers using an inexpensive vertical accelerometer along with several vertical reference points on each survey line. One can look with anticipation to the global positioning system (GPS) to fill the future positioning needs for these and similar airborne mapping applications.

With the AOL operating in the scan mode (Link et al., 1983a,b) it was shown that a three-dimensional terrain contour map could be obtained through forested areas. Figure 6.29*a* shows a composite of two separate passes of the AOL over the same forested ("leaves-off") target region. Again, the bathymetric mode of the AOL was used with a laser rate of 200 pulses/s. The laser data have been smoothed to remove the high-frequency contributions and thus

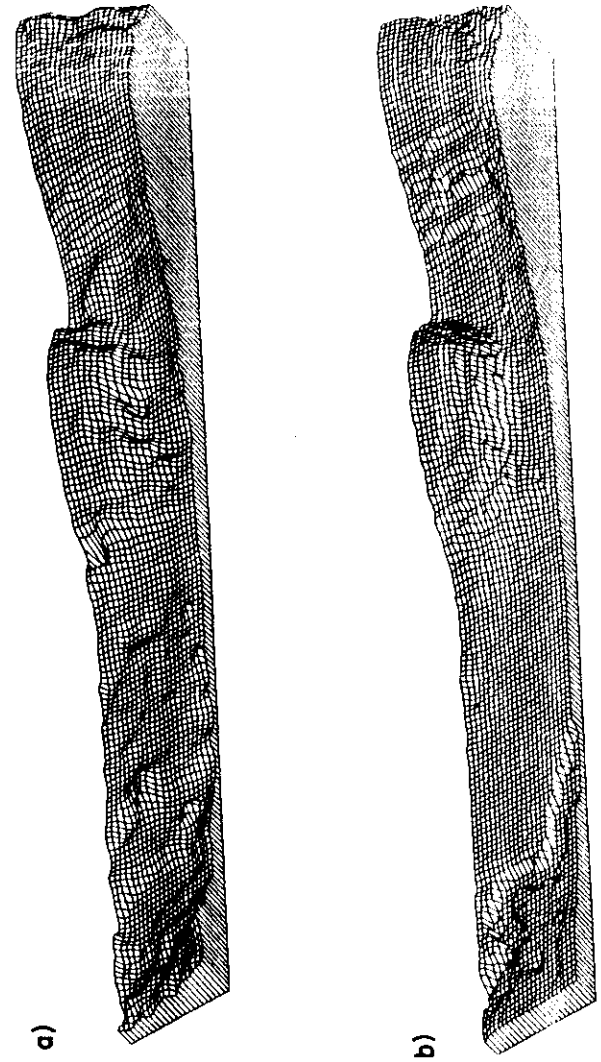

Figure 6.29. (*a*) Topography map of forested region composed of two passes of AOL (smoothed). Bathymetric mode of instrument used with 200-pps laser rate. (*b*) Photogrammetric truth map of same region as in (*a*) (Link et al., 1983a).

simplify comparison with the photogrammetry truth data (Figure 6.29*b*). An independent point-by-point comparison showed that almost 80% of the laser data were within 1 m of the photogrammetric data.

In summary, Krabill et al. (1980, 1984) showed that laser mapping of river valley cross sections in deciduous forest areas appears to be primarily restricted to winter foliage conditions to meet accuracy requirements. However, in areas covered predominantly by coniferous forests, useful ground surface elevations may be acquired at any time of the year. The use of an inexpensive accelerometer to effect vertical control over the distance of a normal flight line is an important advance in vertical position control (Krabill and Martin, 1983). This technique is now being used extensively in making airborne oceanographic laser (Hoge et al., 1984) and radar (Walsh et al., 1984) measurements.

Nelson et al. (1984) used a pulsed nitrogen laser in the AOL system (Hoge et al., 1980; Krabill et al., 1980) to determine the alteration of forest canopy characteristics as a result of insect infestation. Again, the bathymetric mode of the AOL instrument was used to obtain tree heights. They found that (a) the amount of healthy crown sensed over a flight line interval is most closely related to the number of transmitted laser pulses that hit the tree canopy but in which a ground return signal could not be found in the temporal waveform, (b) a comparison of laser profiles taken over healthy and over defoliated (by gypsy moth infestation) forest segments suggested that pulse penetration into the defoliated canopy is greater than the intrusion into a healthy canopy, (c) cross-sectional area (the canopy profile) increases as canopy density increases (this is apparently because denser canopies intercept the laser pulse higher in the canopy, hence yielding a cross-sectional area that is directly related to canopy closure), and (d) the numbers of ground returns increased significantly in defoliated canopies.

One of the most important practical uses of tree height information is the potential it has for yielding timber volume estimates. The relationship between canopy profile and timber volume is based on stratification of species (Maclean, 1982), and thus to obtain reliable estimates of volume, the tree species must be identified. Airborne tree species identification (simultaneously with tree height and canopy closure information) would perhaps allow high-speed timber volume estimates to be obtained. One possible technique that merits investigation is the use of laser-induced fluorescence of the tree's foliage at the same time as the metric height and canopy data are being obtained. Airborne lidars such as the AOL have the potential to gather the required LIF and metric data simultaneously. However, significant laboratory work must be accomplished before this technique can be expected to yield fruitful airborne results. Some of the most recent LIF of terrestrial plants are described in the next section.

6.3.2 Laser-Induced Fluorescence of Living Terrestrial Plants

Clearly, species identification is important insofar as it would allow the practical airborne measurement of timber volume and assessment of biomass. Species identification of all growing plants is also important particularly for foodcrop (and noxious weed infiltration) inventory reporting on a local, national, and international basis. Furthermore, the ability to discriminate among different varieties of the same species would allow regional identification of more naturally disease-resistant strains of different cultivated foodcrops. In total, the ability to identify (a) species, (b) varieties of the same species, (c) maturity within a variety or species, and (d) the previsual and contemporary stress upon the species would have far-reaching, economic and human resources development implications throughout the world. It is felt by many scientists that the multispectral, high-resolution capability of laser-induced fluorescence has enormous potential to address plant identification, maturity, and stress. This is especially evident when such laser techniques could be combined with existing satellite passive multispectral data that is now so easily obtained.

Apparently, the first reported utilization of laser-induced fluorescence in the study of intact plants was performed in Canada. Brach et al. (1977) used remote sensing laser spectroscopy techniques in a laboratory-greenhouse configuration. A pulsed nitrogen (337-nm) and a CW helium–cadmium laser (441 nm) were used to investigate the potential for recognition of both lettuce maturity and variety. While the techniques showed promise, no conclusions regarding their ultimate application were made. Subsequent LIF experiments by Brach et al. (1978) showed that the fluorescence induced by 410-nm laser excitation of a lettuce or grass crop increased as the lettuce or grass matured. However, the same experiments indicated that the laser fluorescence technique would not easily discriminate between different varieties of lettuce cultivars. Later experiments on grain crops (Brach et al., 1982) showed that the fluorescence quantum yield (and possibly the structure of the fluorescence spectra) could be used to differentiate between species and cultivars of a species. Additionally, these authors noted that it appeared likely that the pigment composition determines the fluorescence yield and the structure of the fluorescence spectral curve.

Chapelle et al. (1984a) used a 337-nm laser spectrofluorometer in laboratory studies to show that LIF measurements of plants offer potential for remotely detecting certain types of stress conditions and also for differentiating plant species. The 337.1-nm LIF spectrum of soybeans is shown in Figure 6.30. Typically, spectral peaks are found at 440, 525, 690, and 740 nm. Withholding water from the experimental plants caused dehydration and wilting and resulted in a general increase in fluorescence, as shown. Specifically, the increase in the

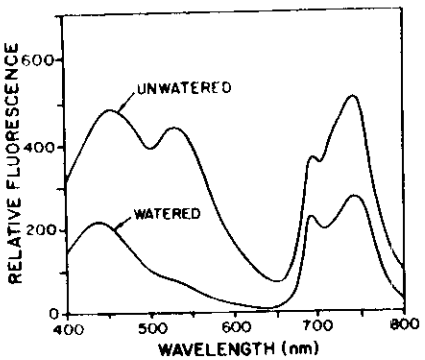

Figure 6.30. A 337.1-nm laser-induced fluorescence emission obtained in laboratory from soybean leaves. Most pronounced effect of dehydration is enhancement of 540-nm band (Chappelle et al., 1984a).

525-nm peak is most dramatic. A potassium-deficiency condition was found to result in a significant increase in the 690- and 740-nm spectral peaks of corn LIF spectra. Incubation of soybean leaves in 3-(3,4-dichlorophenyl)-1,1-dimethylurea (DCMU) led to a suppression of the 690- and 740-nm spectral peaks. Chapelle et al. (1984a) concluded that an impairment of the photosynthetic process leads to an increase in fluorescence at 690 and 740 nm, but a decrease in chlorophyll concentration such as by senescence leads to a decrease in 690- and 740-nm fluorescence with a corresponding increase in 440- and 525-nm fluorescence. The 690- and 740-nm bands are attributed to two different species of chlorophyll (Brown and Michel-Wolwertz, 1968). The spectral peaks at 440 and 525 nm have not yet been assigned to any molecule or plant pigment.

Chappelle et al. (1984b) later showed in the laboratory that deficiencies in phosphorus, nitrogen, and iron in intact corn plants are manifested primarily by a decrease in the fluorescence of the 690- and 740-nm bands. This is in contrast to the fluorescence increase in potassium-deficient corn. While the underlying reasons for the fluorescence changes are not actually known, these studies do suggest the potential usefulness of LIF measurements for the remote detection of nutrient deficiencies in plants.

Laboratory studies by Chappelle et al. (1985) also suggest that individual plant species may potentially be identifiable. They were able to show that the 337.1-nm LIF spectra of five major plant types were sufficiently different to allow their identification. The plant types were herbaceous dicots and monocots, conifers, hardwoods, and algae. Each would be identified by (a) the presence or absence of one or more of the 440-, 525-, 685-, and 740-nm peaks or (b) the strength of one or more of the spectral fluorescence peaks relative to

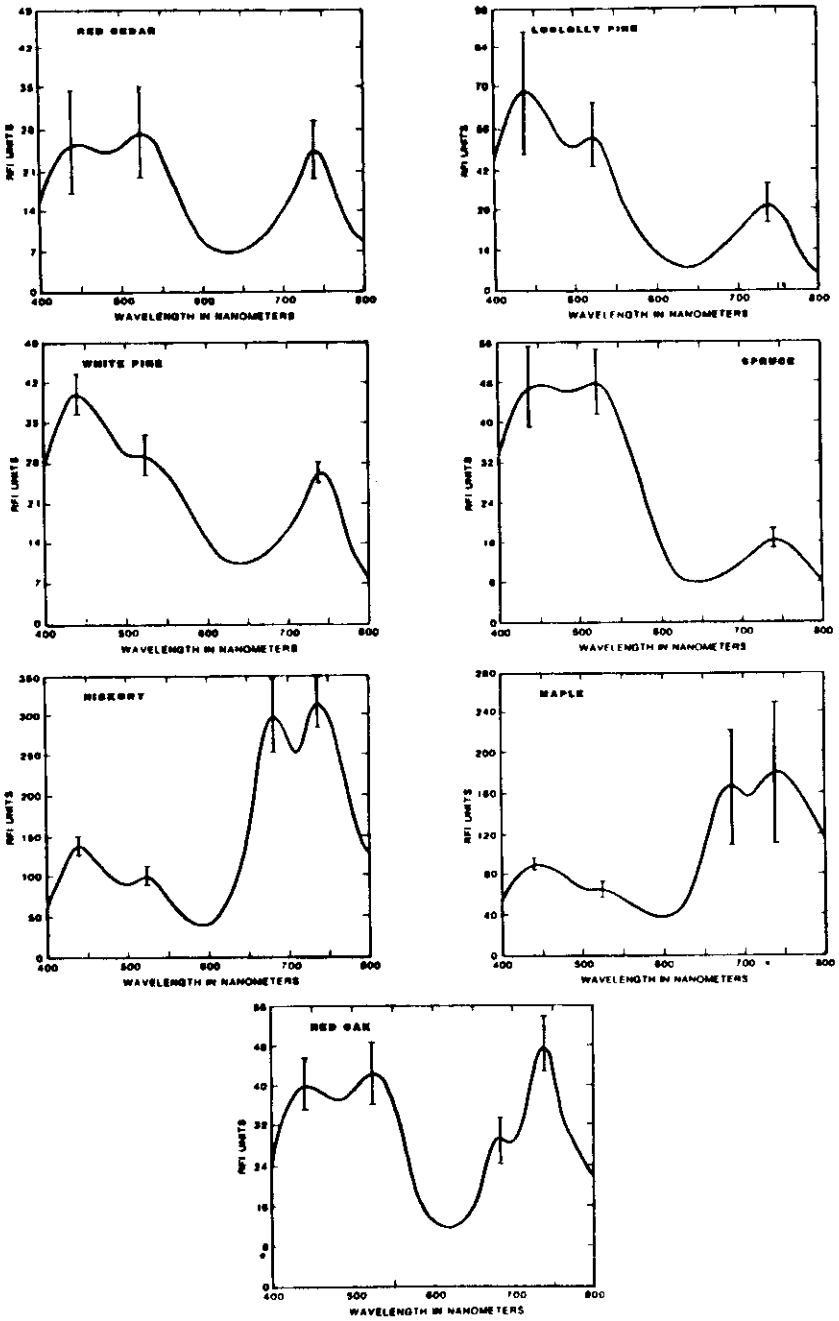

Figure 6.31. Laboratory 337.1-nm laser-induced fluorescence spectra of some selected conifers and hardwoods. Differences found in spectra suggests potential for discrimination of major plant types (Chappelle et al., 1985).

another. Typical 337.1-nm LIF spectra of some conifers and hardwoods are shown in Figure 6.31.

Celander et al. (1978) reported the 337.1-nm laboratory LIF of the foliages of eight different trees including conifers and hardwoods. While some fluorescence emission peaks were always seen in the 400–600-nm region, the lack of observable fluorescence in the 680–750-nm region is not understandable. However, they did observe ~685- and 730-nm chlorophyll fluorescence in grass and in so-called ground vegetation such as peat moss and reindeer lichen. Since the spectra by Celander et al. (1978) were uncorrected, one can only conjecture that the instrument response or sensitivity in the red region was quite reduced in comparison to that of Chappelle et al. (1985), who (1) used a PMT detector having good sensitivity into the red region and (2) further corrected their spectra for the remaining roll-off in the red portion of the spectrum.

Hoge et al. (1983) showed that the LIF spectral emissions are of sufficient strength to be easily detectable from airborne altitudes of 150 m. They used a 532-nm frequency-doubled Nd–YAG laser and an excimer-pumped dye laser at 422 nm integrated into the AOL to conduct airborne experiments over natural

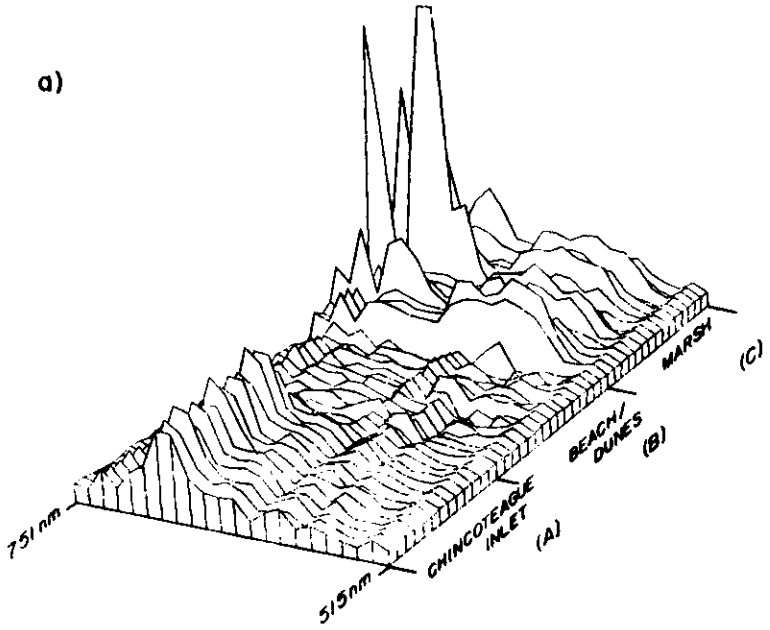

Figure 6.32. Individual, unaveraged laser-induced emission spectra obtained with AOL during overflight of (*a*) water, beach, and marsh portions of a flight line and (*b*) marsh, bush/tree, and marsh segments of same flight line. Pulse-to-pulse variability primarily induced by spatial variability of target and not system noise or solar background radiation (Hoge et al., 1983).

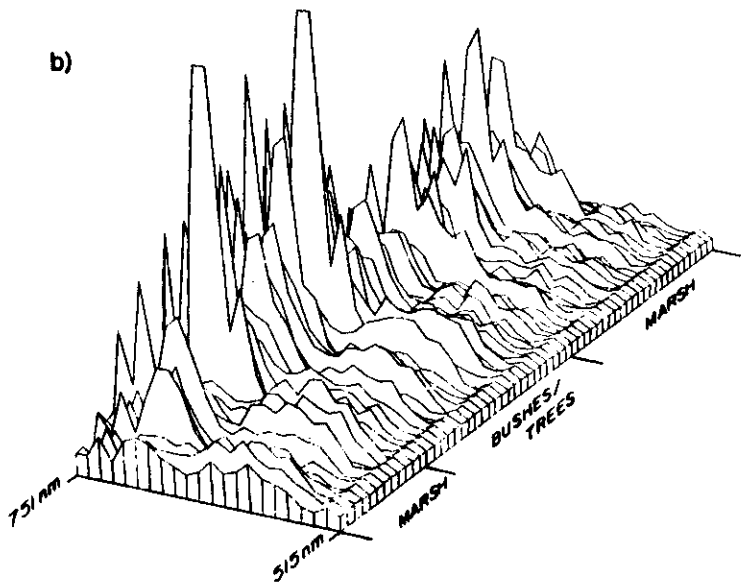

Figure 6.32. (*Continued*)

terrain. Grab samples were also collected by ground-truth teams to allow comparison of laboratory and airborne spectra. The dominant LIF peaks in the airborne and laboratory spectra were found at 690 and 740 nm and are due to chlorophyll. Figure 6.32*a* shows individual, or single-shot, 532-nm LIF spectral waveforms obtained during the course of a flight over marine water, beach, and marsh. Figure 6.32*b* shows a continuing portion of the flight line over marsh, bushes, and trees. Several important features of these spectra should be noted. The signal strength and the LIF spectral color are both highly variable over land targets (Figure 6.32*a*, section *C*) compared to marine targets (Figure 6.32*a*, section *A*). This pulse-to-pulse variability is caused by spatial variability of the target and is not a result of system noise or solar background radiation. The variability in the LIF chlorophyll fluorescence from marine targets is primarily caused by water surface gravity and capillary waves (once the water Raman has been used to correct for water column transmission variability).

The relative terrain and/or plant height were simultaneously measured by laser pulse time-of-flight measurements. These metric measurements offer further discrimination between trees, bushes, and grasses. Figure 6.33 shows the 685-nm chlorophyll fluorescence emission induced by the 422-nm, 100-kW, 5-ns dye laser pulses during the overflight. The on-wavelength backscattered return was utilized to obtain the plant and terrain elevation. Depth-resolved fluorescence techniques (similar to depth-resolved Raman backscatter, Section

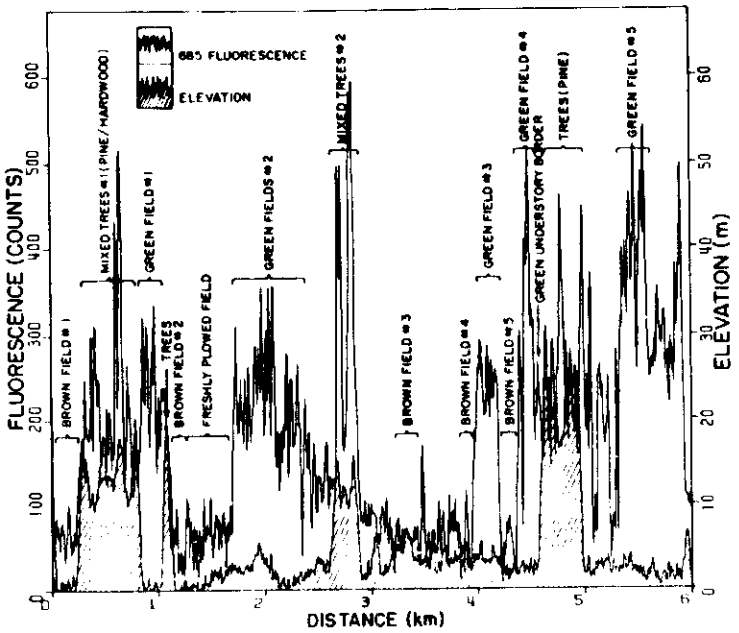

Figure 6.33. Profile of 422-nm LIF emission at 685 nm obtained across various targets of fields and trees. Terrain elevation shown by the cross-hatched profile. Note that some grass-covered fields yield fluorescence levels whose magnitude is approximately the same as that from stands of trees (Hoge et al., 1983).

6.2.2.4) can potentially allow the study of fluorescence emission as a function of leaf position on the plant if the laser pulse width and fluorescence emission response time are on the order of several nanoseconds or less.

We have shown that vegetation height and fluorescence are both measurable simultaneously. In Section 6.2.4 the success of bathymetry, and other water column measurements, was reviewed. The reader will quickly deduce that metric and fluorescence measurement (and wide-area mapping) feasibility studies for investigating submerged aquatic vegetation should be attempted. These measurements will, of course, be hampered by the attenuation of the water column but are nevertheless felt to be a natural extension of the previous bathymetry and plant terrain and fluorescence work.

Outside the United States and Canada, investigators in the USSR (Kanevskiy et al., 1983) have reported the laser irradiation (with a defocused beam) of leaves and subsequent image-intensifier recording of the 685-nm image from distances of 15–20 m. Such a system reportedly would not have adequate SNR for use at aircraft altitudes. They further reported use of a helicopter-borne lidar with a 440-nm, 15-mW laser (presumable He–Cd) to observe ~688 nm fluo-

rescence of leaves in a 10-nm bandpass from altitudes of 15–20 m during cloudy days. It was further suggested that pulsed lasers and larger receiving telescopes could substantially increase the operating altitudes. Not surprisingly, their laboratory LIF spectra of beet leaves obtained during the course of the program displayed an elevated 735-nm peak relative to the 685-nm band.

6.3.3 Laser-Induced Fluorescence of Surface Mineral Deposits

DeNeufville et al. (1981) performed extensive work to evaluate the remote sensing of laser-induced fluorescence of the uranyl ion as a potential indicator of uranium occurring in geologic materials at Earth's surface. The most important characteristics of the uranyl ion fluorescence are illustrated by the laboratory excitation and fluorescence spectra of an efflorescent film from the Hale Quarry near Portland, Connecticut (Figure 6.34). Kåsden et al. (1981) performed ground-based lidar fluorescence studies in a quarry known to have surface mineralization of the fluorescent uranyl ion UO_2^{2+} along its walls. They used a transmitter consisting of a flashlamp-pumped dye laser having a 35-mJ, 175-ns output at 425 nm in a 3-nm spectral bandwidth. The receiver consisted of an 18-cm reflecting telescope with a flexible filter/monochromator/PMT detector observing in the 490–600-nm spectral region. Efflorescent films and flakes of uranyl mineral were first located by visual fluorescence stimulated with a hand-held UV lamp. Then, the lidar was brought onto the target for remote measurements at distances of 32–40 m. The relative fluorescent brightness found was 330–1517 ppm A units, defined as 10^6 times the area concentration of meta-autunite that would have to be illuminated to observe the same brightness as measured from the target (deNeufville et al., 1981). During all the experiments, considerable temporal delay was inserted into the detection system since the fluorescence lifetimes varied from 154 to 398 μs. Based on the quarry measurements of fluorescence lifetime, the authors were then able to assign the shorter lifetime targets to the tetragonal (D_{4h}) uranyl minerals and the longer lived ones to D_{2h} or D_{3h} point symmetry such as possessed by liebigite, schroek-

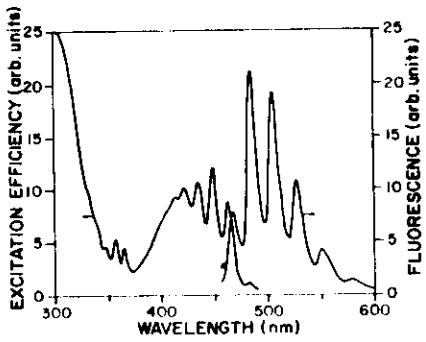

Figure 6.34. Excitation and fluorescence spectra of efflorescent film from Hale Quarry, Portland, CT. Emission at 5250 Å and excitation at 3300 Å, respectively. Chemical uranium 420–490 ppm (deNeufville et al., 1981).

ingerite, or andersonite (deNeufville et al., 1981). The fluorescence lifetime measurements were made with a filter detection system centered at 525 nm and having a 5-nm bandwidth.

Since a Fraunhofer line discriminator (FLD) (Watson, 1981) is able to detect luminescent rocks and minerals in daylight, it would seem natural to suggest that a lidar and a FLD be flown together on the same airborne platform to determine their complementarity (Chimenti, 1981).

Recently, laboratory evaluation of a laser fluorosensor was conducted to determine the feasibility of remotely detecting the fluorescent emission of organic effluents associated with coal processing (Capelle and Franks, 1979). This laser fluorosensor was able to separately accommodate N_2 or KrF excimer lasers and used a 20-cm modified Schmidt Cassegrain telescope and a filter-iris-PMT detector arrangement. For multichannel spectra, a PMT-monochromator and also an optical multichannel analyzer (OMA) were tested. The latter, of course, suffered from inadequate sensitivity. The N_2 lidar system was tested on a two-engine fixed-wing airborne platform at altitudes of 105–308 m over fabricated targets on the ground containing a coal solvent, quinine bisulfate, motor oil, and a detergent (Franks et al., 1983). The KrF implementation of the lidar was similarly flown over test targets at the Nevada Test Site, a naval petroleum reserve, and the Santa Barbara Channel oil field region. The 250-mJ, 249-nm KrF excimer produced a 16-ns pulse and was operated at 31 Hz. The detector consisted of a dichroic beam splitter to yield a visible channel (~ 360–460 FWHM) and a 290-nm UV channel, the latter using a solar blind CsTe PMT. Rather high SNRs were obtained, and petroleum-based by-products were detected in the visible spectral region from altitudes up to 610 m without PMT gating.

6.3.4 Terrain Imaging by Scanning Lidar Reflectance Measurements

During the course of airborne lidar experiments the on-wavelength pulse backscattered from the terrestrial target is most often used to (a) measure the aircraft slant range and/or tree height by temporal time-of-flight measurements or (b) synchronize, trigger, or otherwise gate a fluorosensor into active data acquisition at the proper time. The strength of this on-wavelength pulse is often recorded and infrequently used (Hoge et al., 1984), particularly in the mapping mode. This signal can, however, be used to advantage to image and delineate features on the ground and during postflight data analysis and in determining the position of the airborne platform upon completion of the mission. This mapping feature of the return pulse was investigated as a secondary objective of a recent geodynamic baseline monitoring experiment using aircraft laser ranging (Krabill et al., 1982). The NASA AOL was operated in the conical scan mode at 400 Hz using a 337.1-nm N_2 laser to interrogate a series of retroreflectors

placed at known positions along the runways and taxiways of the Wallops Flight Facility (Figure 6.35*a*). The retroreflectors were easily discriminated on the basis of their specular, often-saturated return signal. However, since all return pulse amplitudes and their spatial positions had been recorded, a 337.1-nm reflectance map was generated. This lidar reflectance map is shown in Figure 6.35*b*. Notice that the concrete taxiways and leftmost portion of the runway yielded similar return power, while the black macadem portion gave a reduced signal. The marsh and creek regions (see upper left, Figure 6.35*a*) showed significant reductions in signal, which allowed their easy delineation. Note, also, that the grassy regions both within the interior of the runway-taxiway complex and outside of it produced the same return signal strength. While little

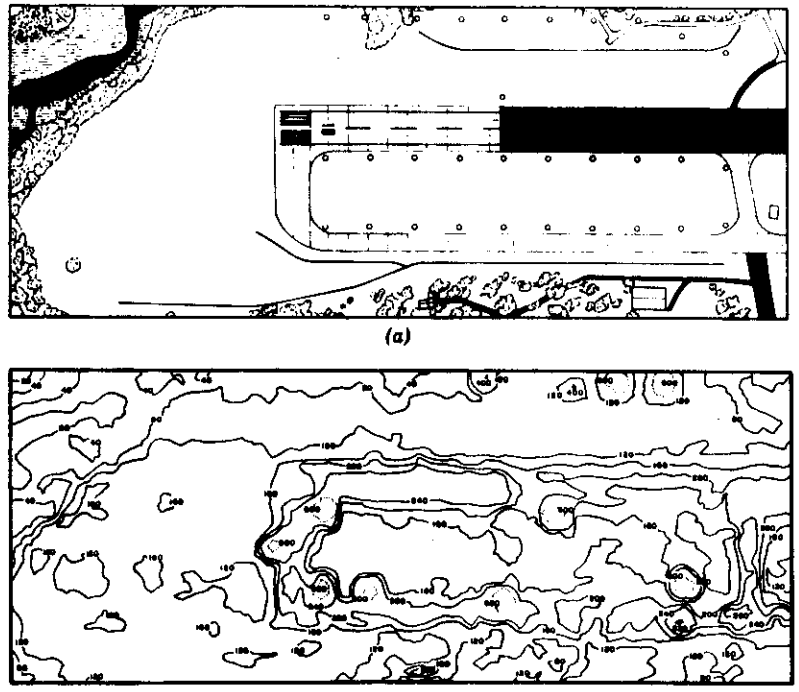

(a)

(b)

Figure 6.35. (*a*) Illustration of vegetation and terrain of selected test sites at Wallops Flight Facility. White, unaltered areas grass covered. Small circles denote location of retroreflectors deployed for baseline monitoring experiment. (*b*) Contour map of surface return signal intensity from target region in (*a*). Taxiways, runways, creek, and bushes as well as interrogated retroreflectors discriminated on basis of return signal strength.

analytical and algorithm development effort was expended in this modest effort, it shows the potential that exists, particularly when one notes that this lidar reflectance map was generated from data taken in total darkness. Considering the LIF of chlorophyll in trees, bushes, and grasses demonstrated recently (Hoge et al., 1983), numerous multiwavelength fluorescence images could also be generated with a single overflight. The high-repetition-rate metal vapor lasers operating in the visible would be a possible transmitter source. However, eye safety may then become more of a concern than when UV lasers are used. If military mapping research is the objective, this visible source may also be less desirable than UV laser transmitters.

6.4 FUTURE PROSPECTS FOR OCEANIC AND TERRESTRIAL LIDAR MEASUREMENTS

Oceanic and terrestrial lidar research and applications are both emerging fields that combine science, engineering, and technology. Exciting concepts have been proposed and investigated to date in ground-based laboratories and from shipboard and airborne platforms. Still newer and more sophisticated ideas will no doubt be proposed and tried. Hopefully, operation from Earth-orbiting satellite platforms will allow global oceanic and terrestrial lidar applications to be successfully pursued to operational status. The laser altimeter in the Apollo 15 orbital science payload certainly demonstrated that lidar operation from a satellite platform is feasible (Kaula et al., 1972).

For satellite applications, scaling the laser transmitters to higher powers (and receivers to larger apertures) will allow feasibility estimates to be quickly obtained in terms of prime power and sheer system weight and volume required for Earth orbit deployment. New problems and considerations such as eye safety and atmospheric two-way attenuation factors may require attention. As with present satellite sensors, the systems to handle the volume of data generated by global sensing will remain a challenge, especially if large numbers of fluorosensor bands are necessarily implemented.

Oceanic and terrestrial lidar systems will probably be erected (at least in part) upon the foundations of shuttle atmospheric lidar research (Browell, 1979) for winds (Huffaker, 1978), species and aerosol determination (Browell, 1983; Menzies and Shumate, 1978) as well as topography (Kobrick et al., 1981), and satellite Earth crustal motion experiments (Kahn et al., 1979).

Relative to the hydrosphere, many of the fundamental or basic problems have been listed and discussed, especially with regard to their possible solution by remote sensing (Goldberg, 1979). Certainly ship, aircraft, and satellite platforms carrying both active and passive sensors must all share a portion of the workload. Lidar sensors must continue to play a role in airborne sensing but must at the same time become established in the satellite platform domain. All scientists can look with fond hope to the use of satellite-based lidar systems to help provide answers to the many land, ocean, and atmospheric research questions. These three latter portions of Earth form a coupled, dynamic system, and the high temporal and spectral specificity of lidar data can, as well as any known sensor, help lace together the answers to many of the interdisciplinary questions of Earth science.

REFERENCES

Abramov, O. I., V. I. Yeremin, L. I. Lobov, and V. V. Polovinko (1977). Use of Lidar to Detect Oil Pollution on the Sea Surface. *Izv., Atmos. Oceanic Phys.* **13**(3), 232–234.

Abramowitz, M., and I. A. Stegun, eds. (1964). *Handbook of Mathematical Functions*, Dover, New York.

Arnush, D. (1972). Underwater Light-Beam Propagation in the Small-Angle-Scattering Approximation. *J. Opt. Soc. Am.* **62**, 1109–1111.

Bobb, L. C., G. Ferguson, and M. Rankin (1978). Laser Irradiance in the Sea: Theory and Experiment. Report No. NADC 78253-30, Naval Air Development Center, Warminster, Pennsylvania.

Bogorodskiy, V. V., M. A. Kropotkin, and T. Yu Sheveleva (1977). Determination of Oil Contamination of Water by a Scanning Optical Radar (Lidar). *Izv., Atmos. Oceanic Phys.* **13**(3), 914–917.

Bowman, M. J., and W. E. Esaias, eds., (1977). Oceanic Fronts in Coastal Processes. Proceedings of a Workshop held at the Marine Sciences Research Center, May 25–27, 1977, Springer-Verlag, New York.

Brach, E. J., J. M. Molnar, and J. T. Jasmin (1977). Detection of Lettuce Maturity and Variety by Remote Sensing Techniques. *J. Agric. Eng. Res.* **22**, 45–54.

Brach, E. J., M. A. Klyne, T. Phan, and J. J. Jasmin (1978). Use of Laser Fluorescence to Study Lettuce Growth and Development Under Controlled Environment. *Proc. Soc. Photo-Opt. Instrum. Eng.* **158**, 156–162.

Brach, E. J., B. Gasman, and L. J. Croix (1982). Development of a Laser Fluorosensor for Cultivars and Species Indentification of Grain Crops. *Z. Acker Pflanzenbau (J. Agron. Crop Sci.)* **151**, 6–16.

Bravo-Zhivotovskiy, D. M., L. S. Dolin, A. G. Luchinin, and V. A. Savel'yev (1969). Structure of a Narrow Light Beam in Sea Water. *Izv., Atmos. and Oceanic Phys.* **5**, 160–167.

Bristow, M. P. F. (1978). Airborne Mapping of Surface Water Pollutants by Fluorescence Spectroscopy. *Remote Sensing of Environment* **7**, 105–127.

Bristrow, M., and D. Nielsen (1981). Remote Monitoring of Organic Carbon in Surface Waters. Report No. EPA-80/4-81-001, U.S. Environmental Protection Agency, Las Vegas, Nevada.

Bristow, M., D. Nielsen, D. Bundy, and F. Furtek (1981). Use of Water Raman Emission to Correct Airborne Laser Fluorosensor Data for Effects of Water Optical Attenuation. *Appl. Optics* **20,** 2889–2906.

Bristow, M. P. F., W. R. Houston, and R. M. Measures (1973). Development of a Laser Fluorosensor for Airborne Surveying of the Aquatic Environment, in *The Use of Lasers for Hydrographic Studies*, H. H. Kim and P. T. Ryan, eds., NASA SP-375, Proceedings of a Symposium held at Wallops Island, Virginia, September 12, 1973, pp. 119–145, Washington, D.C.

Brockmann, U. H., H. Huhnerfuss, G. Kattner, H.-C. Broecker, and Gunter Hentzschel (1982). Artificial Surface Films in the Sea Area Near Syh. *Limnology and Oceanography* **27,** 1050–1058.

Browell, E. V. (1977). Analysis of Laser Fluorosensor Systems for Remote Algae Detection and Quantification. NASA TN D-8447, Washington, D.C.

Browell, E. V., ed. (1979). Shuttle Atmospheric Lidar Research Program. NASA SP-433, Washington, D.C.

Browell, E. V. (1983). NASA Multi-Purpose Airborne DIAL System and Measurements of Ozone and Aerosol Profiles. *Appl. Optics* **22,** 522–534.

Brown, J. S., and M. R. Michel-Wolwertz (1968). Chlorophyll Fluorescence Near 720 μm in Englena Extracts. *Biomchem. Biophys. Acta* **155,** 288–290.

Bufton, J. L., F. E. Hoge, and R. N. Swift (1983). Airborne Measurements of Laser Backscatter from the Ocean Surface. *Appl. Optics* **22,** 2603–2618.

Burlamacchi, P., G. Cecchi, P. Mazzinghi, and L. Pantani (1983). Performance Evaluation of UV Source for Lidar Fluorosensing of Oil Films. *Appl. Optics* **22,** 48–53.

Byrnes, H. J., and S. L. Fagin (1978). Optimal Filtering and Analysis of Scanning Laser Data. Naval Ocean Research and Development Activity (NORDA) Technical Note No. 24, NSTL Station, MS.

Campbell, J. W., and W. E. Esaias (1983). Basis for Spectral Curvature Algorithms in Remote Sensing of Chlorophyll. *Appl. Optics* **22,** 1084–1093.

Campbell, J. W., and J. P. Thomas, eds. (1981). The Chesapeake Bay Plume Study, Superflux 1980. Proceedings of a Conference held in Williamsburg, VA, January 21–23, 1981, NASA Conference Proceedings Document CP-2188.

Capelle, G. A., and L. A. Franks (1979). Laboratory Evaluation of Two Laser Fluorosensor Systems. *Appl. Optics* **18,** 3579–3586.

Capelle, G. A., L. A. Franks, and D. A. Jessup (1983). Aerial Testing of a KrF Laser-Based Fluorosensor. *Appl. Optics* **22,** 3382–3387.

Celander, L., K. Fredriksson, B. Galle, and S. Svanberg (1978). Investigation of Laser-Induced Fluorescence with Applications to Remote Sensing of Environmental Parameters. Gotenburg Institute of Physics, Report No. GIPR-149, Gotenberg, Sweden.

Chapman, W. H. (1982). Aerial Profiling of Terrain System, in Proceedings of Surveying Requirements Meeting, February 2–5, 1982, U.S. Army Engineer Waterways Experiment Station, Vicksburg, MS, pp. 247–260.

Chappelle, E. W., F. W. Wood, Jr., J. E. McMurtrey III, and W. W. Newcomb (1984a). Laser-Induced Fluorescence of Green Plants. 1: A Technique for the Remote Detection of Plant Stress and Species Differentiation. *Appl. Optics* **23,** 134–138.

Chappelle, E. W., J. E. McMurtrey III, F. M. Wood, Jr., and W. W. Newcomb (1984b). Laser-Induced Fluorescence of Green Plants. 2: LIF Caused by Nutrient Deficiencies in Corn. *Appl. Optics* **23,** 139–142.

Chappelle, E. W., F. M. Wood, Jr., W. W. Newcomb, and J. E. McMurtrey, III (1985). Laser-Induced Fluorescence of Green Plants. 3: LIF Spectral Signatures of Five Major Plant Types. *Appl. Optics* **24,** 74–80.

Chimenti, R. J. L. (1981). Optical Characteristics of Uranyl Geologic Targets, in *Workshop in Applications of Luminescence Techniques to Earth Resource Studies*, W. R. Hemphill and M. Settle, ed., LPI Technical Report 81-03, Lunar and Planetary Institute, Houston, pp. 69–71.

Choy, L. W., D. L. Hammond, and E. A. Uliana (1984). Electromagnetic Bias of 10 GHz Radar Altimeter Measurements of MSL. *Marine Geodesy* **8,** 297–312.

Christman, R. F., and M. Ghasseni (1966). Chemical Nature of Organic Color in Water. *J. AWWA* 723–731.

Clegg, J. E., and M. F. Penny (1977). Depth Sounding from the Air by Laser Beam. *Navigation (Australia)* **5** 541–547.

Cox, C., and W. Munk (1954). Measurement of the Roughness of the Sea Surface from Photographs of the Sun's Glitter. *J. Opt. Soc. Am.* **44,** 838–850.

Cronan, C. S., and C. L. Schofield (1979). Aluminum Leaching Response to Acid Precipitation: Effects of High Elevation Watershed in Northeast. *Science* **204,** 304–306.

deNeufville, J. P., A. Kasden, and R. J. L. Chimenti (1981). Selective Detection of Uranium By Laser-Induced Fluorescence: A Potential Remote-Sensing Technique. 1: Optical Characteristics of Uranyl Geological Targets. *Appl. Optics* **20,** 1279–1296.

El-Sayed, S. A. (1970). Phytoplankton Production of the South Pacific and the Pacific Sector of the Antarctic. *Scientific Exploration of the South Pacific*, National Academy of Sciences, Washington, D.C.

Enabnit, D. B., L. R. Goodman, G. K. Young, and W. J. Shaughnessy (1978). The Cost Effectiveness of Airborne Laser Hydrography. National Oceanic and Atmospheric Administration Technical Memorandum NOS-26, Rockville, MD.

Enabnit, D. B., G. C. Guenther, J. Williams, and F. Skove (1981). An Estimate of the Area Surveyable with an Airborne Laser Hydrography System at Ten U.S. Sites. National Oceanic and Atmospheric Administration Technical Report OTES-5, Rockville, MD.

Exton, R. J., W. M. Houghton, W. Esaias, L. W. Haas, and D. Hayward (1983). Spectral Differences and Temporal Stability of Phycoerythrin Fluorescence in Estuarine and Coastal Waters Due to the Domination of Labile Cryptophytes and Stabile Cyanobacteria. *Limnology and Oceanography* **28,** 1225–1231.

Fantasia, J. F., and H. C. Ingrao (1974). Development of Experimental Airborne Laser Remote Sensing System for the Detection and Classification of Oil Spills. *Proc. of*

the 9th Intern. Symp. on Remote Sensing of the Environment, 15–19 April 1974, Paper 10700-1-X, 1711–1745.

Fantasia, J. F., T. M. Hard, and H. C. Ingrao (1971). An Investigation of Oil Fluorescence as a Technique for Remote Sensing of Oil Spills, Report No. DOT-TSC-USCG-71-7, Transportation Systems Center, Dept. of Transportation, Cambridge, MA.

Fork, R. L., C. V. Shank, and R. T. Yen (1982). Amplification of 70-fs Optical Pulses to Gigawatt Powers. *Appl. Phys. Lett.* **41**, 223–225.

Franks, L. A., G. A. Capelle, and D. A. Jessup (1983). Aerial Testing of an N_2 Laser Fluorosensor System. *Appl. Optics* **22**, 1717–1721.

Fredriksson, K., B. Galle, K. Nystrom, S. Svanberg, and B. Ostrom (1979). Marine Laser Probing: Results from a Field Test. Department of Physics, Chalmers University Report No. 245, Gotenberg, Sweden.

Friedman, E. J., and G. D. Hickman (1971). Laser-Induced Fluorescence in Algae: A New Technique for Remote Detection. Final Report, sponsored by NASA, Wallops Island, VA, under Contract NAS6-02081, Sparcom, Inc., Alexandria, VA.

Gardner, C. S. (1982). Target Signatures for Laser Altimeters: An Analysis. *Appl. Optics* **21**, 448–453.

Garrett, W. D. (1983). Frequency and Distribution of Natural and Pollutant Organic Sea Slicks. NRL Memorandum Report #5075, Naval Research Laboratory, Washington, D.C.

Gehlhaar, U. (1982). Computer Simulations and Theory of Oceanograpic Fluorescence Lidar Signals: Effect of Sea Surface Structure. *Appl. Optics* **21**, 3743–3755.

Goldberg, E. D., ed. (1979). Remote Sensing and Problems of the Hydrosphere. National Aeronautics and Space Administration (NASA) Conference Publication 2109, Washington, D.C.

Gordon, H. R. (1982). Interpretation of Airborne Oceanic Lidar: Effects of Multiple Scattering. *Appl. Optics* **21**, 2996–3001.

Gordon, H. R., D. K. Clark, J. W. Brown, R. H. Evans, and W. W. Broenkow (1983) Phytoplankton Pigment Concentrations in the Middle Atlantic Bight: Comparison of Ship Determinations and CZCS Estimates. *Appl. Optics* **22**, 20–36.

Govindjee, and R. Govindjee (1974). The Absorption of Light in Photosynthesis. *Sci. Am.* **231**(6), 68–82.

Grew, G. W., and L. S. Mayo (1983). Ocean Color Algorithm for Remote Sensing of Chlorophyll. NASA Technical Paper 2164, Langley Research Center, Hampton, VA.

Hayne, G. S. (1980). Radar Altimeter Mean Return Waveforms from Near-Normal-Incidence Ocean Surface Scattering. NASA Contractor Report 156864, prepared by Applied Science Associates under Contract NAS6-2810.

Hickman, G. D. (1973). Recent Advances in the Application of Pulsed Lasers to the Hydrosphere. NASA Conference on the Use of Lasers for Hydrographic Studies, NASA SP-375, 81–88.

Hickman, G. D., and J. E. Hogg (1969). Application of an Airborne Pulsed Laser for Near Shore Bathymetric Measurements. *Remote Sensing of Environment* **1**, 47–58.

Hickman, G. D., and R. B. Moore (1970). Laser Induced Fluorescence in Rhodamine and Algae. Proc. 13th Conf. Great Lakes Res., Int. Assoc. Great Lakes Res., 1–14.

Hoge, F. E. (1982). Laser Measurements of the Spectral Extinction Coefficients of Fluorescent, Highly Absorbing Liquids. *Appl. Optics* **21**, 1725–1729.

Hoge, F. E. (1983). Oil Film Thickness Using Airborne Laser-Induced Oil Fluorescence Backscatter. *Appl. Optics* **22**, 3316–3318.

Hoge, F. E., and J. S. Kincaid (1980). Laser Measurement of Extinction Coefficients of Highly Absorbing Liquids. *Appl. Optics* **19**, 1143–1150.

Hoge, F. E., and R. N. Swift (1980). Oil Film Thickness Measurement Using Airborne Laser-Induced Water Raman Backscatter. *Appl. Optics* **19**, 3269–3281.

Hoge, F. E., and R. N. Swift (1981a). Absolute Tracer Dye Concentration Using Airborne Laser-Induced Water Raman Backscatter. *Appl. Optics* **20**, 1191–1202.

Hoge, F. E., and R. N. Swift (1981b). Airborne Simultaneous Spectroscopic Detection of Laser Induced Water Raman Backscatter and Fluorescence from Chlorophyll-a, and other Naturally Occurring Pigments. *Appl. Optics* **20**, 3197–3205.

Hoge, F. E., and R. N. Swift (1981c). Application of the NASA Airborne Oceanographic Lidar to the Mapping of Chlorophyll and Other Organic Pigments. The Chesapeake Bay Plume Study, Superflux 1980, J. W. Campbell and J. P. Thomas, eds., NASA Conference Proceedings Document CP2188.

Hoge, F. E., and R. N. Swift (1982a). Airborne Laser-Induced Fluorescence of Upper Water Column Constituents of a Warm Core Gulf Stream Ring. *Trans. Amer. Geophys. Union* **63**(3), 60.

Hoge, F. E., and R. N. Swift (1982b). Delineation of Estuarine Fronts in the German Bight Using Airborne Laser-Induced Water Raman Backscatter and Fluorescence of Water Column Constituents. *Int. J. Remote Sening* **3**(4), 475–495.

Hoge, F. E., and R. N. Swift (1983a). Experimental Feasibility of the Airborne Measurement of Absolute Oil Fluorescence Spectral Conversion Efficiency. *Appl. Optics* **22**, 37–47.

Hoge, F. E., and R. N. Swift (1983b). Airborne Dual-Laser Excitation and Mapping of Phytoplankton Photopigments in a Gulf Stream Warm Core Ring. *Appl. Optics* **22**, 2272–2281.

Hoge, F. E., and R. N. Swift (1983c). Airborne Detection of Oceanic Turbidity Cell Structure Using Depth-Resolved Laser-Induced Water Raman Backscatter. *Appl. Optics* **22**, 3778–3786.

Hoge, F. E., and R. N. Swift (1985). Airborne Mapping of Laser-Induced Fluorescence of Chlorophyll *a* and Phycoerythrin in a Gulf Stream Warm Core Ring. Paper No. 18 in *Mapping Strategies in Chemical Oceanography*, A. Zirino, ed., *Advances in Chemistry Series*, No. 209, American Chemical Society, Washington, D.C., pp. 353–372.

Hoge, F. E., R. N. Swift, and E. B. Frederick (1980). Water Depth Measurement Using an Airborne Pulsed Neon Laser System. *Appl. Optics* **20**, 1191–1202.

Hoge, F. E., R. N. Swift, and J. K. Yungel (1983). Feasibility of Airborne Detection

of Laser-Induced Fluorescence of Green Terrestrial Plants. *Appl. Optics* **22**, 2991–3000.

Hoge, F. E., W. B. Krabill, and R. N. Swift (1984). The Reflection of Airborne UV Laser Pulses from the Ocean. *Marine Geodesy* **8**, 313–344.

Horvath, R., W. L. Morgan, and S. R. Stewart (1971). Optical Remote Sensing of Oil Slicks: Signature Analysis and Systems Evaluation. Project 724104.2/1, Willow Run Laboratories, University of Michigan, Ann Arbor, Michigan.

Houghton, W. M. (1973). A Remote Sensing Laser Fluorometer, in *The Use of Lasers for Hydrographic Studies*, H. H. Kim and P. T. Ryan, eds., NASA SP-375, Proceedings of a Symposium held at Wallops Island, Virginia, September 12, 1973. NASA, Washington, D.C.

Houghton, W. M., R. J. Exton, and R. W. Gregory (1983). Field Investigation of Technique for Remote Laser Sensing of Oceanographic Parameters. *Remote Sensing of Environment* **13**, 17–32.

Huang, N. E., S. R. Long, C. C. Tung, Y. Yuan, and L. F. Bliven (1983). A Non-Gaussian Statistical Model for Surface Elevation of Nonlinear Random Wave Fields. *J. Geophys. Res.* **88**, 7597–7606.

Huang, N. E., S. R. Long, L. F. Bliven, and C. C. Tung (1984). The Non-Gaussian Joint Probability Density Function of Slope and Elevation for a Nonlinear Gravity Wave Field. *J. Geophys. Res.* **89**, 1961–1972.

Huffaker, R. M. (1978). Feasibility Study of Satellite-Borne Lidar Global Wind Monitoring System. National Aeronautics and Space Administration, Document TM-ERL-WPL-37.

Huhnerfuss, H., and W. D. Garrett (1981). Experimental Sea Slicks: Their Practical Applications and Utilization for Basic Studies of Air-Sea Interactions. *J. Geophys. Res.* **86**, 439–447.

Huhnerfuss, H., W. Alpers, and W. L. Jones (1978). Measurements at 13.9 GHz of Radar Backscattering Cross-Section of the North Sea Covered with an Artificial Surface Film. *Radio Science* **13**, 979–983.

Huhnerfuss, H., W. Alpers, W. L. Jones, P. A. Lange, and K. Richter (1981). The Damping of Ocean Surface Waves by a Monomolecular Film Measured by Wave Staffs and Microwave Radars. *J. Geophys. Res.* **86**, 429–438.

Huhnerfuss, H., W. Alpers, W. D. Garrett, P. A. Lange, and S. Stolte (1983a). Attenuation of Capillary and Gravity Waves at Sea by Monomolecular Organic Surface Films. *J. Geophys. Res.* **88**, 9809–9816.

Huhnerfuss, H., W. Alpers, A. Cross, W. D. Garrett, W. C. Keller, P. A. Lange, W. J. Plant, F. Schlude, D. L. Schuler (1983b). The Modification of *X* and *L* Band Radar Signals by Monomolecular Sea Slicks. *J. Geophys. Res.* **88**, 9817–9822.

Huhnerfuss, H., W. Garrett, and F. E. Hoge (1986). The Discrimination Between Crude Oil Spills and Monomolecular Sea Slicks by Airborne Lidar. submitted to *International Journal of Remote Sensing*, **7**(1), 137–150.

Jarrett, Olin, Jr., W. E. Esaias, C. A. Brown, Jr., and E. B. Pritchard (1981). Analysis of ALOPE Data from Superflux, in *Chesapeake Bay Plume Study, Superflux 1980*, J. W. Campbell and J. P. Thomas, eds., NASA Conf. Pub. 2188, NOAA/NEMP III 81 ABCDFG 0042, NASA Langley Research Center, Hampton, VA, pp. 405–411.

Jelalian, A. V. (1968). Sea Echo at Laser Wavelengths. *Proc. IEEE* **56**, 828–835.

Jensen, H. (1967). Performance of an Airborne Laser Profiler, in Airborne Photo-Optical Instrumentation; Proceedings of a Seminar In-Depth, Society of Photo-Optical Instrumentation Engineers, pp. VIII-1–VIII-6.

Jensen, H., and K. A. Ruddock (1965). Applications of a Laser Profiler to Photogrammetric Problems. Paper presented to Amer. Soc. of Photogrammetry, Washington, D.C.

Jerlov, N. G. (1976). *Marine Optics*, Oceanography Series 14, Elsevier, Amsterdam.

Kahn, W. D., F. O. Vonbun, D. E. Smith, T. S. Englar, and B. P. Gibbs (1979). Performance Analysis of the Spaceborne Laser Ranging System. NASA Technical Memorandum 80330, Goddard Space Flight Center, Greenbelt, MD.

Kalle, K. (1966). The Problem of the Gelbstoff in the Sea. *Oceanogr. Mag. Biol. Ann. Rev.* **4**, 91–104.

Kanevskiy, V. A., V. S. Fedak, F. v. Ryazantsev, V. P. Il'in, Yu. R. Shelyag-Sosonko, S. M. Kochubey, and M. G. Sosonkin (1983). Opyt Primeneniye Electronno-Opticheskikh Sistem Dlya Distantsionnogo Issledovaniya Lyuminetsentsii Rastency. *Issledovaniye Zemli iz Kosmosa* **6**, 87–90.

Karp, S. (1976). Optical Communication between Underwater and above Surface (Satellite) Terminals. *IEEE Trans. Comm.* **COM-24**, 66–81.

Kasden, H. R., J. L. Chimenti, and J. P. deNeufville (1981). Selective Detection of Uranium by Laser-Induced Fluorescence: A Potential Remote-Sensing Technique. 2: Experimental Assessment of the Remote Sensing of Uranyl Geological Targets. *Appl. Optics* **30**, 1297–1307.

Kats, A. V., and I. S. Spevak (1980). Reconstruction of the Seawave Spectra from the Measurements of Moving Sensors. *Izv. Atmos. Ocean. Phys.* **16**, 194–200.

Kaula, W. M., G. Schubert, R. E. Lingenfelter, W. L. Sjogren, and W. R. Wollenhaupt (1972). Analysis and Interpretation of Lunar Laser Altimetry. Proceedings of Third Lunar Science Conference (Supplement 3, *Geochemica et Cosmochimica Acta*) **3**, 2189–2204.

Ketchem, R. D., Jr. (1971). Airborne Laser Profiling of the Arctic Ice Pack. *Remote Sensing of Environment* **2**, 41–52.

Kim, H. H. (1973). New Algae Mapping Technique by the Use of an Airborne Laser Fluorosensor. *Appl. Optics* **12**, 1454–1459.

Kim, H. H. (1977). Airborne Bathymetric Charting Using Pulsed Blue-Green Lasers. *Appl. Optics* **16**, 46–56.

Kim, H. H., P. O. Cervenka, and C. B. Lankford (1975). Development of an Airborne Laser Bathymeter. NASA TN-D-8079, October.

Kobrick, M., and C. Elachi (1981). A Shuttle Scanning Laser Altimeter for Topographic Mapping, in *Proceedings International Symposium on Remote Sensing of Environ-*

ment, Vol. 2, Environmental Research Institute of Michigan, Ann Arbor, MI, pp. 711–714.

Koerber, R. W., and D. M. Phillips (1982). Monte Carlo Simulation of Laser Backscatter from Sea Water. Tech. Report ERL-0224-TR, Department of Defense, Defense Science and Technology Organization, Electronics Research Laboratory, Adelaide, South Australia.

Krabill, W. B., and C. F. Martin (1983). Analysis of Aircraft Vertical Positioning Accuracy Using a Single Accelerometer. NASA Technical Memorandum 84417, Goddard Space Flight Center, Wallops Flight Facility, Wallops Island, VA.

Krabill, W. B., and R. N. Swift (1982). Preliminary Results of Shoreline Mapping Investigations Conducted At Wrightsville Beach, NC, in Proceedings of Surveying Requirements Meeting, February 2–5, 1982, U.S. Army Engineer Waterways Experiment Station, Vicksburg, MS, pp. 261–280.

Krabill, W. B., J. G. Collins, R. N. Swift, and M. L. Butler (1980). Airborne Laser Topographic Mapping Results from Initial Joint NASA/U.S. Army Corps of Engineers Experiment. NASA Technical Memorandum No. 73287, Wallops Island, VA.

Krabill, W. B., F. E. Hoge, and C. F. Martin (1982). Baseline Monitoring Using Aircraft Laser Ranging. NASA Technical Memorandum No. 73298, Wallops Island, VA.

Krabill, W. B., J. G. Collins, L. E. Link, R. N. Swift, and M. L. Butler (1984). Airborne Laser Topography Mapping Results. *Photogrammetric Engineering and Remote Sensing* **50,** 685–694.

Kung, R. T. V., and I. Itzkan (1976). Absolute Oil Fluorescence Conversion Efficiency. *Appl. Optics* **15,** 409–415.

Leonard, D. A., B. Caputo, and F. E. Hoge (1979). Remote Sensing of Subsurface Water Temperature by Raman Scattering. *Appl. Optics* **13,** 1732–1745.

Lerner, R. M., and J. D. Summers (1982). Monte Carlo Description of Time- and Space-Resolved Multiple Scatter in Natural Water. *Appl. Optics* **21,** 861–869.

Link, L. E., W. B. Krabill, and R. N. Swift (1983a). Prospectus on Airborne Laser Mapping System, in *Highway Geometries, Interactive Graphics, and Laser Mapping*, Transportation Research Record No. 923, National Research Council, National Academy of Sciences, Washington, D.C., pp. 1–7.

Link, L. E., W. B. Krabill, and R. N. Swift (1983b). A Prospectus on Airborne Laser Mapping Systems. Proceedings of Symposium and Workshop on Remote Sensing and Mineral Exploration, Ottawa, Canada, May 16–June 2, 1982, *Advances in Space Research*, Vol. 3, 309–322.

Long, R. B. (1979). On Surface Gravity Wave Spectra Observed in a Moving Frame of Reference. National Oceanic and Atmospheric Administration Technical Memorandum ERL AOML-38.

Luchinin, A. G. (1979). Influence of Wind Waves on the Characteristics of the Light Field Backscattered by the Bottom and the Intervening Water. *Izv., Atmos. Oceanic Phys.* **15,** 53–533.

Luchinin, A. G., and I. A. Sergiyevskaya (1982). On the Light Field Fluctuations Beneath a Wavy Sea Surface. *Izv. Atmos. and Oceanic Phys.* **18,** 656–661.

Maclean, G. A. (1982). Timber Volume Estimation Using Cross-Sectional Photogrammetric and Densitometric Methods, Masters Thesis, University of Wisconsin, p. 227.

Makarevich, S. A., A. P. Ivanov, and G. K. Il'ich (1969). The Structure of a Narrow Light Beam Emerging from a Layer of a Scattering Medium. *Izv., Atmos. Oceanic Phys.* **5,** 77–83.

Mamon, G., D. G. Youmans, Z. G. Sztankay, and C. E. Mongan (1978). Pulsed GaAs Laser Terrain Profiler. *Appl. Optics* **17,** 868–877.

McClain, C. R., D. T. Chen, and D. L. Hammond (1980). Gulf Stream Ground Truth Project: Results of the NRL Airborne Sensors. *Ocean Eng.* **7,** 55–97.

McClain, C. R., D. T. Chen, and W. Hart (1982a). On the Use of Laser Profilometry for Ocean Wave Studies. *J. Geophys. Res.* **87,** 9509–9515.

McClain, C. R., N. E. Huang, and P. E. LaViolette (1982b). Measurements of Sea-State Variations Across Oceanic Fronts Using Laser Profilometry. *J. Phys. Ocean* **12,** 1228–1244.

McGoogan, J. T., and E. J. Walsh (1979). Real-Time Determination of Geophysical Parameters from a Multibeam Altimeter, in *Remote Sensing of Earth from Space: Role of Smart Sensors*, Roger A. Breckenridge, ed., Vol. 67, *Progress in Astronautics and Aeronautics*, Paper No. 78-1735 of AIAA/NASA Conference on Smart Sensors Nov. 14–16, 1978, Hampton, VA.

Measures, R. M. (1984). *Laser Remote Sensing*, Wiley, New York.

Measures, R. M., and M. Bristow (1971). The Development of a Laser Fluorosensor for Remote Environmental Probing. Joint Conference on Sensing of Environmental Pollutants, Palo Alto, Nov. 1971, AIAA Paper 71-112; *Can. Aeron. Space J.* **17,** 421–422.

Measures, R. M., W. R. Houston, and D. G. Stephenson (1974). Laser Induced Fluorescence Decay Spectra—A New Form of Environmental Signature. *Opt. Eng.* **13,** 494–450.

Measures, R. M., J. Garlick, W. R. Houston, and D. G. Stephenson (1975). Laser Induced Spectral Signatures of Relevance to Environmental Sensing. *Can. J. Remote Sensing* **1,** 95–102.

Menzies, R. T., and M. S. Shumate (1978). Tropospheric Ozone Distribution Measured with an Airborne Laser Absorption Spectrometer. *Geophys. Res.* **83,** 4039–4043.

Mumola, P. B., and H. H. Kim (1972). Remote Sensing of Marine Plankton by Dye Laser Induced Fluorescence. Proc. of Conference, Engineering in the Ocean Environment. *IEEE* **3,** 204–207.

Mumola, P. B., O. Jarrett, Jr., and C. A. Brown, Jr. (1973). Multiwavelength Lidar for Remote Sensing of Chlorophyll *a* in Algae and Phytoplankton. NASA Conference on the Use of Lasers for Hydrographic Studies, NASA SP-375, 137–145.

Murphee, D. L., C. D. Taylor, J. K. Owens, H. R. Ebersole, and R. W. McClendon (1973). Mathematical Modeling and System Recommendations for the Detection of

Fish by an Airborne Remote Sensing Laser. Report No. EIRS-ASE-74-2, Mississippi State University, Engineering and Industrial Research Station, Contract 03-3-042-27 for the National Marine Fisheries Service, Bay St. Louis, MI.

Myers, E. P., and C. G. Gunnerson (1976). Hydrocarbons in the Oceans. NOAA Marine Ecosystems (MESA) Analysis Program Special Report, Boulder, CO.

Nelson, R., W. B. Krabill, and G. Maclean (1984). Determining Forest Canopy Characteristics Using Airborne Laser Data. *Remote Sensing of Environment* **15**, 201–212.

Noble, V. E., R. D. Ketchum, and D. B. Ross (1969). Some Aspects of Remote Sensing as Applied to Oceanography. *Proc. IEEE* **57**, 495–604.

O'Neil, R. A. (1983). Coastal Hydrography Using the CCRS Lidar Bathymeter. Paper presented at Conference on Ocean Environment and Its Interaction with Off Shore Structures, The Swedish Trade Fair Foundation, Goteborg, Sweden, March 1–4, 1983.

O'Neil, R. A., A. R. Davis, H. G. Gross, and J. Kraus (1973). A Remote Sensing Laser Fluorometer, in *The Use of Lasers for Hydrographic Studies*, H. H. Kim and P. T. Ryan, eds., NASA SP-375, Proceedings of a Symposium held at Wallops Island, Virginia, September 12, 1973.

O'Neil, R. A., L. Buja-Bijunas, and D. M. Rayner (1980). Field Performance of a Laser Fluorosensor for the Detection of Oil Spills. *Appl. Optics* **19**, 863–870.

O'Neil, R. A., F. E. Hoge, and M. P. F. Bristow (1981). The Current Status of Airborne Laser Fluorosensing. Proc. of Fifteenth Int. Sym. On Remote Sensing of Environment, Ann Arbor, Michigan, pp. 379–398.

Penny, M. F. (1972). WREMAPS: System Evaluation. WRE-Technical Note-811(AP), Dept. of Supply, Australian Defence Scientific Service, Weapons Research Establishment, Adelaide, Australia.

Penny, M. F. (1972). Laser Hydrography in Australia. Technical Report ERL-0229-TR, Department of Defence, Electronics Research Laboratory, Adelaide, South Australia.

Petri, K. I. (1977). Laser Radar Reflectance of Chesapeake Bay Waters as a Function of Wind Speed. *IEEE Trans. Geosci. Electron.* **GE-15**, 87–97.

Petzold, T. J. (1972). Volume Scattering Functions for Selected Ocean Waters. Final Report Ref. 73-8, Scripps Institution of Oceanography, La Jolla, California.

Phillips, D. M. (1979). Effects of the Wavenumber Spectrum of a Sea Surface on Laser Beam Reflection. *Aust. J. Phys.* **32**, 469–89.

Phillips, D. M., and B. W. Koerber (1984). A Theoretical Study of an Airborne Laser Technique for Determining Sea Water Turbidity. *Australian J. Phys.* **37**, 75–90.

Phillips, D. M., R. H. Abbot, and M. F. Penny (1984). Remote Sensing of Sea Water Turbidity with an Airborne Laser System. *J. Phys. D. Appl. Physics, Great Britain* **17**, 1749–1758.

Poole, L. R., and W. E. Esaias (1982). Water Raman Normalization of Airborne Laser Fluorosensor Measurements: A Computer Study. *Appl. Optics* **21**, 3756–3761.

Poole, L. R., and W. E. Esaias (1983). Influence of Suspended Inorganic Sediment on Airborne Fluorosensor Measurements. *Appl. Optics* **22**, 380–381.

Rayner, D. M., and A. G. Szabo (1978). Time-Resolved Laser Fluorosensors: A Laboratory Study of their Potential in the Remote Characterization of Oil. *Appl. Optics* **17**, 1624–1630.

Rayner, D. M., M. Lee, and A. G. Szabo (1978). Effect of Sea-State on the Performance of Laser Fluorosensors. *Appl. Optics* **17**, 2730–2733.

Remsberg, E. E., and L. L. Gordley (1978). Analysis of Differential Absorption Lidar from the Space Shuttle. *Appl. Optics* **17**, 624–630.

Riley, J. P., and R. Chester (1971). *Introduction to Marine Chemistry*, Academic Press, New York.

Romanova, L. M. (1968). Light Field in the Boundary Layer of a Turbid Medium with Strongly Anisotropic Scattering Illuminated by a Narrow Beam. *Izv., Atmos. Oceanic Phys.* **4**, 1185–1196.

Ross, D. B., R. A. Peloquin, and R. J. Sheil (1968). Observing Ocean Surface Waves with a Helium-Neon Laser. *Proc. 5th Symp. on Military Oceanography*, U.S. Navy Mine Defense Laboratory, Panama City, Florida.

Ross, D. B., V. J. Cardone, and J. W. Conaway, Jr. (1970). Laser and Microwave Observations of Sea-Surface Conditions for Fetch-Limited 17-to-25 m/sec Winds. *IEEE Transactions Geoscience Electronics* **GE-8**, 326–336.

Ryan, D. K., and J. H. Weber (1982). Copper (II) Complexing Capacities of Natural Waters by Fluorescence Quenching. *Environ. Sci. Tech.* **16**, 866–872.

Saar, R. A., and J. H. Weber (1980). Comparison of Spectrofluorometry and Ion-Selective Electrode Potentiometry for Determination of Complexes Between Fulvic and Heavy-Metal Ions. *Anal. Chem.* **52**, 2095–2099.

Sarabun, C. C., Jr. (1981). Mapping Watermass Boundaries Using Fluorosensing Lidar. The Chesapeake Bay Plume Study, Superflux 1980, J. W. Campbell and J. P. Thomas, eds., NASA Conference Proceedings Document CP2188.

Sato, T., Y. Suzuki, H. Kashiwagi, M. Nanjo, and Y. Kasui (1978). Laser Radar for Remote Detection of Oil Spills. *Appl. Optics* **17**, 3798–3803; A Method for Remote Detection of Oil Spills Using Laser-Excited Raman Backscattering and Backscattered Fluorescence. *IEEE J. Oceanic Eng.* **OE-E**(1), 1–4.

Schau, H. C. (1978). Measurement of Capillary Wave Slopes on the Ocean. *Appl. Optics* **17**, 15–17.

Sick, L. V., C. C. Johnson, and A. Engel (1978). Trace Metal Enhancement in the Biotic and Abiotic Components of an Estuarine Tidal Front. *J. Geophys. Res.* **83**, 4659–4667.

Sorenzen, C. J. (1966). A Method for the Continuous Measurement of "In Vivo" Chlorophyll Concentration. *Deep Sea Res.* **13**, 223–227.

Sorenzen, C. J. (1970). The Biological Significance of Surface Chlorophyll Measurements. *Limnology and Oceanography* **15**, 479–480.

Steinvall, O., H. Klevebrant, J. Leander, and A. Widen (1981). Laser Depth Sounding in the Baltic Sea. *Appl. Optics* **20**, 3484–3286.

Stewart, D. E. (1982). A Method for the Extraction and Quantitation of Phycoerythrin

from Algae. NASA Contractor Report 165996 by Bionetics Corporation under Contract NAS1-16978, Hampton, VA.

Stotts, L. B., and S. Karp (1982). Wave Slope Statistics Derived from Optical Radiance Measurements Below the Sea Surface. *Appl. Optics* **21,** 978–981.

Struum, W., and J. Morgan (1981). *Aquatic Chemistry*, Wiley, New York.

Swennen, J. P. J. W. (1968). Time-Average Surface-Reflected Energy Received from a Collimated Beam of Radiant Energy Normally Incident on the Ocean Surface. *J. Opt. Soc. Am.* **58,** 47–51.

Sylvia, A. E., D. A. Bancroft, and J. D. Miller (1974). Detection and Measurements of Microorganics in Drinking Water by Fluorescence. *Am. Water Works Assoc. Tech. Conf. Proc.* Dec. 2–3, 1974, Dallas, TX.

Tang, S. (1981). Field Investigation of the Short Wave Modulation by Long Waves. Dissertation, University of Florida, Gainesville, Florida.

Tang, S., and O. H. Shemdin (1983). Measurement of High Frequency Waves Using a Wave Follower. *J. Geophy. Res* **88,** 9832–9840.

Tooma, S. G., R. D. Ketchum, Jr., R. A. Mennella, and J. P. Hollinger (1976). Comparison of Sea-Ice Type Identification Between Airborne Dual-Frequency Passive Microwaver Radiometry and Standard Laser/Infrared Techniques. *J. Glaciology* **15,** 225–238.

Tsai, B. M., and C. S. Gardner (1982). Remote Sensing of Sea State Using Laser Altimeters. *Appl. Optics* **21,** 3932–3940.

Vertucci, F. A. and A. Vodacek (1985). The Remote Sensing of Lake Acidification Using Laser Fluorosensing. Tech. Papers of the American Society Photogrammetry, 51st Annual Meeting, 10–15 March, Vol. 2, 793–802. Washington, D.C.

Visser, H. (1979). Teledetection of the Thickness of Oil Films on Polluted Water Based on the Oil Fluorescence Properties. *Appl. Optics* **18,** 1746–1749.

Vodacek, A., and W. D. Philpot (1985). Use of Induced Fluorescence Measurements to Assess Aluminum-Organic Interactions in Acidified Lakes. Technical Papers of the American Society of Photogrammetry, Washington, D.C., 51st Annual Meeting, vol. 2, March 11–15, 460–469.

Walsh, E. J., D. W. Hancock III, D. E. Hines, and J. E. Kinney (1984). Electromagnetic Bias of 36 GHz Radar Altimeter Measurements of MSL. *Marine Geodesy* **8,** 265–296.

Watson, R. D. (1981). Airborne Fraunhofer Line Discriminator Surveys in Southern California, Nevada, and Central New Mexico, in *Workshop on Applications of Luminescence Techniques to Earth Resource Studies*, W. R. Hemphill and M. Settle, eds., LPI Technical Report 81-03, Lunar and Planetary Institute, Houston, pp. 19–35.

Yentsch, C. S. (1973). The Fluorescence of Chlorophyll and Yellow Substances in Natural Water: A Note on the Problems of Measurements and the Importance of Their Remote Sensing, in *The Use of Lasers for Hydrographic Studies*, H. H. Kim and P. T. Ryan, eds., NASA SP-375, Proceedings of a Symposium held at Wallops Island, Virginia, September 12, 1973.

Yentsch, C. S. and D. W. Menzel (1963). A Method for the Determination of Phytoplankton Chlorophyll and Phaeophytin by Fluorescence. *Deep Sea Research* **10,** 221–231.

Yentsch, C. M., and C. S. Yentsch (1984). Emergence of Optical Instrumentation for Measuring Biological Properties. *Oceanogr. Mar. Biol. Ann. Rev.* **22,** 55–98.

Yura, H. T. (1973). Propagation of Finite Cross-Section Laser Beams in Sea Water. *Appl. Optics* **12,** 108–115.

Zimmerman, A., and A. R. Bandy (1975). The Application of Laser Raman Scattering to Remote Sensing of Salinity and Turbidity. Final Technical Report, Old Dominion University Research Foundation for NASA Langley Research Center under Master Contact Agreement NAS1-11707, Task Authorization No. 33.

Zimmerman, A. V., F. W. Paul, and R. J. Exton (1976). Research and Investigation of the Radiation Induced by a Laser Beam Incident on Sea Water. Contractor Final Report CR-14519, NASA Grant NSG-1096, Chesapeake College, Wye Mills, MD.